

COMPLEX PHOTONIC CRYSTALS FOR BROADBAND “ALL-ANGLE” SELF-COLLIMATION

by

Yi-Chen Chuang

A dissertation submitted to the faculty of
The University of North Carolina at Charlotte
in partial fulfillment of the requirements
for the degree of Doctor of Philosophy in
Optical Science and Engineering

Charlotte

2010

Approved by:

Dr. Thomas J. Suleski

Dr. Michael A. Fiddy

Dr. Greg J. Gbur

Dr. Eric G. Johnson

Dr. Kevin M. Lawton

© 2010
Yi-Chen Chuang
ALL RIGHTS RESERVED

ABSTRACT

YI-CHEN CHUANG. Complex photonic crystals for broadband “all-angle” self-collimation. (Under the direction of DR. THOMAS J. SULESKI)

Self-collimation is a dispersion property of many photonic crystals (PCs), in which light beam can propagate free of divergence in the PCs. While self-collimation is a desired property for applications related to wave guiding and light collection, most of the current self-collimating PCs have restrictions on incident angles and/or operating wavelengths. These restrictions limit the operation flexibility of current self-collimating devices, and prevent the usefulness of self-collimation in many potential applications. In this dissertation, different PC structures are proposed to enable broadband, (in-plane) “all-angle” self-collimation or three-dimensional (3D) “omnidirectional” self-collimation.

For in-plane self-collimation, a group of non-conventional two-dimensional (2D) PC structures inspired by the irradiance distributions resulting from the fractional Talbot effect (“Talbot crystals”) is studied for the first time. A complex rhombus lattice Talbot crystal is found to support broadband virtual “all-angle” self-collimation. Such concepts are further extended to 3D. Multiple PC structures and different design strategies are proposed and compared in terms of the resulting self-collimation performance. Several desired 3D properties are realized for the first time, including broadband virtual 3D limited-angled self-collimation, 3D omnidirectional beam confinement, and broadband 3D omnidirectional self-collimation. These results may enable future self-collimation applications, such as PC core fibers and solar light collection, and suggest a possible whole-band self-collimation phenomenon.

ACKNOWLEDGMENTS

I would like to thank my advisor, Dr. Thomas Suleski, for his encouragement and support. He introduced me the true spirit of research (i.e. “re-search”) through an Albert Einstein quote “If we knew what we were doing, it wouldn’t be called research...” All the fun discussions with my academic siblings, Dr. Brent Bergner and Aaron Cannistra, have become one of my unforgettable memories in the past years. Thanks guys, especially for your valuable feedback!

I would also like to thank the following people: Dr. Michael Fiddy, for his expertise and inspiring suggestions; Dr. Xianyu Ao, Dr. Raymond “Tipper” Rumpf, and Dr. Kirankumar Hiremath, for their advice on numerical simulations; Dr. Tsing-Hua Her, for his encouragement and many thoughtful Chinese-speaking parties; Dr. Greg Gbur, Dr. Eric Johnson, and Dr. Kevin Lawton, for serving on my committee. To my friends from all over the world, I treasure and appreciate your friendship, especially from Dr. Mingzhen Tang, Dr. Kristin Walker, and Dr. Choon How Gan. To my dear brother Chih-Yang, thank you for cheering me up. Finally, I want to express my deepest appreciation to my dearest mother, Ya-Yuan Chen, for her non-conditional love and understanding. Without her, my dream would not have possibly come true.

TABLE OF CONTENTS

LIST OF TABLES	viii
LIST OF FIGURES	ix
CHAPTER 1: INTRODUCTION	1
1.1 Motivation	1
1.2 Objectives	3
CHAPTER 2: BACKGROUND OF SELF-COLLIMATION STUDIES	5
2.1 Photonic crystals	5
2.2 Isofrequency diagrams	7
2.3 Conditions for self-collimation	9
2.4 Quantifying self-collimation performance	10
2.5 Previous self-collimation studies	13
2.5.1 3D autocloned stacking structure	13
2.5.2 2D PC structures	14
2.5.3 2D complex PC structures	16
2.5.4 3D PC structures	17
2.6 Key features for broadband “all-angle” self-collimation	20
CHAPTER 3: NUMERICAL METHODS & MATHEMATICAL BACKGROUND	21
3.1 Plane wave expansion method	21
3.2 Finite-difference time-domain method	24
3.3 Rigorous coupled-wave analysis	27
3.4 Mathematical background of the fractional Talbot effect	30

CHAPTER 4: INTRODUCTION TO TALBOT CRYSTALS	33
4.1 The fractional Talbot effect	33
4.2 Talbot crystal geometries	35
4.3 Realization of the fractional Talbot effect	36
4.4 Manipulating the irradiance distributions	37
4.5 Realization of Talbot crystals	39
4.5.1 Talbot crystals directly converted from the irradiance distributions	40
4.5.2 Talbot crystals created based on the main features of the irradiance distributions	41
CHAPTER 5: SELF-COLLIMATION IN COMPLEX RHOMBUS LATTICE TALBOT CRYSTALS	44
5.1 Numerical method and notation for isofrequency diagrams	44
5.2 Description of the structure	45
5.3 Comparison of structures made of different materials	46
5.4 Broadband virtual “all-angle” self-collimation	50
5.4.1 Robustness of virtual “all-angle” self-collimation to fabrication tolerance	55
5.4.2 Study of transmission efficiency	57
5.4.3 Diffractive reflection	61
CHAPTER 6: PHOTONIC CRYSTALS FOR THREE-DIMENSIONAL SELF-COLLIMATION	66
6.1 3D tetragonal lattice structures	67
6.2 Out-of-plane self-collimation in 2D triangular lattice structures	70
6.3 3D complex hexagonal lattice structures	75
6.4 Out-of-plane self-collimation in 2D kagome lattice PCs	79
6.5 Summary and discussion	86

	vii
CHAPTER 7: CONCLUSIONS	89
REFERENCES	95
APPENDIX A: PWEM SOURCE CODE	105
APPENDIX B: CODE TO GENERATE IRRADIANCE DISTRIBUTIONS	112
APPENDIX C: DERIVATION OF THE TALBOT DISTANCE	113
APPENDIX D: CODE TO GENERATE DIELECTRIC FUNCTIONS	115

LIST OF TABLES

TABLE 2.1: Summary of current self-collimating PCs and their performance	19
TABLE 3.1: List of numerical methods used and their purposes	30
TABLE 4.1: Procedures to generate and simulate the optical properties of Talbot crystals	43
TABLE 5.1: Results of diffractive reflection analysis	63
TABLE 6.1: Normalized and relative frequency range of omnidirectional self-collimation ($ \theta_p _{max}=0.5^\circ$) for $ k_z \leq 5$ in the triangular lattice structures	73
TABLE 6.2: Normalized and relative frequency range of omnidirectional self-collimation for $ k_z \leq 5$ in the triangular lattice structures ($r=0.48a$) using different background materials	75
TABLE 6.3: Normalized and relative frequency range of omnidirectional self-collimation in the 3D complex hexagonal lattice structures (air cylinders embedded in Si ($\epsilon=12$)/ SiO ₂ ($\epsilon=2.1316$) stack; $z=0.1a$; $h=0.1z$, $r=0.48a$)	78
TABLE 6.4: Normalized and relative frequency range of omnidirectional self-collimation for $ k_z \leq 5$ in the kagome lattice structures (InSb ($\epsilon=17.7$) rods ($r=0.2a$) embedded in an air background)	81
TABLE 6.5: Normalized and relative frequency range of omnidirectional self-collimation for $ k_z \leq 5$ in the embedded kagome lattice structures (β -FeSi ₂ ($\epsilon=31.36$) rods ($r=0.2a$) embedded in SiO ₂ ($\epsilon=2.1316$) background)	85
TABLE 6.6: Summary of PCs for 3D self-collimation and their performance	88
TABLE 7.1: Summary of achieved self-collimation performance in this work with previously reported results if applicable	93

LIST OF FIGURES

FIGURE 2.1: Examples of 1D, 2D, and 3D PCs	6
FIGURE 2.2: Example of band diagram and isofrequency diagram	8
FIGURE 2.3: Schematic example of EFC in PC (right, red) and corresponding air contour (left, black)	9
FIGURE 2.4: Schematic examples of EFCs (color lines) and corresponding air contours (circles) of (a) limited angle self-collimation; (b) “all-angle” self-collimation; (c) “all-angle” self-collimation by open flat EFC; (d) “all-angle” self-collimation by open flat EFC for multiple operating wavelengths. The arrows indicate light propagating directions. Shade areas imply the valid angular collimating range of each case mentioned; (e) schematic diagram showing the maximum absolute refraction angle ($/\theta_{p/max}$).	11
FIGURE 2.5: Schematic diagram showing the orientation of (a) in-plane, and (b) “3D”, self-collimation	13
FIGURE 2.6: (a) 3D autocloned PC structure showing self-collimation and superprism effect [77] (b) experimental self-collimated beam in the 3D autocloned PC structure (top-plane image) [67]	14
FIGURE 2.7: Example EFCs of (a) a square lattice structure; and (b) a triangular lattice structure	16
FIGURE 2.8: (a) 2D complex PC showing (b) broadband flat EFCs [2]	17
FIGURE 3.1: Yee’s mesh [97]	26
FIGURE 3.2: Geometry for diffraction of a plane wave by a 1D optical grating	32
FIGURE 4.1: 2D irradiance profile from 1D binary amplitude grating (simulation result)	35
FIGURE 4.2: Schematic diagram of the setup to generate periodic/quasi-periodic irradiance distribution based on the fractional Talbot effect	37
FIGURE 4.3: Examples of irradiance distributions resulting from the fractional Talbot effect	38
FIGURE 4.4: Examples of the Talbot crystals directly converted from the irradiance distributions by assuming a simple threshold as the contour reference	41

FIGURE 4.5: Examples of the Talbot crystals directly converted from an irradiance distribution by assuming different irradiance thresholds as the contour reference	41
FIGURE 4.6: Example of Talbot crystal created by mimicking the main features of the irradiance distribution resulting from the fractional Talbot effect	42
FIGURE 5.1: Complex rhombus lattice structure with elliptical rods embedded in air background	46
FIGURE 5.2: (a) Fifth band EFCs for TM polarization of the Talbot crystal shown in FIGURE 5.1(a). Hexagonal area (dotted line) is the first BZ and special k -points are indicated in the figure. (b) Fifth band EFCs at frequency of $1.4 \mu\text{m}^{-1}$ ($\lambda=714 \text{ nm}$)	48
FIGURE 5.3: (a) Fifth band EFCs for TM polarization using Si as the dielectric material. Hexagonal area (dot lines) indicates the first BZ with some special k -points defined as in the figure. (b) Fifth band EFCs at frequency $0.66 \mu\text{m}^{-1}$ ($\lambda=1515 \text{ nm}$)	50
FIGURE 5.4: Relative operating range of the “nearly flat” ($\theta_p/\theta_{p,max}=2^\circ$) EFCs in the fifth band for TM polarization within the domain of study	52
FIGURE 5.5: Fifth band EFCs of the described complex rhombus structure for TM polarization	55
FIGURE 5.6: Wavelength range ($\Delta\lambda$; bars; left axis) and relative range ($\Delta\lambda/\lambda_c$; dots; right axis) of “nearly flat” EFCs based on the best design by rescaling the elliptical rods proportionally	57
FIGURE 5.7: (a) PC structure for transmission study (b) Modified PC with additional anti-reflection rods	58
FIGURE 5.8: (a) Transmission spectrum of the power within the illuminated width at the exit side of the PC. (b) Corresponding transmission spectrum of the PC with anti-reflection rods	59
FIGURE 5.9: Beam combining effect using 1495 nm and 1607 nm wavelengths at -30° and 30° respectively	60
FIGURE 5.10: Normalized reflection spectrum of the total power for PCs with different lattice aspect ratios at 30° incident angle	65
FIGURE 6.1: (a) Hole-type tetragonal lattice structure under study. (b) 3rd band EFS at $aa/2\pi c=0.3$ of the tetragonal lattice structure with $a=1.05$. (c)~(f) Cross-sections of the 3rd band EFSs at $k_y=0, 0.05, 0.1$, and	68

0.15, respectively

- FIGURE 6.2: (a) Orientation for out-of-plane propagation in 2D triangular lattice structures. (b) Top view of the structure 71
- FIGURE 6.3: Cross-sections of the EFSs at $k_y=0$ for (a) 1st (b) 2nd (c) 3rd (d) 4th (e) 5th band of the triangular lattice structure (air cylinders in Si background, $r=0.48a$) 72
- FIGURE 6.4: (a) 1st band EFSs of the triangular lattice structure ($r=0.48a$) at $\omega a/2\pi c=1.2$ (b) Band diagram for in-plane propagation 72
- FIGURE 6.5: (a) 3D complex hexagonal lattice structure combining a 2D triangular lattice array with an alternative dielectric stack (b) top view and (c) side view of the structure 76
- FIGURE 6.6: Cross-sections at $k_y=0$ for (a) 1st (b) 2nd (c) 3rd (d) 4th (e) 5th band EFSs of the 3D complex hexagonal lattice structure (air cylinders embedded in Si ($\epsilon=12$)/ SiO₂ ($\epsilon=2.1316$) stack; $z=0.1a$; $h=0.1z$, $r=0.48a$) 77
- FIGURE 6.7: (a) The 2D rod-type kagome lattice PC structure [123] under study. (b) The band diagram of this kagome structure [123] (c) The orientation for 3D self-collimation. (d) The “embedded design” 80
- FIGURE 6.8: Cross-sections at $k_y=0$ for (a) 1st (b) 2nd (c) 3rd (d) 4th (e) 5th band EFSs of the kagome lattice structure (InSb ($\epsilon=17.7$) rods ($r=0.2a$) embedded in an air background) 81
- FIGURE 6.9: (a) Cross-section of the 4th band EFSs at $k_y=0$ (b) close view for $\omega a/2\pi c=0.22\sim 0.4$ 83
- FIGURE 6.10: 4th band EFSs of the kagome lattice structure at (a) $\omega a/2\pi c=0.38$ (b) $\omega a/2\pi c=0.25$ 83
- FIGURE 6.11: Cross-sections of the EFSs at $k_y=0$ for (a) 1st (b) 2nd (c) 3rd (d) 4th (e) 5th band of the embedded kagome lattice structures (β -FeSi₂ ($\epsilon=31.36$) rods ($r=0.2a$) embedded in SiO₂ ($\epsilon=2.1316$) background) 85
- FIGURE 6.12: (a) Cross-section of the 4th band EFSs at $k_y=0$ of the embedded kagome lattice structure (β -FeSi₂ ($\epsilon=31.36$) rods ($r=0.2a$) embedded in SiO₂ ($\epsilon=2.1316$) background) (b) close view for $\omega a/2\pi c=0.18\sim 0.26$ 86

CHAPTER 1: INTRODUCTION

1.1 Motivation

Self-collimation (also referred to as self-guiding [1] or super-collimation [2]) is a dispersion property of many photonic crystals (PCs), which describes an optical phenomenon where light propagating in a medium is free of diffraction and divergence along the collimating direction. It can be used for different purposes, such as, confining light from spreading, eliminating power loss during propagation, and combining or collecting multiple incident beams toward the same direction. Self-collimation allows a narrow beam to propagate in the PC without engineered defects (such as waveguides), and thus it may simplify fabrication processes for some PC devices. In addition, PCs are incident position invariant (i.e. beams can be self-collimated by the structure regardless of the positions at which the beams are incident); therefore beam alignment in self-collimating PCs is relatively straightforward.

Self-collimation is a very useful phenomenon that can benefit a variety of applications related to wave guiding and/or light collection. Current self-collimation applications include waveguides [3, 4], beam splitters [5-12], optical switches [13], interferometers [14-16], wave plates [17], resonators [18, 19], lasing cavities [20], and beam combiners [21]. Most of the current applications apply self-collimation to a single propagation beam and do not require a wide angular collimating range and/or broad wavelength/frequency range for operation. While there have been few studies applying

self-collimation to multiple beams, self-collimation can also be very useful for beam combining and light collecting purposes. Potential applications include multiplexers [22, 23]¹, solar light collection [24-30]², and PC core fibers [31-33]³. These applications utilize the property that light incident from different incident angles within a valid angular collimating range will be collimated to the same direction. Besides non-channel waveguiding and easy alignment that is generally offered by the self-collimation phenomenon, self-collimation in these applications can also provide additional benefits. For example, a self-collimating beam combiner or multiplexer requires no input or output waveguides, thus simplifying the device design. A self-collimating PC on the top of a solar cell could help to gather and guide light from large incident angles to reach the solar cell at smaller incident angles, potentially reducing the need for the solar panel to track the sun throughout the day as the incident angles change. A PC core fiber using self-collimating PC as the fiber core can allow a larger acceptance cone for light coupling. These potential applications have not yet benefited from self-collimation phenomenon because current PCs do not support the desired self-collimation performance (i.e. a wide angular collimating range and a broad operating wavelength/frequency range) in suitable orientation for the purposes mentioned.

¹⁻³: These references provide general information about the applications mentioned, but do not apply self-collimation ideas.

1.2 Objectives

Although a collimating structure that can be used for all incident angles across a broad wavelength range is highly desirable, very few related studies have been published with this purpose [2, 34]. Also, previously reported broadband “all-angle” self-collimation is limited to in-plane propagation. PC structures supporting broadband self-collimation in a three-dimensional (3D) manner have not yet been reported (an introduction will be given later in Section 2.4). This dissertation is intended to present and discuss improvements to self-collimation performance through engineering of PC structures. Several PC structures are investigated to achieve ideal broadband (in-plane) “all-angle” or (3D) “omnidirectional” self-collimation. The work in this dissertation can be divided to two parts. The first part explores additional two-dimensional (2D) PC structures to support broadband “all-angle” self-collimation. In particular, a group of non-conventional 2D PC structures inspired by the irradiance distributions resulting from the fractional Talbot effect [35-38] (“Talbot crystals”) is studied for the first time. Talbot crystals are considered because they have more design flexibility over traditional PCs. Comparisons between the self-collimating Talbot crystals and previously reported self-collimating PCs are made in terms of self-collimation performance and other practical performance metrics. The second part of this work further extends the concept of broadband “all-angle” self-collimation to 3D. Several PC structures are proposed to enable 3D broadband omnidirectional self-collimation, including 3D tetragonal lattice structures, 3D complex hexagonal lattice structures, and two 2D PC structures* (*PC structures in 3D space with 2D periodicity). Detailed structure descriptions will be provided in CHAPTER 6. Different design strategies are presented and compared in

terms of the resulting self-collimation performance. 3D self-collimation effects realized by different mechanisms are also discussed.

Background knowledge and basic terminology for self-collimation studies are presented in CHAPTER 2, and theories and numerical methods used in these studies are described in CHAPTER 3. Detailed descriptions of Talbot crystals are given in CHAPTER 4, including comparison between Talbot crystals and conventional PCs. CHAPTER 5 presents simulation results of self-collimation in a complex rhombus lattice Talbot crystal. Structure optimization and the effects of adding an anti-reflection feature to the Talbot crystals are also discussed. CHAPTER6 focuses on PC structures proposed for broadband omnidirectional self-collimation. Different design strategies with the resulting self-collimation performance are presented and compared in detail. Conclusions and future work are provided in CHAPTER 7.

CHAPTER 2: BACKGROUND OF SELF-COLLIMATION STUDIES

In this dissertation, self-collimation performance of different PC structures is quantitatively investigated and compared. For this purpose, background knowledge and related terminologies are provided in this chapter. First, the media that are used to realize self-collimation phenomenon (i.e. PCs) are introduced. Then the essential tools to identify and quantitatively study self-collimation (i.e. isofrequency diagrams) are described. Conditions where self-collimation is realized are summarized, followed by quantitative definitions of self-collimation performance metrics. Performance of previously reported self-collimating PC structures are also reviewed and compared.

2.1 Photonic crystals

PCs are periodic or quasi-periodic dielectric materials designed to control and manipulate light through careful engineering. Simple examples of one-dimensional (1D), 2D, and 3D PCs are displayed in (FIGURE 2.1) Due to their small size and flexibility for integration with other optical components, PCs have become promising candidates to realize desired optical properties in many optical devices, especially for optical integrated circuits [39, 40]. Many interesting optical phenomena that do not exist in nature have been found in PCs, including photonic band gaps (PBGs) [39, 41-44], negative refraction, superprism effects, and self-collimation.

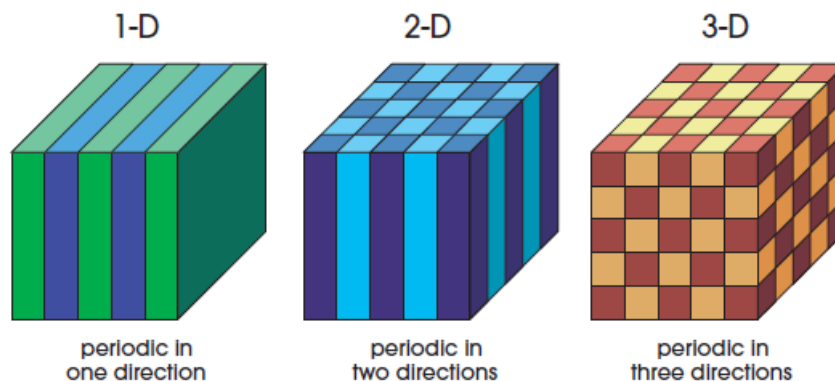


FIGURE 2.1: Examples of 1D, 2D, and 3D PCs. The different colors represent materials with different dielectric constants. The defining feature of a PC is the periodicity of dielectric material along one or more axes. [39]

A PBG prohibits light propagation in a PC within a certain frequency range. One may incorporate defects in such PBG structures to allow desired modes to propagate. There have been different applications utilizing the PBG property, for example, mirrors [45], filters [46, 47], waveguides [48-50], beam splitters, [51], and PC lasers [52, 53]. A PC often requires a large refractive index contrast between the materials used to open a PBG [39, 54, 55]. Therefore, the materials that can be used for this purpose are limited.

In addition to the PBG property, PCs can also possess complicated photonic band structures allowing light to display strong dispersion and anisotropy, including negative refraction [56-62], self-collimation [3, 6, 7, 20, 63-69], and superprism effects [70, 71]. These phenomena are generally referred to as the *dispersion properties* of PCs and have attracted large attention recently. Instead of searching for a PBG, the wave vector (k -vector) and the directionality of the band structure become the main focus of related studies. Since dispersion properties of a PC do not require a PBG, dispersion properties can be realized using materials with low refractive index contrast. Thus materials with relatively low refractive index, such as glass [72], chalcogenide glass [7], polymer [73],

SiN_x [74], and SU-8 [75, 76], can be utilized to provide more design flexibility and functionality.

2.2 Isofrequency diagrams

To study dispersion properties of PCs, an *isofrequency diagram* (or *wavevector diagram*) [39] is an essential guide map to determine beam propagation direction. An isofrequency diagram is a contour plot of the eigen-frequencies of Maxwell's equations (angular frequency, $\omega(k)$) in 2D or 3D wave vector space (k -space). It is similar to the representation of the band diagram, except band diagrams only plot $\omega(k)$ of the k -points along the boundary of the irreducible Brillouin zone (BZ) while isofrequency diagrams include $\omega(k)$ of a k -point mesh covering the whole chosen k -space. The required eigen-frequencies can be calculated using numerical methods, such as the plane wave expansion method (PWEM) as will be introduced in Section 3.1. As an example, the band diagram of a 2D rectangular lattice structure (FIGURE 2.2(a)) is shown in FIGURE 2.2(b) along with its isofrequency diagram in FIGURE 2.2(c).

The contour lines in 2D isofrequency diagram and contour surfaces in 3D isofrequency diagram are usually referred to *equi-frequency contours* (EFCs) (or *isofrequency contours* [39]) and *equi-frequency surfaces* (EFSs) (or *isofrequency surfaces* [39]) respectively. EFCs and EFSs of isotropic materials, such as air, are circles and spherical surfaces respectively. The radius of each EFC/EFS represents the wavenumber ($2\pi n/\lambda$) of the corresponding incident light, where n is the refractive index of the material and λ is the incident wavelength. In this case, light propagation follows Snell's law. On the other hand, EFCs and EFSs of anisotropic materials, such as many PCs, can be different shapes. As a result, by engineering the shape of EFCs/EFSs, one

may manipulate beam propagation in such anisotropic materials to create a variety of interesting non-conventional optical properties (i.e., dispersion properties of PCs as mentioned earlier) to benefit many applications.

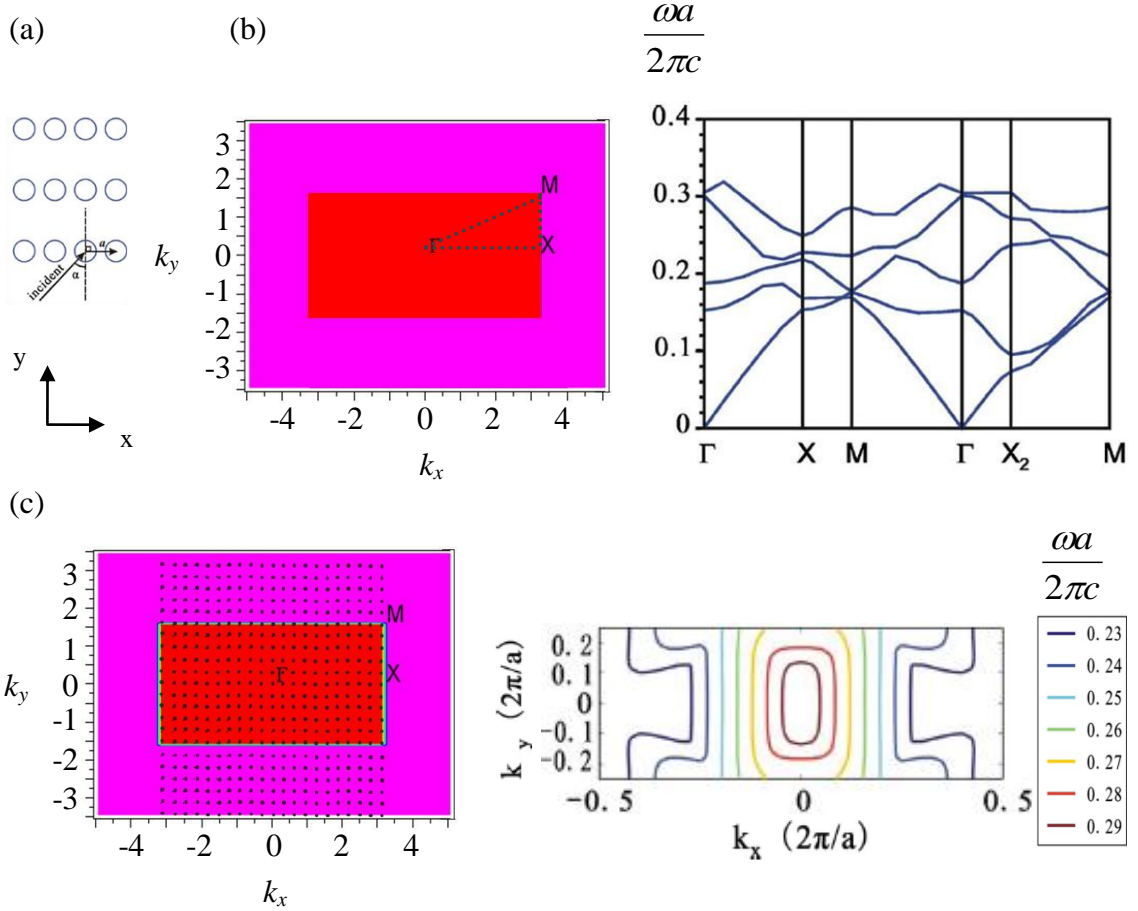


FIGURE 2.2: Example of band diagram and isofrequency diagram. (a) Geometry of the lattice structure (b) (left) selected k -points along the boundary of the irreducible BZ; (right) band diagram of the rectangular lattice structure (c) (left) selected k -point mesh in the k -space; (right) isofrequency diagram of the same structure [3]

Since the direction of propagating light in a medium is the direction of its group velocity, $v_g = \nabla_k \omega(k)$, this direction can be determined based on EFCs (and/or EFSs) of the incident and propagating media and the incident k -vector [39, 77, 78]. An illustration of this concept is shown in FIGURE 2.3 [39], where schematic examples of EFCs of a PC

and the incident medium (assumed air) are displayed as indicated. Assume light with incident k -vector (blue arrow, FIGURE 2.3) is incident from air to a PC. The propagating direction of light in the PC (red arrow ②) is the gradient direction of its corresponding EFCs at the intersection with the tangential k -vector conservation line (blue dot line) away from the air-PC interface. Based on this principle, one may determine the propagating direction in a PC (red arrows ①~⑤) using EFCs as long as the incident wavelength and incident angle (corresponding black arrows ①~⑤) are given.

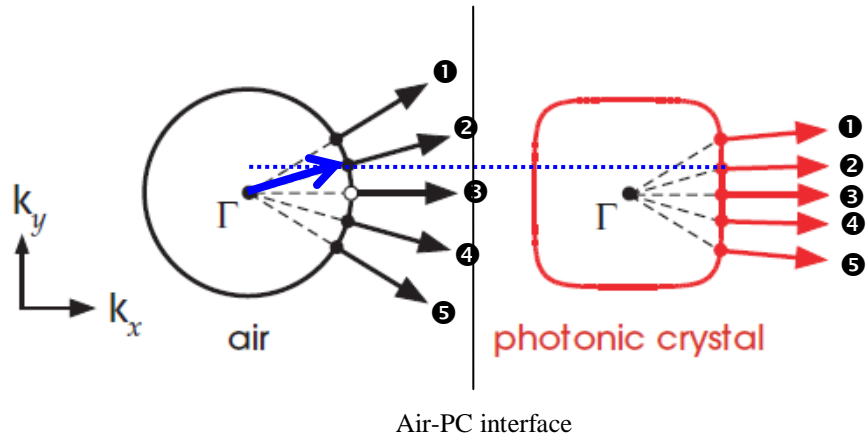


FIGURE 2.3: Schematic example of EFC in PC (right, red) and corresponding air contour (left, black). Arrows show the group velocity directions for a variety of k vectors (dots) with different k_y components. The horizontal dot line (blue) indicates surface parallel k -vector conservation. The flat contour of the PC implies self-collimation phenomenon. [39]

2.3 Conditions for self-collimation

Self-collimation only occurs under certain conditions. First, the PC structure must show partially or totally flat EFCs; also, at least one of these flat EFCs must intersect with their corresponding k -vector conservation lines (the lines indicate surface-parallel k -vector conservation) at the same frequency (FIGURE 2.3 [39]). Similar principles apply to 3D cases, where flat EFS intersecting with the corresponding k -vector conservation

line is essential. These requirements can limit the self-collimation phenomenon, including incident angles and/or working wavelengths, as will be discussed in the next section.

2.4 Quantifying self-collimation performance

One may describe the performance of self-collimation in terms of three parameters: angular collimating range, operating range (in terms of wavelength and/or frequency), and degree of self-collimation.

The angular collimating range is the range of valid incident angles (θ_i) showing self-collimation. It is described by $|\theta_i| \leq \theta$ in this dissertation, where θ is the half-angle of the angular collimating range as shown in FIGURE 2.4(a). In this example, the projection of the partially flat EFC parallel to the air-PC interface is shorter than the diameter of the corresponding air contour; only light rays incident within the shaded area have their k -vector conservation lines intersect with the flat EFC. Therefore, the shaded area indicates the valid angular collimating range of this case. Only light incident within this valid angular collimating range can be collimated. Light incident from other angles does not have its k -vector conservation lines intersect with the flat EFC, thus this light will be refracted to other directions or may not even be coupled to this PC. On the other hand, in the partially flat EFC shown in FIGURE 2.4(b), the projection of the flat EFC parallel to the air-PC interface is longer than the diameter of the corresponding air contour, and thus “all-angle” self-collimation occurs. “All-angle” self-collimation in 2D representation refers to a phenomenon that all incident light in the plane of incidence from -90 degrees to 90 degrees ($|\theta_i| < 90^\circ$) can be collimated [6]. In a special case of open flat EFCs, “all-angle” self-collimation is shown regardless of the size of the corresponding air contour (FIGURE 2.4(c)). Therefore, open flat EFCs are not essential to show “all-angle” self-

collimation but remain a preferable characteristic for this purpose. Such open flat EFCs can be seen in a rectangular lattice structure proposed by Xu [6] at a specific operating frequency.

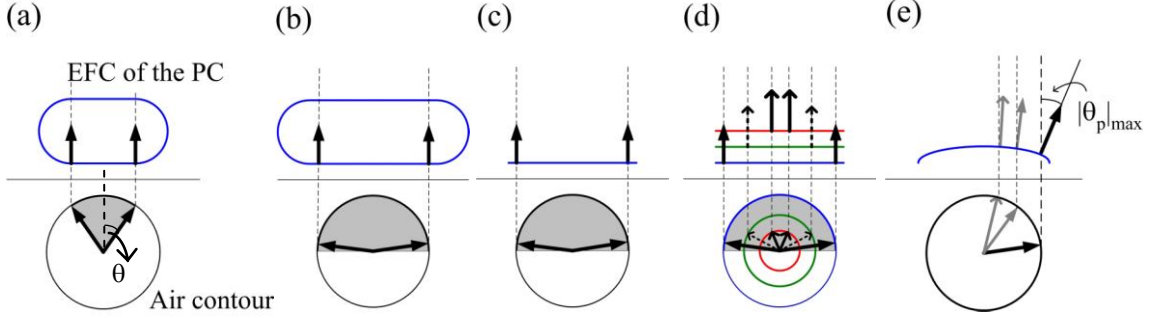


FIGURE 2.4: Schematic examples of EFCs (color lines) and corresponding air contours (circles) of (a) limited angle self-collimation; (b) “all-angle” self-collimation; (c) “all-angle” self-collimation by open flat EFC; (d) “all-angle” self-collimation by open flat EFC for multiple operating wavelengths. The arrows indicate light propagating directions. Shade areas imply the valid angular collimating range of each case mentioned; (e) schematic diagram showing the maximum absolute refraction angle ($|\theta_p|_{max}$). In this example, the primary collimating direction is the air-PC interface normal.

Operating range ($\Delta\lambda$) is the range of wavelengths supporting self-collimation. It is also represented by its relative form, $\Delta\lambda/\lambda_c$ or its equivalent form $\Delta f/f_c$, where λ_c , f , and f_c are the central wavelength, frequency, and central frequency, respectively. The definition of this relative operating range is very similar to the expression of the gap-midgap ratio used to describe the size of a photonic band gap [39]. Since relative operating range is invariant no matter the wavelength of interest, it is a more objective measure of the operating range. If a PC structure has multiple open flat EFCs across a broad operating wavelength (or frequency) range (FIGURE 2.4(d)), this structure could be a good candidate to realize *broadband* “all-angle” self-collimation.

In some cases, EFCs are not perfectly flat, thus only a degree of self-collimation

is achievable. We introduce the maximum absolute refraction angle ($|\theta_p|_{max}$) as a means to quantify the degree of self-collimation. The angle $|\theta_p|_{max}$ is the largest deviation of the propagation direction from the primary collimating direction (FIGURE 2.4(e)); in the ideal self-collimation cases mentioned earlier, $|\theta_p|_{max} = 0^\circ$. As a result, the smaller the value of $|\theta_p|_{max}$, the flatter the EFC, and the better the degree of self-collimation. In this case, light beams in the PC would be refracted slightly off the primary propagating direction within an angle of $|\theta_p|_{max}$. If multiple frequencies are considered, $|\theta_p|_{max}$ refers to the overall maximum value of $|\theta_p|_{max}$ among all chosen frequencies. Such a virtual collimated beam will also slightly diverge as it propagates. However, in case where ideal self-collimation performance is not achievable for broadband “all-angle” operation, some slight compromises on the degree of self-collimation might be acceptable in order to improve both angular collimating range and operating wavelength range.

The EFC examples given in FIGURE 2.4 illustrate the performance of “in-plane” self-collimation in 2D PC structures, where the out-of-plane k -vector is assumed zero ($k_z=0$, FIGURE 2.5(a)) But the same principles can be extended to 3D cases, where the out-of-plane k -vector is not necessary zero and the valid angular self-collimation range is described by an angular collimating “cone” (FIGURE 2.5(b)). In 3D cases, the area and the flatness of the EFSs decide the performance of self-collimation. Assume the radius of the inscribed circle of the flat EFS is r_k , then the acceptance angle (Θ) of the angular collimating “cone” can be determined by $\Theta = \sin^{-1}(r_k/r_a)$, where r_a is the radius of the corresponding air contour surface at the same frequency. If $\Theta=90^\circ$, it refers to ideal omnidirectional self-collimation. The term “omnidirectional”, as used in omnidirectional mirrors [39], includes all incident angles in the semi-spherical space of the incident

medium. In this dissertation, the air-PC interface is assumed extended to infinity so that light incident on the “sides” of a PC is excluded in our discussion. To date, omnidirectional self-collimation has not yet been reported in any PC structure.

From an application point of view, a collimating device that can be used for all incident angles across a broad operating range is greatly desirable. Therefore, a wider angular collimating range and a broader operating range imply broader applicability for self-collimation effects.

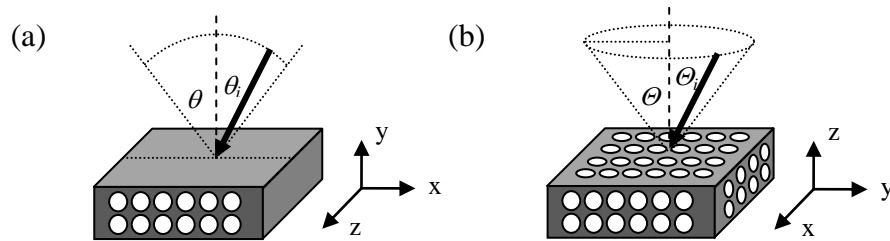


FIGURE 2.5: Schematic diagram showing the orientation of (a) in-plane, and (b) “3D”, self-collimation. The dot fan and dot cone indicate the range of incident angles supporting self-collimation, where θ_i and Θ_i represent incident angles in the angular collimating ranges of the two cases respectively. θ and Θ imply the half-angle and the acceptance angle supporting self-collimation of the two cases respectively. If $\Theta=90^\circ$, omnidirectional self-collimation occurs.

2.5 Previous self-collimation studies

Many different lattice structures exhibiting self-collimation have been considered by other researchers. It is shown that the performance of self-collimation is strongly dependent on the geometry of the PC structures. In the following subsections, these lattice structures are reviewed, and their self-collimation performances are discussed.

2.5.1 3D autocloned stacking structure

The first PC found showing self-collimation is a 3D autocloned stacking structure. This structure was fabricated by depositing alternating layers of Si and SiO₂ on a Si

substrate with a SiO_2 buffer that had a hexagonal array of holes, resulting in self-organized (autocloned) Si/SiO_2 stacking layers [67, 79] (FIGURE 2.6(a) [77]) Each layer of this structure can be considered a 2D triangular/hexagonal PC slab. In this reference, experimental results of a self-collimated beam are presented (FIGURE 2.6(b) [67], top-plane image) when a TM polarized (magnetic field parallel to the plane, as defined in [39]) laser beam (956 nm) is incident from the side of the structure at 15° ($|\theta_i| = 15^\circ$). In this structure, the self-collimated beam is confined to propagate in plane by the alternating layers; and the self-collimation phenomenon is mainly caused by the anisotropy of the triangular lattice feature. However, self-collimation in this stacking structure only occurs at a specific incident angle for a particular wavelength.

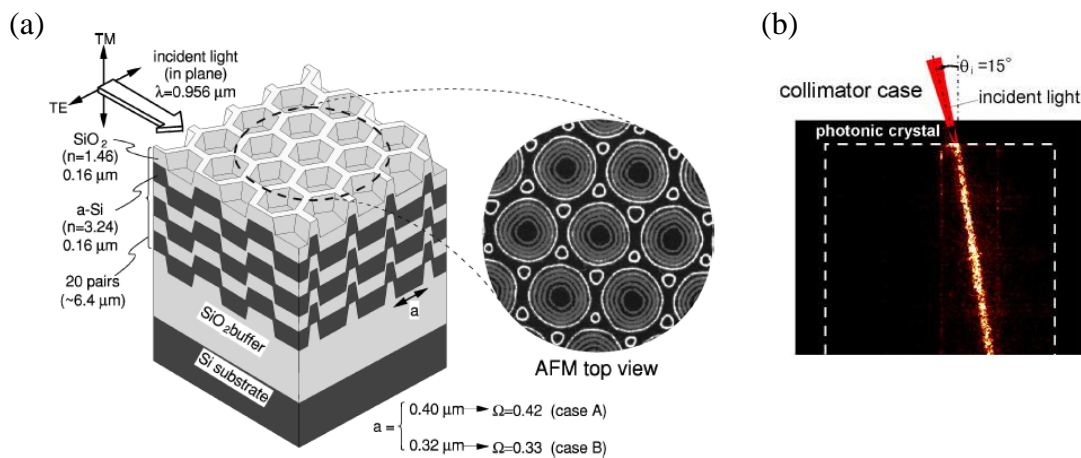


FIGURE 2.6: (a) 3D autocloned PC structure showing self-collimation and superprism effect [77] (b) experimental self-collimated beam in the 3D autocloned PC structure (top-plane image) [67]

2.5.2 2D PC structures

Since the discovery of self-collimation phenomenon, many different 2D PC structures have been proposed and studied. Generally, PCs with lower geometric symmetry tend to support a wider angular collimating range [6] and/or broader operating

range of self-collimation. For some frequencies, the form of EFCs mimics the form of the BZ of the crystal. In such case, a longer side of the BZ corresponds to a longer flat EFC. For example, a four-fold symmetry square lattice has a better chance to have longer flat EFCs compared with a six-fold triangular one, which results in a larger angular collimating range (FIGURE 2.7) [1]. Therefore, square lattice structures have been extensively studied for self-collimation applications [5, 7-9, 13-17, 19-21, 63]. In addition to conventional circular scatterers, different scatterer shapes in a square lattice structure have also been investigated to improve self-collimation performance and enable polarization-independent self-collimation (*absolute self-collimation*) [5, 80]. Very recently, 2D square lattice structures using elliptical scatterers were reported that show broadband “all-angle” self-collimation [34].

Based on the same principle of breaking the geometric symmetry, 2D rectangular and parallelogram lattice structures were proposed [3, 6, 68]. These two structures successfully realized “all-angle” self-collimation with a relatively narrow operating range [3, 6] and/or relatively broadband self-collimation within limited incident angles [3]. In such cases, a shorter side of the BZ implies a better chance to obtain open EFCs [6] which is a desired condition for “all-angle” self-collimation as mentioned in Section 2.4. An illustration of this concept can be referred to the example shown in FIGURE 2.2. Such properties are particularly desirable for self-collimating beam combiners and multiplexers. Unfortunately, the operating wavelength ranges of the “all-angle” self-collimation in these 2D rectangular and parallelogram lattice structures are narrow compared to previously mentioned square lattice structure proposed by Liang [34] and a hybrid square lattice structure proposed by Hamam [2] (Section 2.5.3).

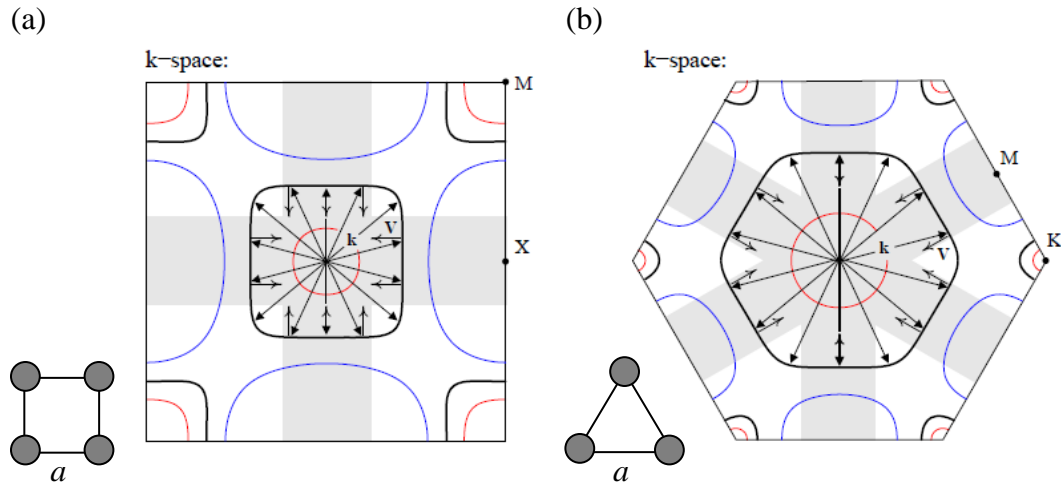


FIGURE 2.7: Example EFCs of (a) a square lattice structure; and (b) a triangular lattice structure. Both of the structures are made of dielectric rods ($n=2.9$; $r=0.15a$, where n , r , and a are refractive index, radius of the rods, and lattice constant, respectively) in air [1]

2.5.3 2D complex PC structures

2D complex PC structures (hybrid lattice structures [2], or superlattice structures [81]) refer to PC structures which include multiple sub-lattices and/or different shaped scatterers in a unit cell. Recently, Hamam et al. designed a 2D hybrid square lattice structure to realize broadband “all-angle” self-collimation [2]. In this structure, a 1D waveguide array is superposed with a 2D rod-type square lattice sub-lattice (FIGURE 2.8). The 1D waveguide array provides the broadband feature while the square sub-lattice shows self-collimation phenomenon [2]. This structure supports 2D “all-angle” self-collimation over a 13 % operating range for TM polarization. This result suggests the possibility of achieving self-collimation of polychromatic beams.

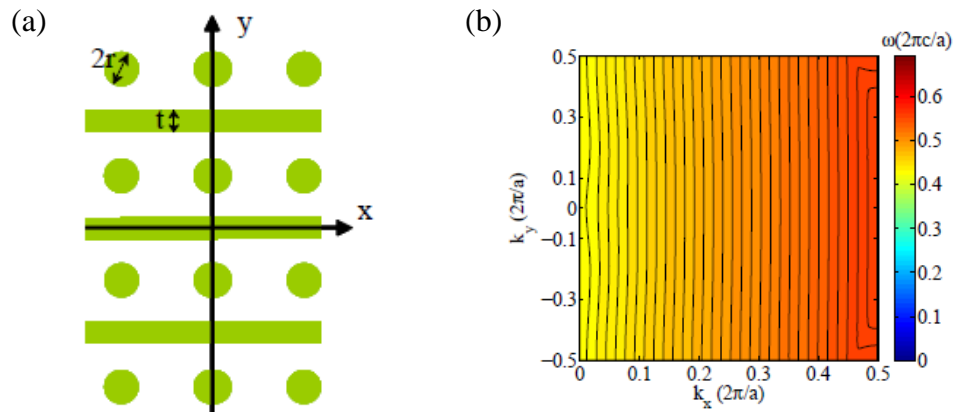


FIGURE 2.8: (a) 2D complex PC showing (b) broadband flat EFCs [2]

Although 2D PC structures are capable of realizing broadband “all-angle” self-collimation, such properties are limited to in-plane propagation ($k_z=0$). In other words, light beams in such 2D PCs can only be collimated in the plane with periodicity (x-y plane, FIGURE 2.5); a light beam with any non-zero out-of-plane k -vector ($k_z \neq 0$) is still likely divergent in the third direction (z -direction). One may confine out-of-plane propagation using index guiding in 2D PC slabs, but the propagating beams are not “truly” 3D self-collimated beams.

2.5.4 3D PC structures

As discussed earlier, 3D self-collimation is highly desirable, but 3D structures require significant computational resources for numerical calculation, and fabrication of 3D structures are challenging. As a consequence, there have been relatively few studies using 3D structures to realize self-collimation. All the reported 3D self-collimating PCs to date are highly symmetric lattice structures, such as simple cubic (sc) lattice structures [66, 82, 83], face centered cubic (fcc) lattice structures (including woodpile structures, inverse opal structures [84], contact-free woodpile-like structures [85]), and body

centered cubic (bcc) [64]. As a result, the angular collimating range and operating range of self-collimation in these structures are both relatively narrow. And 3D self-collimating PCs have only been considered for applications like optical routing [66], optical bends and beam splitters [64]. While a PC showing broadband omnidirectional self-collimation is highly desired, to date no work has been reported in terms of PC design to achieve this goal.

In this section, we have briefly reviewed current self-collimating PCs. The geometrical structure of the PCs discussed and their performance is summarized in TABLE 2.1. Self-collimation performance of our proposed structures will be presented in CHAPTER 5 and CHAPTER 6. Comparisons between current self-collimating PCs and our proposed structures will be discussed in terms of self-collimation performance and some practical concerns.

PC structures	Example self-collimation performance	Reference
3D autocloned stacking structures	Only a single θ_i was reported Only a single λ was reported TM polarization	Kosaka et al. (1999) [67, 79]
2D square lattice structures	$ \theta_i < 19^\circ$ ^(†) Only a single λ was reported TM polarization	Chigrin et al. (2003) [1]
2D square lattice structures with pill-void scatterers	$ \theta_i < 45^\circ$; $\Delta\lambda/\lambda_c = 2.8\%$ ^(†) Absolute self-collimation	Xu et al. (2009) [80]
2D square lattice structures with elliptical scatterers	“All-angle” self-collimation ($ \theta_i < 90^\circ$) $\Delta\lambda/\lambda_c = 10.9\%$ ^(†) for TM polarization (rod-type structure) $\Delta\lambda/\lambda_c = 9\%$ ^(†) for TE polarization (hole-type structure)	Liang et al. (2010) [34]
2D rectangular lattice structures	“All-angle” self-collimation ($ \theta_i < 90^\circ$) $\Delta\lambda/\lambda_c = 4\%$ ^(†) ; TE polarization	Gao et al. (2008) [3]
	$ \theta_i < 10^\circ$ ^(†) ; $\Delta\lambda/\lambda_c = 23\%$ ^(†) ; TE polarization	Gao et al. (2008) [3]
2D complex lattice structures	“All-angle” self-collimation ($ \theta_i < 90^\circ$) $\Delta\lambda/\lambda_c = 13\%$; TM polarization	Hamam et al. (2009) [2]
3D sc	$ \theta_i < 29^\circ$ for $ \theta_p _{max} \sim 6.7^\circ$ ^(†) Only a single λ was reported	Lu et al. (2006) [82]
3D woodpile structures (fcc)	$ \theta_i < 23.6^\circ$ ^(†) for average curvature 0.134 Only a single λ was reported	Iliev et al. (2005) [84]
3D bcc	$ \theta_i < 20^\circ$ for $ \theta_p _{max} \sim 0.52^\circ$ ^(†) Only a single λ was reported	Shin et al. (2005) [64]

TABLE 2.1: Summary of current self-collimating PCs and their performance.

†Determined (calculated by us) based on the published data

2.6 Key features for broadband “all-angle” self-collimation

To summarize, there are three keys to obtain broadband “all-angle” self-collimation in 2D PCs. First, the structure must have periodicity along the desired collimating direction [2]; it provides the chance for the curvature of the EFC to flip sign, resulting in the flat EFCs (EFSs for 3D cases) required for self-collimation. This is the conventional criteria for the self-collimation phenomenon. Second, the structure is preferred to include (to some extent) an isolated waveguiding configuration along the desired collimating direction; such features provide broadband properties in higher-order bands, similar to the concept of tight-binding bands in solid state physics [2]. The waveguiding configuration can be, for example, the 1D waveguide in Hamam’s hybrid square lattice structure [2], and the aligned elliptical scatterers in Liang’s square lattice structure [34], the aligned pill-void scatterers in Xu’s square lattice structure [80], and the aligned circular scatterers in Gao’s rectangular lattice structure [3]. Third, structures with lower geometrical symmetry tend to show a wider angular collimating range. This result can be understood in terms of the size of the 1st BZ. Structures with lower geometrical symmetry usually have 1st BZs that have less symmetrical shapes. A longer side of the 1st BZ corresponds to a longer flat EFC for cases where the form of the EFCs mimics the form of the BZ of the crystal [1]. In many other cases, a shorter side of the 1st BZ perpendicular to the desired collimating direction can help to obtain open flat EFCs, thus resulting in a wider angular collimating range [6]. Such concepts can be found in 2D PCs supporting “all-angle” self-collimation, including rectangular, parallelogram, and rhombus lattice structures [3, 6, 86]. These design rules will be extended to 3D to realize broadband omnidirectional self-collimation in CHAPTER 6.

CHAPTER 3: NUMERICAL METHODS & MATHEMATICAL BACKGROUND

Numerical methods are of critical importance for modeling and simulation of the optical properties of PCs, including band diagrams and/or isofrequency diagrams, modeling field distributions, and to determine transmission and/or reflection efficiency. In this chapter, numerical methods applied in this dissertation are discussed, including the plane wave expansion method (PWEM), the finite-difference time-domain method (FDTD), and rigorous coupled-wave analysis (RCWA). The purposes and basic principles of these numerical methods are introduced in the following sections. In addition, numerical methods are required to model periodic/quasi-periodic irradiance distributions resulting from the fractional Talbot effect, which are used as design templates to obtain Talbot crystals (details in CHAPTER 4). To this end, related mathematical concepts behind the fractional Talbot effect are also introduced.

3.1 Plane wave expansion method

The PWEM [55, 87-90] is a popular numerical method to calculate band diagrams and isofrequency diagrams of PCs. This approach solves Maxwell's equations as an eigenvalue problem, where the eigenvalues represent the angular frequencies of the existing modes in the PC while the eigenvectors represent the amplitude coefficients of the fields. In the PWEM, the dielectric function and field are expanded by Fourier series in reciprocal space (k -space). Due to slow convergence of the Fourier series for structures with high refractive index contrast (such as metal), the PWEM is best suited to analyze

periodic structures with low to moderate index contrast [89].

In a source-free non-magnetic medium, the two Maxwell's equations relating electric field ($E(r)$) to magnetic field ($H(r)$) are:

$$\nabla \times \vec{E}(r) - i\omega\mu_0\vec{H}(r) = 0 \quad (3.1)$$

$$\nabla \times \vec{H}(r) + i\omega\varepsilon_0\varepsilon(r)\vec{E}(r) = 0 \quad (3.2)$$

where ε_0 and μ_0 are the free-space permittivity and permeability of the material respectively, $\varepsilon(r)$ is the dielectric function, and ω is the angular frequency. Decoupling these equations can lead to the *master equation* [39]:

$$\nabla \times \left(\frac{1}{\varepsilon(r)} \nabla \times \vec{H}(r) \right) = \left(\frac{\omega}{c} \right)^2 \vec{H}(r) \quad (3.3)$$

where c is the speed of light in vacuum. Since the dielectric function is assumed to be periodic, it can be expanded by Fourier series, such that

$$\varepsilon(r) = \sum_{\vec{G}} \varepsilon_G e^{i\vec{G} \cdot \vec{r}} \quad (3.4)$$

where ε_G is the Fourier transform of the dielectric function and \vec{G} are the expansion vectors in reciprocal space. The expansion vectors are a set of finite-numbered plane waves. Based on Bloch's theorem [39, 91], a mode in an infinite PC can be expanded as a sum of an infinite number of plane waves. Therefore, the magnetic field in Eq. (3.3) can be described as [87]:

$$\vec{H}(r) = \sum_{G,l} H_{G,l} e^{i(\vec{k} + \vec{G}) \cdot \vec{r}} \hat{e}_l \quad (3.5)$$

where H_G is the coefficient of the field component along the direction of \hat{e}_l , and \vec{k} is the wave vector. The index l is equal to 1 or 2, so that \hat{e}_l represents the two unit vectors

perpendicular to the propagating direction $\vec{k} + \vec{G}$ (i.e. \hat{e}_1 , \hat{e}_2 , and $\vec{k} + \vec{G}$ are perpendicular to each other). When Eq. (3.4) and Eq. (3.5) substitute back into Eq. (3.3), a set of linear equations is formed [88, 92]:

$$\sum_{\vec{G}'} \left| \vec{k} + \vec{G} \right| \left| \vec{k} + \vec{G}' \right| \varepsilon^{-1}(\vec{G} - \vec{G}') \begin{bmatrix} \hat{e}_2 \cdot \hat{e}_2' & -\hat{e}_2 \cdot \hat{e}_1' \\ -\hat{e}_1 \cdot \hat{e}_2' & \hat{e}_1 \cdot \hat{e}_1' \end{bmatrix} \begin{bmatrix} H_{1,G'} \\ H_{2,G'} \end{bmatrix} = \left(\frac{\omega}{c} \right)^2 \begin{bmatrix} H_{1,G} \\ H_{2,G} \end{bmatrix} \quad (3.6)$$

Eq. (3.6) is an eigenvalue problem [39, 93] and can be solved using an eigensolver, such as MATLAB™. In a 2D PWEM problem, assume $\vec{k} + \vec{G}$, \hat{e}_1 are in the x-y plane, and \hat{e}_2 is along the z-direction. Then H_1 corresponds to TM polarization (H components are only in x-y plane [39]) while H_2 corresponds to TE polarization (H components are along z-direction [39]). One may further specify Eq.(3.6) to two different equations for TM and TE polarizations respectively [94]:

$$\text{TM: } \sum_{\vec{G}'} \left| \vec{k} + \vec{G} \right| \left| \vec{k} + \vec{G}' \right| \varepsilon^{-1}(\vec{G} - \vec{G}') H_{1,G'} = \left(\frac{\omega}{c} \right)^2 H_{1,G} \quad (3.7a)$$

$$\text{TE: } \sum_{\vec{G}'} (\vec{k} + \vec{G}) \cdot (\vec{k} + \vec{G}') \varepsilon^{-1}(\vec{G} - \vec{G}') H_{2,G'} = \left(\frac{\omega}{c} \right)^2 H_{2,G} \quad (3.7b)$$

The following procedures describe the implementation of the PWEM:

1. Define primitive lattice vectors (\vec{t}_1 , \vec{t}_2 , \vec{t}_3) of a unit cell
2. Define dielectric function $\varepsilon(r)$ of the unit cell
3. Construct expansion vectors in terms of the reciprocal lattice vectors (\vec{T}_1 , \vec{T}_2 , \vec{T}_3).

Obtain the convolution matrix $\varepsilon(\vec{G} - \vec{G}')$ by applying Fourier transform to $\varepsilon(r)$

4. Construct the “global matrix” for the eigenvalue problem, which is

$$\sum_{\vec{G}'} \left| \vec{k} + \vec{G} \right| \left| \vec{k} + \vec{G}' \right| \varepsilon^{-1}(\vec{G} - \vec{G}') \begin{bmatrix} \hat{e}_2 \cdot \hat{e}_2' & -\hat{e}_2 \cdot \hat{e}_1' \\ -\hat{e}_1 \cdot \hat{e}_2' & \hat{e}_1 \cdot \hat{e}_1' \end{bmatrix}$$

5. Solve the eigenvalue problem

In procedure 3, the number of expansion vectors (the number of plane waves used) is related to the accuracy of the calculated results. The more plane waves used, the closer the calculated results will be to the converged values. However, this increases the required computational memory and time. A convergence study is necessary to determine the proper number of plane waves to use. In this dissertation, the number of plane waves is described by the following manner: assume a plane wave in the expansion vector set is labeled by an index (p, q, r) , then the number of plane waves in each direction is $2P+1$, $2Q+1$, and $2R+1$ respectively, where $|p| \leq P$, $|q| \leq Q$, $|r| \leq R$ and P, Q, R are integers. The total number of plane waves is then $(2P+1)*(2Q+1)*(2R+1)$. In procedure 4, if the structures under study do not have simple geometries allowing the use of the analytical Fourier transform, then the numerical fast Fourier transform (FFT) has to be applied [88].

In this work, the PWEM is used to obtain band diagrams and isofrequency diagrams of PCs. Three software packages are chosen: an in-house source code written in MATLAB is mainly used for 2D simulation (Appendix A); a commercial software package Rsoft BandSOLVETM [95] is used to confirm the results. Lastly, a freely distributed software package, the MIT Photonic Bands (MPB) package [87], is used for 3D simulation.

3.2 Finite-difference time-domain method

The FDTD method [96, 97] is a rigorous solution to Maxwell's equations, and is a flexible technique for broadband characterization and field visualization. It allows the simulation of almost any structure, including non-periodic and complicated structures. In addition, this scattering algorithm can also be used to calculate eigen-modes and obtain

band diagrams.

In the FDTD method, the structures under study are represented by discrete grid points (the Yee's mesh [97]) in the spatial domain. The E and H field components at all grid points are then computed by iterating the time-dependent Maxwell's equations over time. In a source-free medium, the time-dependent Maxwell's equations can be written as six scalar equations, where the temporal change in the electric field is dependent on the spatial variation of the magnetic field, and vice versa:

$$\frac{\partial}{\partial t} E_x = -\frac{1}{\varepsilon} \left(\frac{\partial}{\partial y} H_z - \frac{\partial}{\partial z} H_y \right) \quad (3.8a)$$

$$\frac{\partial}{\partial t} E_y = -\frac{1}{\varepsilon} \left(\frac{\partial}{\partial z} H_x - \frac{\partial}{\partial x} H_z \right) \quad (3.8b)$$

$$\frac{\partial}{\partial t} E_z = -\frac{1}{\varepsilon} \left(\frac{\partial}{\partial x} H_y - \frac{\partial}{\partial y} H_x \right) \quad (3.8c)$$

$$\frac{\partial}{\partial t} H_x = -\frac{1}{\mu} \left(\frac{\partial}{\partial z} E_y - \frac{\partial}{\partial y} E_z \right) \quad (3.8d)$$

$$\frac{\partial}{\partial t} H_y = -\frac{1}{\mu} \left(\frac{\partial}{\partial x} E_z - \frac{\partial}{\partial z} E_x \right) \quad (3.8e)$$

$$\frac{\partial}{\partial t} H_z = -\frac{1}{\mu} \left(\frac{\partial}{\partial y} E_x - \frac{\partial}{\partial x} E_y \right) \quad (3.8f)$$

The FDTD method discretizes these equations via central differences in time and space: the E and H field components are interlaced on the Yee's mesh in the spatial domain (FIGURE 3.1), and time is broken up into discrete steps of Δt . Maxwell's equations are iteratively solved by alternatively computing the E and H fields at subsequent $\Delta t/2$ intervals. For example, the E field components are computed at times $t=m\Delta t$ while the H field components are computed at $t=(m+0.5)\Delta t$, where m is an integer. This method results in six equations that can be used to compute the field at a given mesh point, denoted by integers (i, j, k) :

$$E_{x(i,j,k)}^{n+1} = E_{x(i,j,k)}^{n+1} + \frac{\Delta t}{\epsilon \Delta y} (H_{z(i,j+1,k)}^{n+0.5} - H_{z(i,j,k)}^{n+0.5}) - \frac{\Delta t}{\epsilon \Delta z} (H_{y(i,j,k+1)}^{n+0.5} - H_{y(i,j,k)}^{n+0.5}) \quad (3.9a)$$

$$E_{y(i,j,k)}^{n+1} = E_{y(i,j,k)}^{n+1} + \frac{\Delta t}{\epsilon \Delta z} (H_{x(i,j+1,k)}^{n+0.5} - H_{x(i,j,k)}^{n+0.5}) - \frac{\Delta t}{\epsilon \Delta x} (H_{z(i,j,k+1)}^{n+0.5} - H_{z(i,j,k)}^{n+0.5}) \quad (3.9b)$$

$$E_{z(i,j,k)}^{n+1} = E_{z(i,j,k)}^{n+1} + \frac{\Delta t}{\epsilon \Delta x} (H_{y(i,j+1,k)}^{n+0.5} - H_{y(i,j,k)}^{n+0.5}) - \frac{\Delta t}{\epsilon \Delta y} (H_{x(i,j,k+1)}^{n+0.5} - H_{x(i,j,k)}^{n+0.5}) \quad (3.9c)$$

$$H_{x(i,j,k)}^{n+0.5} = H_{x(i,j,k)}^{n+0.5} + \frac{\Delta t}{\epsilon \Delta y} (H_{z(i,j+1,k)}^{n+0.5} - H_{z(i,j,k)}^{n+0.5}) - \frac{\Delta t}{\epsilon \Delta z} (H_{y(i,j,k+1)}^{n+0.5} - H_{y(i,j,k)}^{n+0.5}) \quad (3.9d)$$

$$H_{y(i,j,k)}^{n+0.5} = H_{y(i,j,k)}^{n+0.5} + \frac{\Delta t}{\epsilon \Delta z} (H_{x(i,j+1,k)}^{n+0.5} - H_{x(i,j,k)}^{n+0.5}) - \frac{\Delta t}{\epsilon \Delta x} (H_{z(i,j,k+1)}^{n+0.5} - H_{z(i,j,k)}^{n+0.5}) \quad (3.9e)$$

$$H_{z(i,j,k)}^{n+0.5} = H_{z(i,j,k)}^{n+0.5} + \frac{\Delta t}{\epsilon \Delta x} (H_{y(i,j+1,k)}^{n+0.5} - H_{y(i,j,k)}^{n+0.5}) - \frac{\Delta t}{\epsilon \Delta y} (H_{x(i,j,k+1)}^{n+0.5} - H_{x(i,j,k)}^{n+0.5}) \quad (3.9f)$$

where Δx , Δy , Δz are the grid spacings in their respective directions.

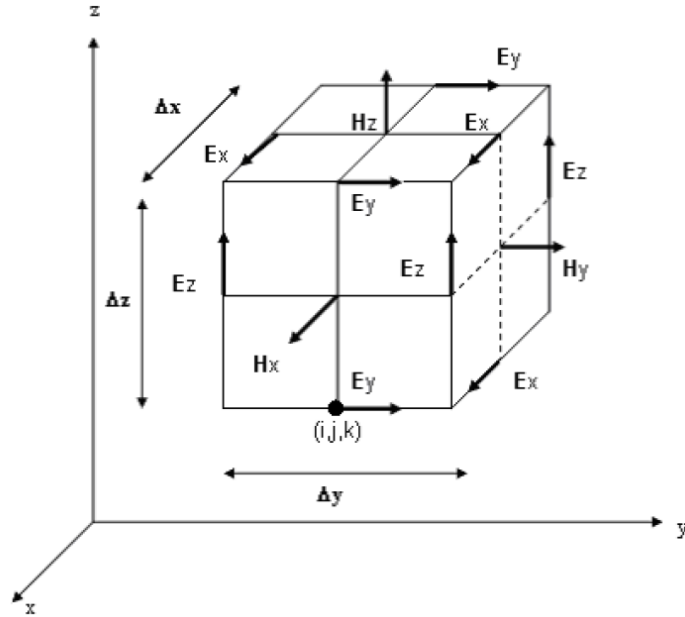


FIGURE 3.1: Yee's mesh [97]

The weakness of the FDTD method, however, is computational expense. The amount of required memory scales inversely with the grid size needed to approximate the profile. While a larger grid size is preferred for the sake of saving computational memory, the grid size must meet the following criteria. First, the grid spacing must be small

enough to resolve the finest feature of the structure. Second, the grid spacing must be small enough to resolve the shortest wavelength of interest. It is typical to use $\lambda/10 \sim \lambda/30$ for the grid spacing, where λ is the shortest wavelength in the region of higher refractive index material.

In this dissertation, a commercial software package, Rsoft FullWAVETM [98] is used to implement the FDTD method. Periodic boundary conditions and perfectly matched layers (PMLs) [99] are both considered for a chosen limited size PC. Dielectric structure extending into the PML can be treated as if it extends to infinity.

3.3 Rigorous coupled-wave analysis

RCWA [100-102] calculates the diffraction efficiency and field distribution for periodic structures with low to moderate index contrast. It is a fully-vectorial solution of Maxwell's equations, and is thus suitable for structures with periods at and below the scale of the illuminating wavelength. RCWA is a semi-analytical method, where the wave equation is solved analytically in the longitudinal direction and periodic boundary conditions are applied in the transverse direction. In other words, the periodic structures under study are assumed extended to infinity in the transverse direction and may have arbitrary variations in the longitudinal direction, as long as the two semi-finite regions adjacent to the periodic structure are homogenous. Therefore, RCWA is usually used in the design process of applications involving subwavelength structures, PCs, and other grating-assisted devices.

To implement the RCWA method, structures are divided into layers that are uniform in the longitudinal direction. In each layer, the electromagnetic fields are represented as a sum of coupled waves (or spatial harmonics [89]). A periodic dielectric

function is represented using Fourier harmonics. Each coupled wave is related to a Fourier harmonic, allowing Maxwell's equations to be solved in the Fourier domain as an eigen-value problem. The eigen-vectors characterize the spatial field distributions in each layer while the eigen-values indicate the longitudinal behavior in terms of a complex propagation constant which incorporates loss, gain, and coupling between modes. The overall diffraction efficiencies are calculated at the end of simulation by applying the boundary conditions at the interfaces of the layers. For simple structures that can be described well with few Fourier series terms, RCWA is especially fast and efficient.

The derivation of RCWA starts from expanding Maxwell's curl equations (Eq. (3.1) and Eq. (3.2)) to six coupled equations:

$$\frac{\partial}{\partial y} E_z - \frac{\partial}{\partial z} E_y = i\omega\mu H_x \quad (3.10a)$$

$$\frac{\partial}{\partial z} E_x - \frac{\partial}{\partial x} E_z = i\omega\mu H_y \quad (3.10b)$$

$$\frac{\partial}{\partial x} E_y - \frac{\partial}{\partial y} E_x = i\omega\mu H_z \quad (3.10c)$$

$$\frac{\partial}{\partial y} H_z - \frac{\partial}{\partial z} H_y = i\omega\varepsilon_0\varepsilon_{rx} E_x \quad (3.10d)$$

$$\frac{\partial}{\partial z} H_x - \frac{\partial}{\partial x} H_z = i\omega\varepsilon_0\varepsilon_{ry} E_y \quad (3.10e)$$

$$\frac{\partial}{\partial x} H_y - \frac{\partial}{\partial y} H_x = i\omega\varepsilon_0\varepsilon_{rz} E_z \quad (3.10f)$$

In these equations, the dielectric material of a chosen layer is characterized by a diagonal permittivity tensor with respect to the principle axes. The diagonal elements are ε_{rx} , ε_{ry} , and ε_{rz} . By substituting Eq. (3.10c, f) into Eq. (3.10a, b, d, e), Maxwell's equations can be described by the following transverse format:

$$\frac{\partial}{\partial z} E_x = -\frac{i}{\omega \varepsilon_0} \frac{\partial}{\partial x} \frac{1}{\varepsilon_{rz}} H_x + \left(\frac{i}{\omega \varepsilon_0} \frac{\partial}{\partial x} \frac{1}{\varepsilon_{rz}} \frac{\partial}{\partial x} + i\omega\mu \right) H_y \quad (3.11a)$$

$$\frac{\partial}{\partial z} E_y = \left(-\frac{i}{\omega \varepsilon_0} \frac{\partial}{\partial y} \frac{1}{\varepsilon_{rz}} \frac{\partial}{\partial y} - i\omega\mu \right) H_x + \frac{i}{\omega \varepsilon_0} \frac{\partial}{\partial y} \frac{1}{\varepsilon_{rz}} \frac{\partial}{\partial x} H_y \quad (3.11b)$$

$$\frac{\partial}{\partial z} H_x = -\frac{i}{\omega\mu} \frac{\partial}{\partial x} \frac{\partial}{\partial y} E_x + \left(-\frac{i}{\omega\mu} \frac{\partial}{\partial x} \frac{\partial}{\partial x} - i\omega \varepsilon_0 \varepsilon_{ry} \right) E_y \quad (3.11c)$$

$$\frac{\partial}{\partial z} H_y = \left(\frac{i}{\omega\mu} \frac{\partial}{\partial y} \frac{\partial}{\partial y} + i\omega \varepsilon_0 \varepsilon_{rx} \right) E_x - \frac{i}{\omega\mu} \frac{\partial}{\partial y} \frac{\partial}{\partial x} E_y \quad (3.11d)$$

Based on Bloch's theorem, field components in a periodic layer can be described as:

$$E_x = e^{i(k_x x + k_y y)} \sum_p \sum_q e^{i\left(\frac{2\pi}{\Lambda_x} px + \frac{2\pi}{\Lambda_y} qy\right)} \sum_m a_{x,m,p,q} (f_m e^{ik_m z} + g_m e^{-ik_m z}) \quad (3.12a)$$

$$E_y = e^{i(k_x x + k_y y)} \sum_p \sum_q e^{i\left(\frac{2\pi}{\Lambda_x} px + \frac{2\pi}{\Lambda_y} qy\right)} \sum_m a_{y,m,p,q} (f_m e^{ik_m z} + g_m e^{-ik_m z}) \quad (3.12b)$$

$$H_x = e^{i(k_x x + k_y y)} \sum_p \sum_q e^{i\left(\frac{2\pi}{\Lambda_x} px + \frac{2\pi}{\Lambda_y} qy\right)} \sum_m b_{x,m,p,q} (f_m e^{ik_m z} - g_m e^{-ik_m z}) \quad (3.12c)$$

$$H_y = e^{i(k_x x + k_y y)} \sum_p \sum_q e^{i\left(\frac{2\pi}{\Lambda_x} px + \frac{2\pi}{\Lambda_y} qy\right)} \sum_m b_{y,m,p,q} (f_m e^{ik_m z} - g_m e^{-ik_m z}) \quad (3.12d)$$

Substituting Eq. (3.12) into Eq. (3.11) results in an eigen-value equation that can be solved as a regular eigen-value problem.

In this dissertation, a commercial RCWA software packages, GSolver© [103], is used to calculate the complex field coefficients needed in the rigorous diffraction theorem to obtain periodic/quasi-periodic irradiance distributions based on the Talbot effect.

TABLE 3.1 lists and describes all the numerical methods used.

Numerical Method	Purpose	Software Used
Rigorous couple wave analysis (RCWA)	To obtain complex coefficients required in the propagation field from an optical grating (Eq. (3.16))	GSolver ©
Plane wave expansion method (PWEM)	To obtain EFCs/EFSs of a PC	1. Custom source code using MATLAB 2. Rsoft BandSOLVE™ 3. MPB package
Finite domain time domain method (FDTD)	To simulate beam propagation and to determine transmission efficiency	Rsoft FullWAVE™

TABLE 3.1: List of numerical methods used and their purposes

3.4 Mathematical background of the fractional Talbot effect

The fractional Talbot effect is a self-imaging property of periodic structures (such as optical gratings), that will be applied to generate periodic/quasi-periodic irradiance distributions for Talbot crystals (CHAPTER 4). To this end, the electromagnetic theory behind the fractional Talbot effect is introduced in this section. A 1D optical grating is used as a simple example to describe the concept.

Assume a 1D grating (with periodicity in x-direction) is illuminated with coherent plane waves, where the incident and propagating medium are both homogeneous with refractive index of n_i and n_t respectively (FIGURE 3.2). The transmitted wave fields beyond the grating (along z-direction) can be expressed in the form of the Rayleigh expansion [104-106].

$$U_T(x; z) = \sum_{m=-\infty}^{\infty} T_m e^{i(\bar{k}_m \cdot \bar{x} + \bar{l}_m \cdot \bar{z})} \hat{x} = \sum_{m=-\infty}^{\infty} T_m e^{i(k_m x + l_m z)} \hat{x} \quad (3.13)$$

The coefficient T_m represents the complex amplitudes of the m^{th} transmitted diffraction

order; \vec{k}_m and \vec{t}_m are the wave vectors in the incident medium and propagating medium respectively. Based on Bloch's theorem and surface-parallel k -vector conservation, we have [39, 105]:

$$k_m = n_i k \sin \theta_i + \frac{2\pi m}{\Lambda} \quad (3.14)$$

$$t_m^2 = (n_t k)^2 - k_m^2 \quad (3.15)$$

where Λ is the grating period along the x-direction, and k is the wave number in vacuum.

Assuming normal incidence ($\theta_i=0^\circ$) for simplicity, Eq. (3.13) can be rewritten as:

$$U_T(x; z) = \sum_{m=-\infty}^{\infty} T_m e^{i \left(\frac{2\pi m}{\Lambda} x + \sqrt{(n_t k)^2 - \left(\frac{2\pi m}{\Lambda} \right)^2} z \right)} \hat{x} \quad (3.16)$$

Eq. (3.16) describes the wave field distributions after light passes through an optical grating. The complex coefficient in Eq. (3.16), T_m , can be determined by applying the electromagnetic boundary conditions at the boundary of the grating and the propagating medium ($z=0$ in FIGURE 3.2) [35, 105]. At the boundary, generally, the various components of the electric and magnetic fields are coupled through Maxwell's equations and cannot be treated independently [35]. In many cases where the grating period is much larger (typically five times larger or more) than the illuminating wavelength ($\Lambda \gg \lambda$), the coupling effect of the boundary conditions on the electric and magnetic fields may be small [35]. Thus scalar diffraction theory may be used for simple calculation [35, 36]. This means the complex coefficients, T_m , in Eq. (3.16) can be expressed by Fourier transform of the input distribution, $U_T(x; z=0)$ [36]. However, if the grating period is approximately the same scale as the illuminating wavelength ($\Lambda \sim \lambda$), the complex coefficients in Eq. (3.16) then have to be obtained using rigorous numerical

methods, such as RCWA, as introduced in Section 3.3.

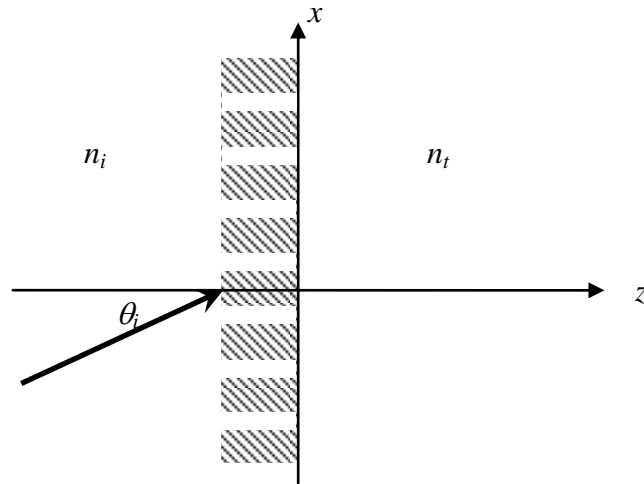


FIGURE 3.2: Geometry for diffraction of a plane wave by a 1D optical grating

In this dissertation, rigorous numerical methods are required to calculate the irradiance distributions because we intentionally chose a grating period on the same scale as the incident wavelength. In this case, the resulting periodic/quasi-periodic irradiance is relatively simple and can be considered as a design template for 2D complex PCs. This concept and approach will be discussed in more detail in Section 4.4. An in-house source code to calculate the irradiance distributions from a 1D phase grating was written in MATLAB (Appendix B). This code is based on the electromagnetic theory described in this section.

CHAPTER 4: INTRODUCTION TO TALBOT CRYSTALS

In this chapter, a group of non-conventional 2D PC structures is introduced for self-collimation studies. These PC structures are inspired by the periodic/quasi-periodic irradiance distributions resulting from the fractional Talbot effect [35-38]; thus such PCs are referred to as “Talbot crystals.” Talbot crystals generally have more design flexibility compared with conventional PCs. In this dissertation, 2D Talbot crystals are considered as options to realize broadband “all-angle” (in-plane) self-collimation as introduced in Section 2.4. Talbot crystals have the potential to support these desired properties because Talbot crystals are usually complex lattice structures with 2D rectangular or rhombus lattice geometries, where complex lattice structures and rectangular lattice structures have been demonstrated as good candidates for the purpose mentioned [2, 3, 6].

In the following sections, the fractional Talbot effect and the methods used to obtain Talbot crystals will be introduced. Derivation of the geometries of Talbot crystals is provided and other advantages of Talbot crystals will also be discussed.

4.1 The fractional Talbot effect

The Talbot effect refers to a self-imaging property of periodic structures due to near field diffraction and interference. When collimated coherent light illuminates a periodic structure (including but not limited to an optical grating), periodic and/or quasi-periodic field distributions are formed along the propagating direction through Talbot self-imaging [35, 36, 38, 107, 108]. The longitudinal distance between the periodic

structure and the location of the first self-image is defined as one ‘‘Talbot distance’’ (Z_T), which is a function of the illuminating wavelength (λ) and the period of the periodic structure (Λ) as described in the following equation.

$$Z_T = \frac{\lambda}{1 - \sqrt{1 - \left(\frac{\lambda}{\Lambda}\right)^2}} \quad (4.1)$$

Derivation of the Talbot distance is included in Appendix C. Because of the Talbot effect, the field distribution immediately following a periodic structure is replicated at integer multiples of the Talbot distance from the periodic structure. In addition, multiple phase-shifted replicas of the input field distribution are also created at different fractions of the Talbot distance. This is referred to as the fractional Talbot effect.

FIGURE 4.1 gives a simple example showing the basic concept of the fractional Talbot effect. The pattern shown in FIGURE 4.1 is the simulation result of the irradiance distribution generated from a simple 1D binary amplitude grating. The grating is assumed placed in the x-y plane ($z=0$) with periodicity along the x-direction. If the grating is normally illuminated from the left by a coherent collimated beam (plane waves), periodic/quasi-periodic irradiance distributions are formed along the +z-direction (refer to FIGURE 4.2 for setup orientation). The displayed area in FIGURE 4.1 is Z_T (length) by $2*\Lambda$ (width) with arbitrary units. As shown in the figure, the patterns at $Z_T/2$ and Z_T have the original grating period; the patterns at $Z_T/4$, $Z_T/6$, and $Z_T/8$ have half, one-third, and quarter of the grating period, respectively. Therefore, one may observe single images at $Z_T/2$ and Z_T ; double, triple, and quadruple images at $Z_T/4$, $Z_T/6$, and $Z_T/8$, respectively. Additional images can also be observed at other fractions of the Talbot distance.

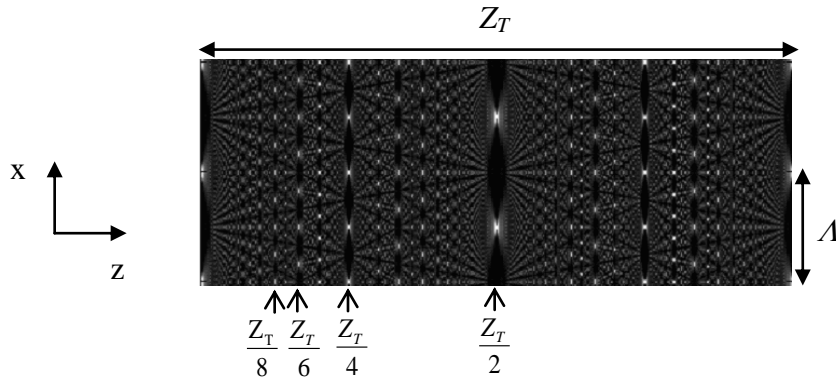


FIGURE 4.1: 2D irradiance profile from 1D binary amplitude grating (simulation result). The image displayed in the figure is Z_T in length (z-direction) and $2A$ in width (x-direction) with arbitrary units. The grating has $1/24$ ($\sim 4.2\%$) duty cycle; the irradiance distribution is calculated based on scalar diffraction theorem assuming the grating period is much larger than the incident wavelength.

4.2 Talbot crystal geometries

The geometries of the Talbot crystals are normally rhombus or rectangular lattices, but may also include triangular lattices and square lattices in some special cases. This can be shown by applying the following simple derivation.

As mentioned in Eq. (4.1), Talbot distance (Z_T) can be described in terms of the grating period (A) and the incident wavelength (λ). In order to assure the Talbot distance is a positive real number, the denominator of Eq. (4.1) must be a positive real number. Mathematically, this implies that the grating period should be at least equal to or larger than the incident wavelength ($A \geq \lambda$).

Assume $A = m \cdot \lambda$, where m is a positive real number and $m \geq 1$. Eq. (4.1) can be rewritten as

$$Z_T = \frac{\lambda}{1 - \sqrt{1 - \left(\frac{\lambda}{m\lambda}\right)^2}} = \frac{m\lambda}{m - \sqrt{m^2 - 1}} \quad (4.2)$$

Since $\frac{m\lambda}{m - \sqrt{m^2 - 1}} \geq m\lambda$, we have

$$Z_T \geq \Lambda \quad (4.3)$$

According to this result, the Talbot distance must be equal or larger than the grating period. This implies that the irradiance distributions based on the fractional Talbot effect have longer longitudinal periods (along the propagation direction; z-direction as in FIGURE 4.1) than lateral periods (along x-direction). Therefore, 2D Talbot crystals are generally rhombus or rectangular lattice structures. These structures have relatively lower geometrical symmetry, which have a better chance to support broadband “all-angle” self-collimation as mentioned earlier (Section 2.5.2 and Section 2.6).

4.3 Realization of the fractional Talbot effect

To realize the fractional Talbot effect experimentally, a collimated coherent light source and a periodic structure are essential. The required periodic structure could be any periodic optical component, including optical gratings, phase masks, and photonic crystals. The periodicity of the periodic structure could be in 1D, 2D, and even 3D. If 1D periodic structures are used, 2D periodic/quasi-periodic irradiance distributions are generated (in x-z plane as in FIGURE 4.2). Since the irradiance in the third direction (y-direction) is assumed uniform, it is usually not displayed for the sake of convenience. On the other hand, if 2D or 3D periodic structures are used, then 3D periodic/quasi-periodic irradiance distributions are formed based on the same principle. In this dissertation, only 1D optical gratings are considered for the self-collimation study.

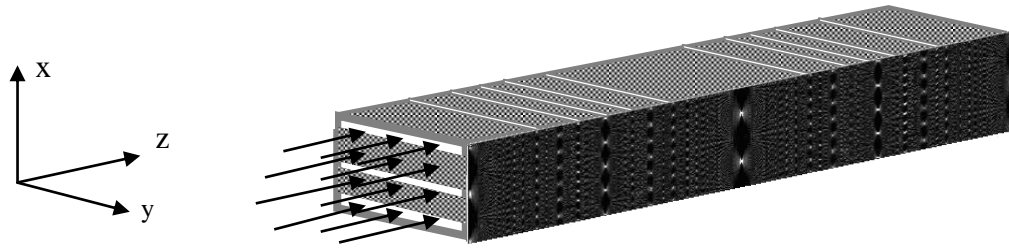


FIGURE 4.2: Schematic diagram of the setup to generate periodic/quasi-periodic irradiance distribution based on the fractional Talbot effect. Plane waves are normally incident to the periodic structure (optical grating) as indicated by the array of arrows.

4.4 Manipulating the irradiance distributions

The irradiance distributions resulting from the fractional Talbot effect can be easily manipulated through the control of the illuminating wavelength and the choice of the optical grating. A wide variety of novel irradiance distributions can be synthesized through design of the grating structures. As will be introduced in Section 4.5, these irradiance distributions will be used as the design templates for Talbot crystals. Therefore, Talbot crystals generally have significant design flexibility that can enable desired optical properties (in our case for example, broadband “all-angle” self-collimation).

There are generally two kinds of optical gratings available for this purpose, amplitude gratings and phase gratings. Amplitude gratings modulate the irradiance of the illuminating light while phase gratings modulate the phase. The fundamental behavior of the fractional Talbot effect is the same for both kinds. However, phase gratings give additional degrees of freedom in engineering more complex irradiance distributions in fractional Talbot planes. The irradiance distribution shown in FIGURE 4.1 is generated from a 1D amplitude grating. The rest of this dissertation will focus on irradiance distributions generated from 1D phase gratings for the reason given above.

For a binary phase grating, grating period (Λ), phase step ($\Delta\phi$), and duty cycle (or

opening factor, which is the ratio of grating opening divided by the grating period) are three main parameters that can affect resulting irradiance distributions. FIGURE 4.3(a)~(c) are sample irradiance distributions generated from 1D phase gratings with different grating periods and/or duty cycles. All the cases in FIGURE 4.3 are simulation results calculated based on rigorous diffraction theory assuming the same incident wavelength ($\lambda=364$ nm) and grating phase step ($\Delta\phi=0.5\pi$). This example shows that the irradiance distributions resulting from the fractional Talbot effect can be very different even if only one grating parameter is changed.

In general, irradiance distributions resulting from a grating with a smaller *period to wavelength ratio* (Λ/λ) and/or larger duty cycle are relatively simple compared with those from a grating with a larger period to wavelength ratio and/or smaller duty cycle. For example, the irradiance distributions shown in FIGURE 4.3 ($\Lambda/\lambda=1.1, 1.5, 1.5$; duty cycle= $1/8$ (12.5 %), $1/8$ (12.5 %), $1/2$ (50 %) in the case of (a), (b), (c) correspondingly) are relatively simple compared with the one given in FIGURE 4.1 ($\Lambda/\lambda \gg 5$; duty cycle= $1/24$ (~ 4.2 %)).

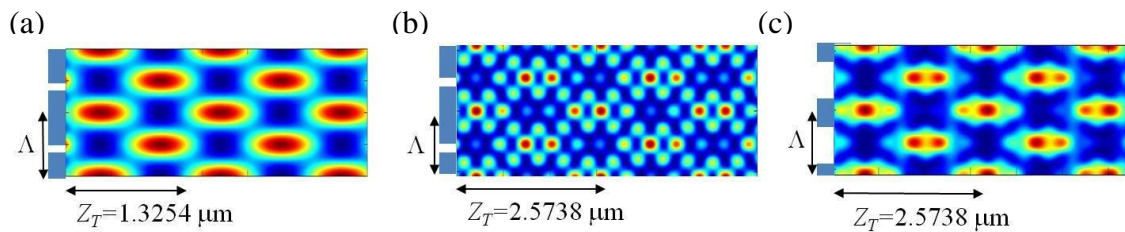


FIGURE 4.3: Examples of irradiance distributions resulting from the fractional Talbot effect. Assume $\lambda=0.364$ μm ; Different grating parameters are used in these cases (a) $\Lambda = 1.1\lambda$; duty cycle=12.5 %; (b) $\Lambda = 1.5\lambda$; duty cycle=12.5 %; (c) $\Lambda = 1.5\lambda$; duty cycle=50 %. The phase step is $\pi/2$ ($\Delta\phi=\pi/2$). (Plots are not to scale.)

4.5 Realization of Talbot crystals

In this dissertation, two methods are considered to realize Talbot crystals. Descriptions of each case are given as follows.

The first method is to assume the irradiance distributions can be directly converted to dielectric structures through exposure of photosensitive materials and subsequent processing, i.e. some Talbot crystals have the potential to be fabricated by a single exposure using the periodic/quasi-periodic irradiance distribution as the exposure light source. For the simple example given in FIGURE 4.2 (1D grating cases), assume a 3D photosensitive material (photosensitive bulk) is placed behind the grating before the light is illuminated. Ideally, since the photosensitive bulk is only crosslinked where the irradiance is higher than a exposure threshold, a 3D structure (with 2D periodicity) is formed in the photosensitive bulk after the irradiance distribution generated in the photosensitive bulk. For simplicity, the examples given later all belong to this case. Similar ideas can be extended to 2D grating cases, where the generated irradiance distributions (the light source) and the resulting Talbot crystals both have 3D periodicity. But such cases are excluded in our discussion. After the exposed photosensitive bulk is developed, a basic Talbot crystal (comprised of the photosensitive material and air) is obtained. If a Talbot crystal made with higher index materials is desired, it can be obtained by infiltrating the basic Talbot structure with the desired material then dissolving the developed photosensitive material. The former process can be done using inverse opal methods [109, 110] and/or atomic layer deposition (ALD) [111].

The second method of realizing Talbot crystals is to use the irradiance distribution as a design template. Talbot crystals are then created by mimicking the main features of

the irradiance distributions. In this case, Talbot crystals can be fabricated through techniques used for conventional 2D PCs, including conventional photo-lithography or direct e-beam or laser writing to expose/draw the desired pattern in the photosensitive material. The developed pattern may be further converted to other dielectric structure with subsequent process, including deposition, etching and/or lift-off.

4.5.1 Talbot crystals directly converted from the irradiance distributions

To convert the irradiance distribution to a dielectric structure, a simple irradiance threshold is assumed for dielectric contours. FIGURE 4.4 shows several examples of resultant Talbot crystals. FIGURE 4.4 (a), (b), and (c) correspond to the irradiance distributions shown in FIGURE 4.3 (a), (b), and (c), assuming the same irradiance threshold. In these examples, areas where the irradiance is higher than the threshold value (40 % of the maximum irradiance) are indicated in red, while areas where the irradiance is lower than the threshold value are indicated in blue. These two colors represent two different media. The red areas can be dielectric material while blue areas imply air, and vice versa, depending on the fabrication method and the type of light sensitive material used. For instance, assume a negative tone light sensitive material is exposed to an irradiance distribution; a dielectric structure can be formed by the remaining areas (the red areas) after subsequent development to remove unexposed portions (the blue areas). As seen in FIGURE 4.4, different Talbot crystals can be obtained based on different irradiance distributions.

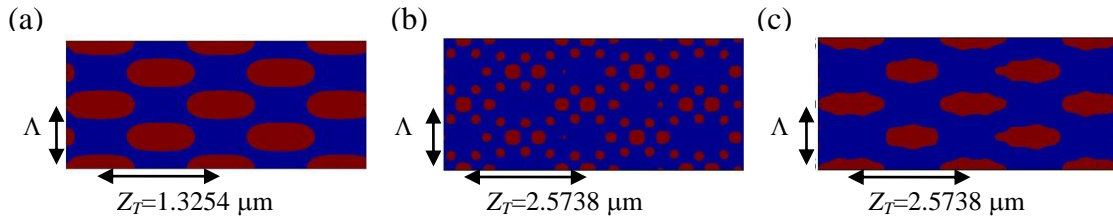


FIGURE 4.4: Examples of the Talbot crystals directly converted from the irradiance distributions by assuming a simple threshold as the contour reference. All of the cases are converted from the previous examples individually by assuming the threshold value is 40 % of the maximum irradiance. (Plots are not to scale.)

In addition, different Talbot crystals can be obtained based on a chosen irradiance distribution but assuming different irradiance thresholds. As in FIGURE 4.5, these dramatically different Talbot crystals result from the irradiance distribution shown in FIGURE 4.3 (a) but assume different irradiance thresholds (40 %, 30 %, and 10 % of the maximum irradiance in FIGURE 4.5 (a), (b), and (c), respectively).

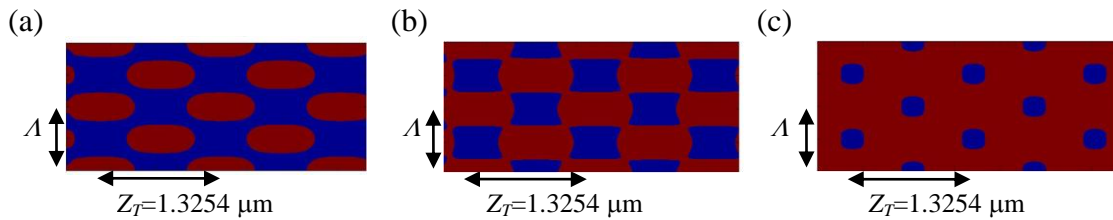


FIGURE 4.5: Examples of the Talbot crystals directly converted from an irradiance distribution by assuming different irradiance thresholds as the contour reference. The threshold value of (a), (b), and (c) is 40 %, 30 %, and 10 % of the maximum irradiance, respectively. (Plots are not to scale.)

4.5.2 Talbot crystals created based on the main features of the irradiance distributions

The second method to obtain Talbot crystals is to use the irradiance distribution as a design template. In this case, Talbot crystals are created by mimicking the main features of the irradiance distributions also in a binary manner (i.e. the resulting Talbot crystals only contain two materials). The example shown in FIGURE 4.6 is one such pattern. The

pattern was created based on the irradiance distribution shown in FIGURE 4.3 (b). This Talbot crystal is very similar to the example shown in FIGURE 4.4 (b), but these two structures are not exactly the same. The created Talbot crystals can be considered complex lattices made by superimposing multiple sub-lattice structures. Such complex structures are usually designed to present combined optical properties from different sub-lattice structures, for example, combining self-collimation behavior with broadband properties [2].

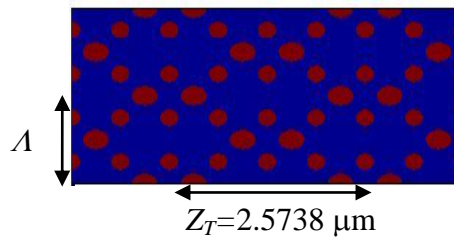


FIGURE 4.6: Example of Talbot crystal created by mimicking the main features of the irradiance distribution resulting from the fractional Talbot effect. This particular example is created based on the second irradiance distribution as in FIGURE 4.3.

Procedures to generate and simulate the properties of Talbot crystals are outlined in TABLE 4.1. After generating the dielectric function describing the Talbot crystal, the dielectric function is imported into the PWEM source code for dispersion property studies, as discussed in more detail in CHAPTER 5.

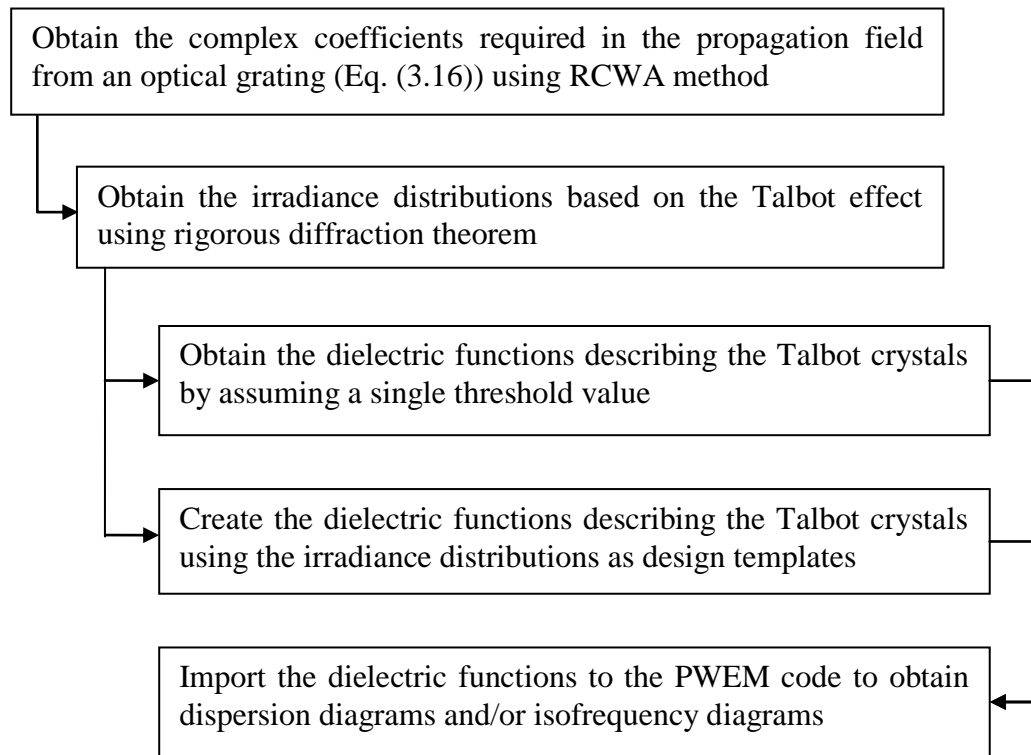


TABLE 4.1: Procedures to generate and simulate the optical properties of Talbot crystals

CHAPTER 5: SELF-COLLIMATION IN COMPLEX RHOMBUS LATTICE TALBOT CRYSTALS

In this chapter, a complex rhombus lattice Talbot crystal is investigated in detail for self-collimation properties. This Talbot crystal was created by mimicking the main features of an irradiance distribution pattern generated from a 1D phase grating, as introduced in Section 4.5.2. A set of custom codes written in MATLAB is used to generate the dielectric function of the structure (Appendix D). The Talbot crystal presented here contains several desired structure geometries for broadband “all-angle” self-collimation. In the following sections, the structure design is described, the EFCs are presented, and the self-collimation performance is discussed in detail. Transmission efficiency and related analysis of some practical performance issues are also given.

5.1 Numerical method and notation for isofrequency diagrams

The EFCs shown in this chapter are calculated by the PWEM as mentioned in Section 3.1. A set of custom codes written in MATLAB is used for this purpose (Appendix A). A commercial software package, Rsoft BandSOLVETM, is also used to confirm the results. The total number of plane waves is chosen so that the calculated eigen-frequencies show convergence to within 1 % of their corresponding converged values. The number of plane waves along each primitive lattice vector is assumed to be proportional to the magnitude of the corresponding reciprocal lattice vector, thus the total number of plane waves used in different structures varies. For the structures under study, the desired convergence is achievable at the fifth band using 11~17 plane waves along

the shorter reciprocal lattice vector (assuming the number of plane waves along the other reciprocal lattice vector is defined accordingly). The number of plane waves used in each structure will be mentioned along with their EFC results. In a band diagram or an isofrequency diagram, eigen-frequencies of Maxwell's equations (ω/c) are typically presented in their normalized form, $\omega a/2\pi c$ or a/λ , where a is the lattice constant. However, since Talbot crystals might not have a well defined lattice constant, we present the eigen-frequencies in the form of $\omega/2\pi c$ or $1/\lambda$ with unit of μm^{-1} .

5.2 Description of the structure

The complex rhombus lattice Talbot crystal discussed in this chapter was created by mimicking the main feature of the irradiance distribution shown in FIGURE 4.3(b). The Talbot crystal consists of two different sized elliptical dielectric rods embedded in an air background (FIGURE 5.1(a)). These elliptical rods are periodically spaced as indicated. The bigger elliptical rods form two identical rhombus sub-lattices (FIGURE 5.1(b)), while the smaller elliptical rods form a rectangular sub-lattice (FIGURE 5.1(c)).

Structure parameters are defined as follows to describe this complex rhombus lattice structure: the diagonals of the rhombus lattice unit cell in the x-direction/y-direction as D_x and D_y ; the semi-major/semi-minor axes of the bigger elliptical rods as Sa_B and Sb_B ; and the semi-major/semi-minor axes of the smaller elliptical rods as Sa_S and Sb_S . The original design adopts the parameters from the dimensions of the irradiance distribution by assuming $\lambda=0.364 \mu\text{m}$ and $A=0.546 \mu\text{m}$ with the corresponding Talbot distance, $Z_T=2.5738 \mu\text{m}$. Since the lateral period (D_y) and the longitudinal period (D_x) of the resulting irradiance distribution are equivalent to the grating period and the Talbot distance respectively, $D_y=A=0.546 \mu\text{m}$ and $D_x=Z_T=2.5738 \mu\text{m}$. Based on the dimensions

of the irradiance pattern shown in FIGURE 4.3(b), the rest of the parameters are chosen as follow: $Sa_B=0.17 \mu\text{m}$, $Sb_B=0.06 \mu\text{m}$, $Sa_S=0.12 \mu\text{m}$, and $Sb_S=0.05 \mu\text{m}$.

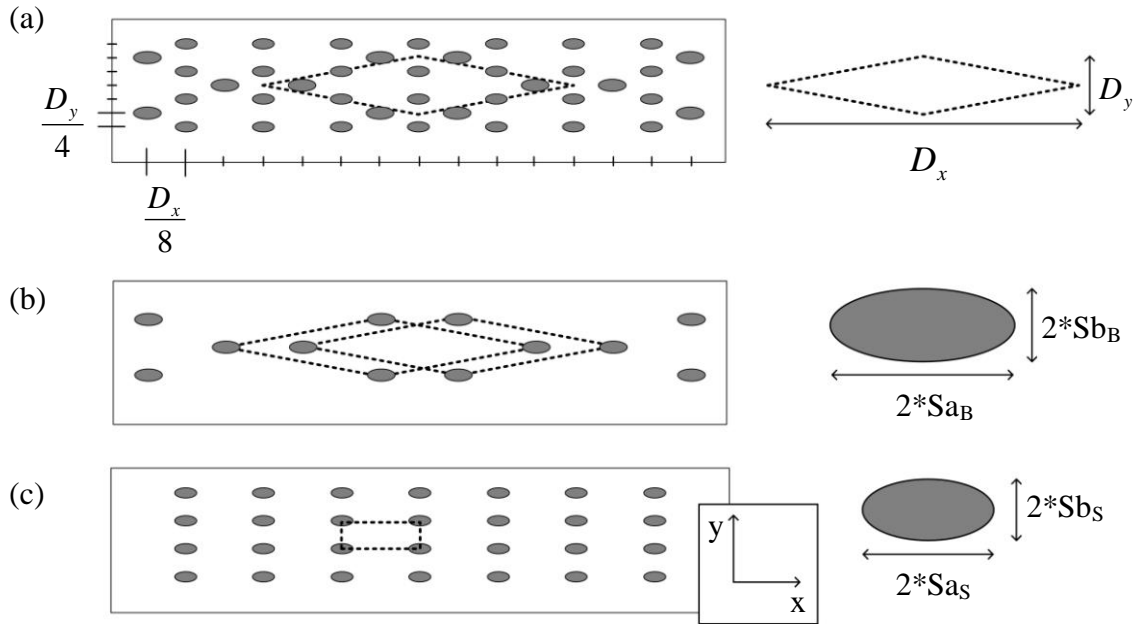


FIGURE 5.1: Complex rhombus lattice structure with elliptical rods embedded in air background. This structure can be considered a superposition of two rhombus sub-lattices and a rectangular one as shown in (b) and (c), respectively. Dotted lines indicate the unit cell of the structure and the sub-lattices. The two identical rhombus sub-lattices are related by a horizontal shift.

5.3 Comparison of structures made of different materials

Here we consider two different dielectric materials to compose the elliptical rods in an air background. The refractive indexes used in the numerical simulation are 1.642 and 3.464, corresponding to possible materials such as a photo-sensitive material (SU-8, $n=1.653\sim 1.52$ within the range 325 nm~1650 nm [112]), and silicon (Si, $n=3.5193\sim 3.4321$ ($\epsilon=12.4\sim 11.8$) within the range 1200 nm~3500 nm [113]). SU-8 is a negative photoresist commonly used for micro-electro-mechanical systems (MEMS), and is a potential material to realize Talbot crystals directly converted from the irradiance

distributions resulting from the fractional Talbot effect (Section 4.5.1). For simplicity, the refractive index in each case is assumed wavelength-independent throughout any wavelength range of interest.

First, the refractive index of the rods is assumed $n=1.642$. FIGURE 5.2(a) shows the fifth band EFCs of the complex rhombus lattice structure mentioned for TM polarization. The total number of plane waves used was 297 (11 along one reciprocal lattice vector; 27 along the other). The rectangular-like EFCs at frequencies about $1.4 \mu\text{m}^{-1}$ to $1.45 \mu\text{m}^{-1}$ ($\lambda=689 \text{ nm} \sim 714 \text{ nm}$; $\Delta\lambda/\lambda_c=3.6 \%$) imply potential self-collimation phenomenon. The EFCs at $1.4 \mu\text{m}^{-1}$ ($\lambda=714 \text{ nm}$) are displayed in FIGURE 5.2(b). In the figure, the dashed circle is the corresponding air-contour at the same wavelength and the dashed parallel lines are the construction lines for surface-parallel k -vector conservation, assuming the air-PC interface is along the Γ - M_1 direction. There are several separate flat EFCs along the Γ - K_3 direction, implying the self-collimation phenomenon will occur in separate angular ranges. These ranges are $|\theta_i| < 2^\circ$, $12^\circ < |\theta_i| < 18.5^\circ$, $31.5^\circ < |\theta_i| < 38^\circ$ and $54.5^\circ < |\theta_i| < 66^\circ$ as indicated by the shaded areas. Light incident from other angles will be refracted to other directions (EFC is not parallel to the air-crystal interface) or cannot be coupled into this structure (the construction line does not intersect with the EFC, i.e. such modes do not exist in the PC structure based on k -vector conservation). Similar analysis can be applied to other wavelengths from 689 nm to 714 nm. As a result, using $n=1.642$ as the refractive index of the rods only shows limited-angle self-collimation within the wavelength range mentioned.

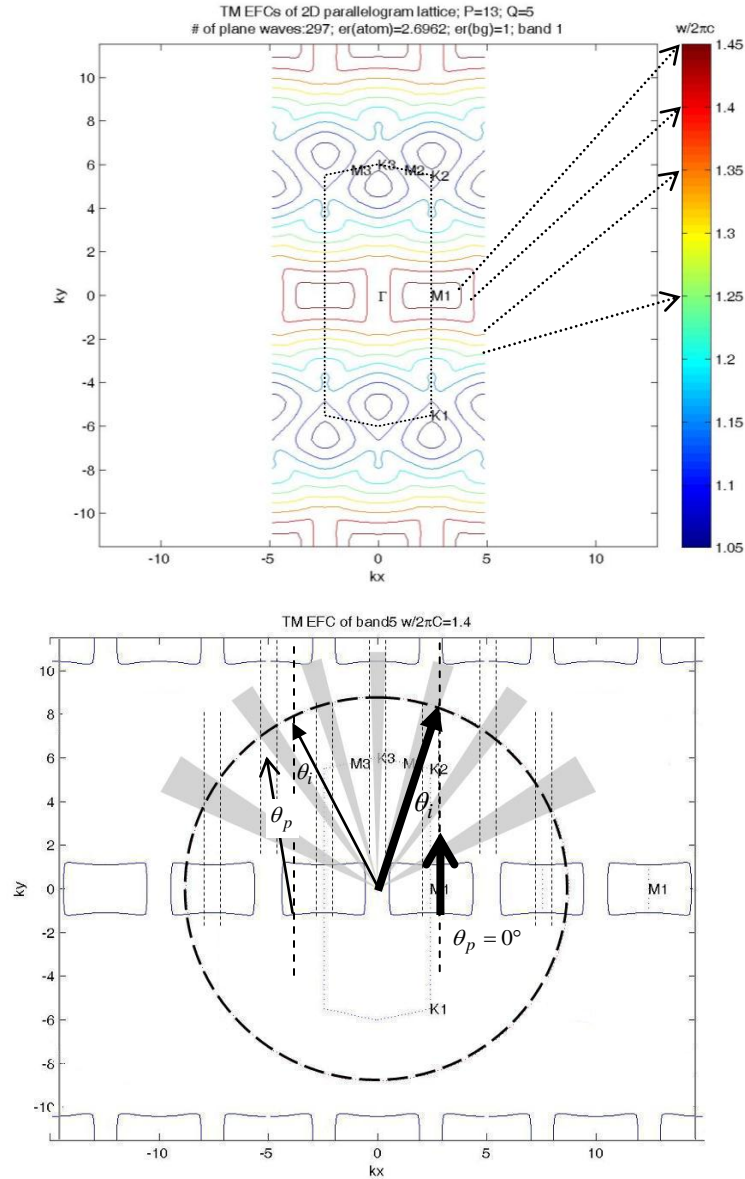


FIGURE 5.2: (a) Fifth band EFCs for TM polarization of the Talbot crystal shown in FIGURE 5.1(a). Hexagonal area (dotted line) is the first BZ and special k -points are indicated in the figure. (b) Fifth band EFCs at frequency of $1.4 \mu\text{m}^{-1}$ ($\lambda=714 \text{ nm}$). The dashed circle is the air contour at the same frequency, and dashed parallel lines are construction lines for surface-parallel k -vector conservation. The shaded areas indicate the seven ranges of the incident angles that exhibit self-collimation behavior. Two examples of incident light are given here. Bold arrows show the case where light is incident within the angular self-collimation range ($\theta_p=0^\circ$); thin arrows represent the case where light is not incident from those angle ranges showing self-collimation phenomenon ($\theta_p \neq 0^\circ$). The arrow style (\rightarrow) indicates the directions of incident light while the arrow style (\Rightarrow) shows the directions of refracted light.

On the other hand, if the refractive index of the rods is assumed $n=3.464$, the complex rhombus lattice structure shows a broadband open wavy EFCs (in short, “wavy” EFSs) from $0.66 \mu\text{m}^{-1}$ to $0.78 \mu\text{m}^{-1}$ ($\lambda=1282 \text{ nm} \sim 1515 \text{ nm}$) at the fifth band for TM polarization as seen in FIGURE 5.3(a). This result has a reasonable explanation. Because modes are easier to concentrate in the dielectric regions with higher refractive index contrast [39], the rectangular sub-lattice presents a stronger waveguiding effect, which traps more light along the waveguiding direction, thus allowing the EFCs to become connected.

The EFCs presented here were obtained using 697 plane waves (17 along one reciprocal lattice vector; 41 along the other). The relative range ($\Delta f/f_c$ or $\Delta\lambda/\lambda_c$) of these “wavy” EFCs is $(0.78-0.66)/0.72=16.7 \%$. The degree of self-collimation ($|\theta_p|_{max}$, as defined in Section 2.4) of these open EFCs is 12° ($|\theta_p|_{max}=12^\circ$). An example is given for $0.66 \mu\text{m}^{-1}$ ($\lambda=1515 \text{ nm}$) in FIGURE 5.3(b). As seen in the figure, light beams incident from different angles are refracted to different directions. Although this result is not what is desired for self-collimation, this design implies a possibility of showing broadband “all-angle” self-collimation if the structure is further optimized.

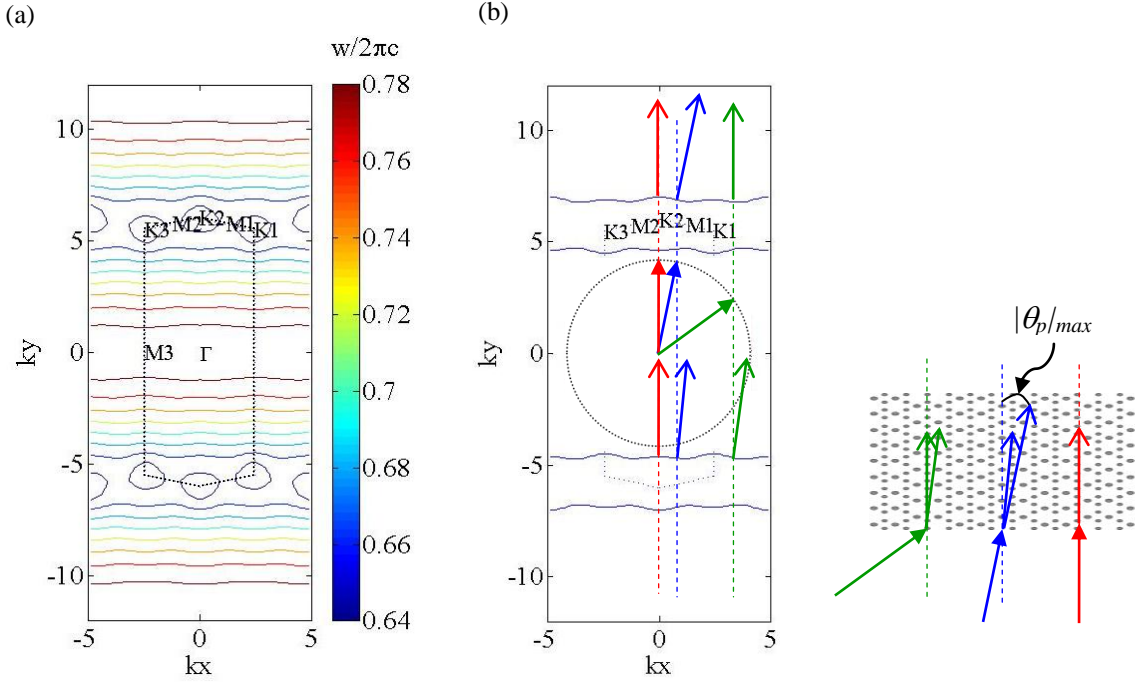


FIGURE 5.3: (a) Fifth band EFCs for TM polarization using Si as the dielectric material. Hexagonal area (dot lines) indicates the first BZ with some special k -points defined as in the figure. (b) Fifth band EFCs at frequency $0.66 \mu\text{m}^{-1}$ ($\lambda=1515 \text{ nm}$). Dashed circle is the corresponding air contour at the same frequency, and the dashed parallel lines are construction lines for surface-parallel wave vector conservation. The arrow style (\rightarrow) indicates wave vectors of lights incident from different angles, while the arrow style (\rightarrow) shows their corresponding refracted wave vectors. The insertion defines the maximum absolute refraction angle ($|\theta_p|_{max}$) among all the refraction angles.

5.4 Broadband virtual “all-angle” self-collimation

In this subsection, the lattice aspect ratio (D_x/D_y) and the ellipticity of the rods are tuned to improve and broaden the self-collimation performance of the Si complex rhombus Talbot crystal. These two variables were chosen in our investigation based on the idea that structures with reduced geometrical symmetry have tendencies towards better self-collimation performance (Section 2.5.2). While tuning the variables mentioned,

the parameters in the y-direction (i.e. D_y , Sb_B , and Sb_S) are assumed constant. Also, all the rods were scaled based on the same scaling ratio. We define a general *longitudinal scaling ratio* to describe how these parameters were tuned. The longitudinal scaling ratio is the ratio of the value of a chosen parameter (for example, lattice aspect ratio or ellipticity of the rods) after stretching/compression to the original value. Longitudinal scaling ratios larger than one imply the structure is stretched; while values less than one indicate compression.

In the previously mentioned Si complex rhombus Talbot crystal, the lattice aspect ratio and the ellipticity of the bigger rods are 4.7139 ($D_x/D_y=2.5738/0.546=4.71$) and 2.83 ($Sa_B/Sb_B =0.17/0.06=2.83$) respectively. To further explore and optimize the structure, the lattice aspect ratio was tuned from 4.71 to 6.6 (based on a longitudinal scaling ratio from 1 to 1.4 with 0.1 increment), and the ellipticity of the bigger rods was tuned from 2.27 to 3.4 (based on a longitudinal scaling ratio from 0.8 to 1.2 with 0.1 increment). The total number of plane waves used varied from 697 (17 along one reciprocal lattice vector; 41 along the other) to 969 (17 along one reciprocal lattice vector; 57 along the other), depending on the dimensions of the unit cell. Within the domain of study, open nearly flat (in short, “nearly flat” assuming $|\theta_p|_{max}=2^\circ$ unless otherwise stated) EFCs are realized in the fifth band for TM polarization when the lattice aspect ratio is equal to or larger than 5.19 (corresponding to $D_x \geq 3.25 \mu\text{m}$ for the desired wavelength range mentioned). In such cases, the complex rhombus lattice structure can be practically applied for “all-angle” self-collimation.

FIGURE 5.4 shows the relative operating range of the virtual ($|\theta_p|_{max}=2^\circ$) “all-angle” self-collimation under different parameter settings. For chosen lattice aspect ratios,

locally a relatively large relative operating range is achieved when the ellipticity of the big rods is 2.55. And for a chosen ellipticity of the rods, the relative operating range is generally larger with a larger lattice aspect ratio. The largest relative operating range within the domain of study is 22.2% when the lattice aspect ratio is 6.6 and ellipticity of the bigger rods is 2.55. This range is comparable to the results from a recently published hybrid square lattice PC proposed by Hamam [2] based on the same criteria ($|\theta_i| < 90^\circ$; $|\theta_p|_{max} = 2^\circ$; $\Delta\lambda/\lambda_c = 22.2\%$). However, our Talbot crystal suffers more diffractive reflection [39] than Hamam's structure, which should be considered with respect to practical applications. We did not continue to increase the lattice aspect ratio for this reason, as will be discussed in Section 5.4.3.

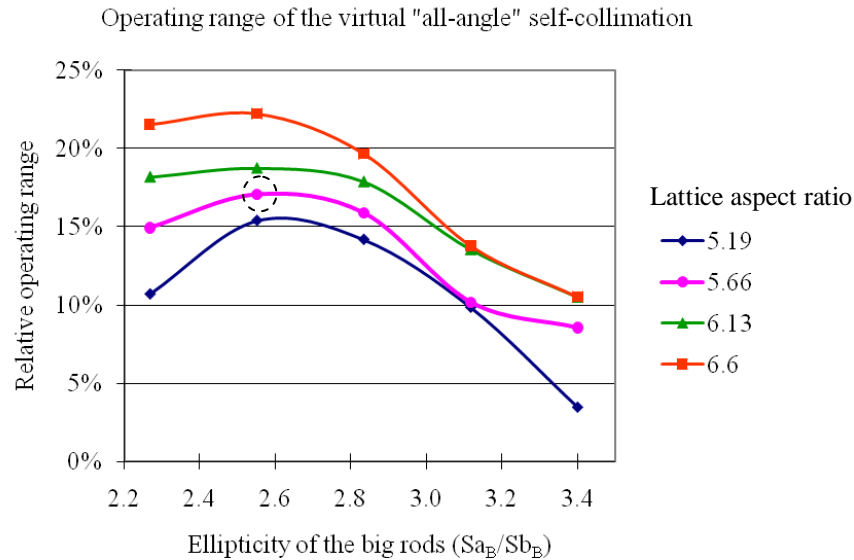


FIGURE 5.4: Relative operating range of the “nearly flat” ($|\theta_p|_{max} = 2^\circ$) EFCs in the fifth band for TM polarization within the domain of study. The dash circle indicates the conditions of a chosen example for EFCs presentation (this section) and transmission studies (Section 5.4.2).

FIGURE 5.5 displays an example of these “nearly flat” EFCs under the following conditions: the lattice aspect ratio is 5.66 and the ellipticity of the bigger rods is 2.55. The

reason for choosing this structure for further study will be explained later in Section 5.4.3. The parameters of the structure are described as follows: $D_x=3.5425 \mu\text{m}$; $D_y=0.6263 \mu\text{m}$; $Sa_B=0.1755 \mu\text{m}$; $Sb_B=0.0688 \mu\text{m}$; $Sa_S=0.1238 \mu\text{m}$; and $Sb_S=0.0574 \mu\text{m}$. These dimensions have been rescaled based on the scaling property of Maxwell's equations [39], allowing the nearly flat EFCs to cover the desired wavelength band centered at 1550 nm. For this structure, the “nearly flat” EFCs are presented from $\omega/2\pi c=0.59 \mu\text{m}^{-1} \sim 0.7 \mu\text{m}^{-1}$ (1429 nm~1695 nm). In other words, this structure supports virtual “all-angle” self-collimation with $\Delta\lambda/\lambda_c=17.05\%$ relative operating range. Within the wavelength range, the refractive index of Si ranges from 3.48 to 3.4644 [113]. Therefore, $n=3.464$ is a good approximation (within $\pm 0.46\%$ percentage difference if material dispersion is considered) throughout the wavelength range mentioned. The operating wavelength range of our complex rhombus lattice Talbot crystal covers wavelengths in the optical communication S-band through the U/XL-band from 1429 nm to 1695 nm (centered at 1550 nm). Also the virtual “all-angle” self-collimation range can be scaled to cover the two most commonly used wavelengths in optical communication at 1310 nm and 1550 nm, if the central wavelength is chosen at 1430 nm.

Structures with such small dimensions and features can be made using nanofabrication techniques (i.e., e-beam lithography with subsequent processing). However, it should be noted that fabrication of such structures is challenging especially if high aspect ratios are required. Further, if the desired operating wavelengths are shorter, the corresponding structure dimensions must also be smaller (according to Maxwell's scaling properties [39]). These are concerns to be aware of if such PC structures are to be realized.

We also explored the EFCs for TE polarization in the same domain of study, but no similar phenomenon was found in this case. From an application point of view, a PC device supporting broadband “all-angle” self-collimation for both polarizations is highly desired. Unfortunately, no PC structure has been reported supporting such properties. This result is related to the mode concentration in the “waveguiding configuration” described in Section 2.6. Recall that broadband “all-angle” self-collimation is likely to be present if the propagating modes are more concentrated in a waveguiding configuration. For rod-type PCs (dielectric rods in an air background), the desired waveguiding configuration is formed by the dielectric rods (for example, the 1D waveguide in Hamam’s hybrid square lattice structure [2], the aligned elliptical scatterers in Liang’s square lattice structure [34], and the rectangular sublattice in the complex rhombus Talbot crystal presented here). In this case, the TM polarized mode is easier to concentrate in the dielectric waveguiding configuration [39] for broadband “all-angle” self-collimation. Similar principles applied to hole-type PCs (air cylinders in dielectric background), where the waveguiding configuration is formed by the aligned air holes (such as the aligned elliptical holes in Liang’s square [34]). Therefore, hole-type PCs more easily support broadband “all-angle” self-collimation with TE polarization.

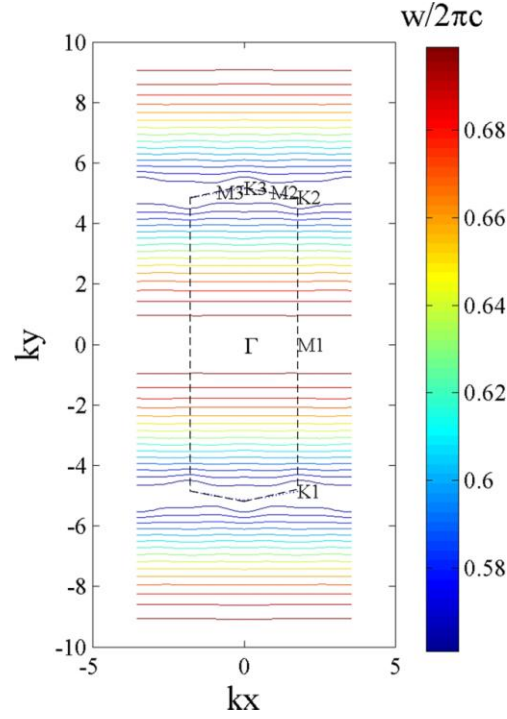


FIGURE 5.5: Fifth band EFCs of the described complex rhombus structure for TM polarization. Eigen-frequencies of the Maxwell's equations are represented by $\omega/2\pi c$ ($=1/\lambda$) with units of μm^{-1} . There are “nearly flat” EFCs from $\omega/2\pi c=0.59 \mu\text{m}^{-1}\sim 0.7 \mu\text{m}^{-1}$ (1429 nm~1695 nm). The dashed hexagon indicates the first BZ and some main k -points.

5.4.1 Robustness of virtual “all-angle” self-collimation to fabrication tolerance

In reality, any structure distortion during fabrication processes could affect the desired optical properties. Here the operating range of the virtual “all-angle” self-collimation is studied in terms of fabrication tolerance. The structure under study is the complex rhombus Talbot crystal supporting broadband virtual “all-angle” self-collimation mentioned earlier (Section 5.4), where the desired dimensions are $D_x=3.5425 \mu\text{m}$; $D_y=0.6263 \mu\text{m}$; $Sa_B=0.1755 \mu\text{m}$; $Sb_B=0.0688 \mu\text{m}$; $Sa_S=0.1238 \mu\text{m}$; and $Sb_S=0.0574 \mu\text{m}$. In this study, the lattice dimensions (i.e. D_x and D_y) are assumed to be the same, but all the elliptical rods are evenly scaled (enlarged or shrunk) from the desired dimensions by a scaling factor (s). The scaling factor can be described by the ratio of the scaled

dimension in each direction to the desired values, i.e. the area of the scaled rod is s^2 times the desired value. Scaling factors larger than one implies the structure is stretched; while values less than one indicate compression. FIGURE 5.6 shows the operating wavelength ranges of the “nearly flat” EFCs with respect to different scaling factors.

The bars in the figure show the wavelength range of the “nearly flat” EFCs ($\Delta\lambda$; left axis) of each distorted structures while the dots represent their corresponding relative ranges ($\Delta\lambda/\lambda_c$; right axis). As seen in the plot, the wavelength range shifts toward longer wavelengths as the elliptical rods are enlarged. This is because the increment of the dielectric material pulls down the frequencies of the modes [39]. This vague notion can be understood qualitatively by referring to the *master equation* (Eq. (3.3)). Mathematically, a larger $\varepsilon(r)$ in Equation (3.3) corresponds to a smaller eigen-frequency ω/c . Therefore, the increment of the dielectric material can generally decrease the value of corresponding eigen-frequencies. According to FIGURE 5.6, if the size of the rods is changed (enlarged or shrunk) by 5%, the wavelengths supporting the “nearly flat” EFCs remain unaffected from 1471 nm to 1613 nm ($\Delta\lambda/\lambda_c=9.2\%$). Therefore, even if the size of the rods is changed (enlarged or shrunk) by 5% during the fabrication process, our complex rhombus Talbot crystal still presents acceptable broadband “all-angle” self-collimation.

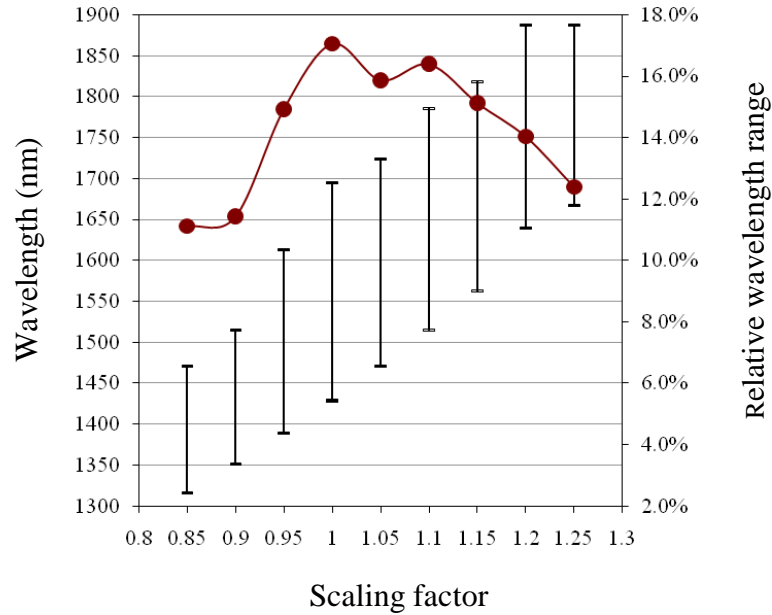


FIGURE 5.6: Wavelength range ($\Delta\lambda$; bars; left axis) and relative range ($\Delta\lambda/\lambda_c$; dots; right axis) of “nearly flat” EFCs based on the best design by rescaling the elliptical rods proportionally. The results can be used to determine fabrication tolerance due to change of the scatterer size.

5.4.2 Study of transmission efficiency

To use self-collimating PCs as optical devices, it is desirable that light can be efficiently coupled into and out of the PC. For potential beam combining and light collection purposes, high transmission efficiency is especially important. Here the transmission spectrum of a limited-sized PC using the proposed Si complex rhombus lattice structure is investigated. The PC discussed is shown in FIGURE 5.7(a). This PC consists of 8.5 longitudinal periods ($8.5D_y=5.32 \mu\text{m}$) in the $\Gamma\text{-K}_3$ direction (y-direction), and 14 transverse periods ($14D_x=49.6 \mu\text{m}$) in the $\Gamma\text{-M}_1$ direction (x-direction), where D_x and D_y have been defined in FIGURE 5.1. The primary collimating direction in the PC is chosen along the $\Gamma\text{-K}_3$ direction. The row with smaller rods along $\Gamma\text{-M}_1$ direction (x-direction) is chosen as the air-PC interface to reduce diffractive reflection. Analysis will

be given in Section 5.4.3. The longitudinal period of this PC was chosen so that relatively high transmission efficiency occurs around 1550 nm (as will be shown later in FIGURE 5.8(a)).

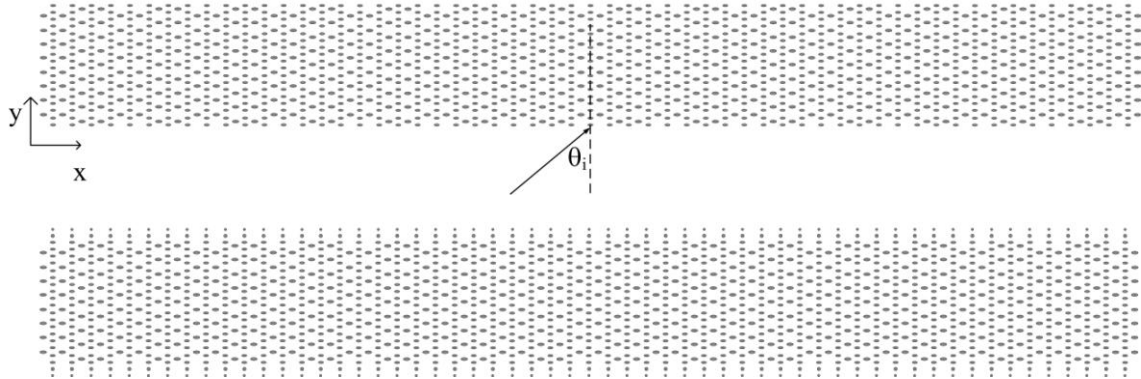


FIGURE 5.7: (a) PC structure for transmission study (b) Modified PC with additional anti-reflection rods. The dimension of the structures is listed as follows: $D_x=3.5425 \mu\text{m}$; $D_y=0.6263 \mu\text{m}$; $Sa_B=0.1755 \mu\text{m}$; $Sb_B=0.0688 \mu\text{m}$; $Sa_S=0.1238 \mu\text{m}$; and $Sb_S=0.0574 \mu\text{m}$, which has been mentioned in Section 5.4. The radii of the anti-reflection rods are $0.0803 \mu\text{m}$ (closer to the interface) and $0.0574 \mu\text{m}$ (farther from the interface)

FDTD with a PML was used to calculate the transmission spectrum using the Rsoft FullWAVETM software package. A Gaussian beam with a width (w_{02} , $w_{02}=2w_0$, where w_0 is the beam waist [114]) of $2.83 \mu\text{m}$ (based on a 20° expansion angle [114] at 1550 nm in air) was launched from air to one side of the structure at assigned incident angles. A monitor of the same width as the illuminated area was placed on the other side of the structure along the collimating direction to capture the transmitted power. FIGURE 5.8(a) shows the normalized transmitted power spectrum of the PC from 1429 nm to 1695 nm at several different incidence angles (0° , 30° , 50° , and 80°). This wavelength range corresponds to the range of the nearly flat EFCs mentioned earlier. Without any modifications to the air-PC interfaces, this structure shows strong Fabry-Perot-like

phenomenon. This result implies a mode mismatch at the air-PC interfaces so that a light mode cannot be coupled into and out of the PC smoothly (i.e. without strong reflection) [115]. As seen in the figure, transmission peaks are shown at specific wavelengths, and these peaks can be adjusted by choosing proper longitudinal length of the PC.

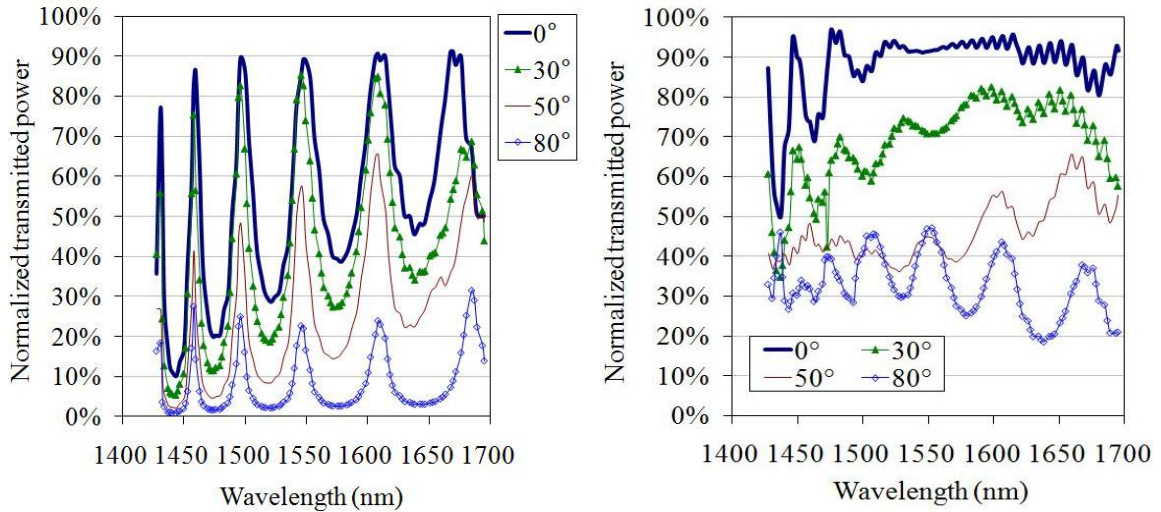


FIGURE 5.8: (a) Transmission spectrum of the power within the illuminated width at the exit side of the PC. The wavelength range shown corresponds to the virtual “all-angle” self-collimation operating range discussed in Section 5.4. (b) Corresponding transmission spectrum of the PC with anti-reflection rods.

In the example shown in FIGURE 5.8(a), locally high transmission efficiency occurs at 1495 nm, 1546 nm, and 1607 nm at 30° of incidence. The transmitted power at these wavelengths reaches 90% of the incident power. As a result, this design has a potential for coarse wavelength division multiplexing (CWDM) to combine wavelengths from optical communication S-band, C-band, and L-band. For example, FIGURE 5.9 shows the beam combining effect generated by the FDTD method. The wavelengths of the two beams are assumed to be 1495 nm ($\theta_i = -30^\circ$) and 1607 nm ($\theta_i = 30^\circ$),

corresponding to the wavelengths presenting locally high transmission efficiency, as mentioned earlier. The specific peak wavelengths can be adjusted by rescaling the lattice structure and/or the longitudinal length of the PC, for example, to cover 1310 nm and 1550 nm. On the other hand, at larger incident angles ($|\theta_i| = 50^\circ$ and $|\theta_i| \leq 80^\circ$ in FIGURE 5.8(a)), the transmission efficiency of the PC drops notably. This could be related to the fact that when $|\theta_i| > 37^\circ$, diffractive reflection occurs in our current design (Section 5.4.3).

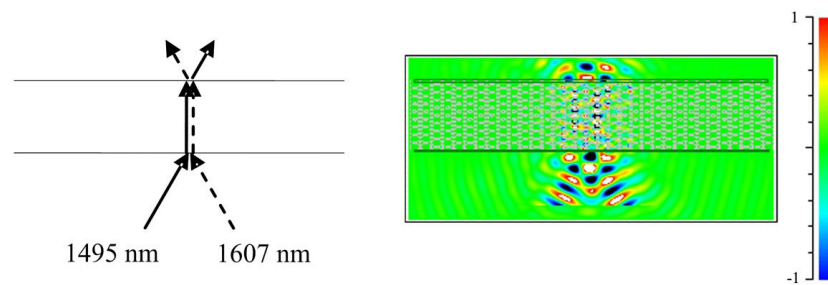


FIGURE 5.9: Beam combining effect using 1495 nm and 1607 nm wavelengths at -30° and 30° respectively.

In order to use this PC for broadband self-collimation purposes, the transmission is desired to be generally high across the frequency range of interest. It has been shown that a rod-type PC can achieve broadband 90% transmission efficiency ($\Delta\lambda/\lambda_c \sim 15\%$ for $|\theta_i| \leq 25^\circ$) without any modification applied to the structure [21]. However, this result is achievable only if multiple diffracted orders do not exist when each layer of the rods is considered as a grating. Our current design does not fulfill this condition. Therefore, additional modification (such as anti-reflection features) is required to improve broadband transmission efficiency.

In this study, additional rod layers are added to both of the air-PC interfaces. Such a design works similarly to anti-reflection layers with a channeled feature to match the

propagating mode [116, 117]. The modified PC with anti-reflection features is shown in FIGURE 5.7(b). Each side of the air-PC interface contains two different sized circular rod-type layers. The distance between these layers, and the distance from the first layer to the interface are both $D_y/2$ (0.3132 μm). The transverse period of both layers is $D_x/4$ (0.0886 μm). The radii of the rod-type layers are 0.0803 μm (closer to the interface) and 0.0574 μm (farther from the interface), and the rod material is also Si.

The resulting transmission spectrum of this modified PC is shown in FIGURE 5.8. This result has a relatively flat transmission spectrum across a broader wavelength range compared with the original PC without anti-reflection features. The transmission efficiency at an incident angle of 80° is also increased. Therefore, the modified PC works better for broadband, wide angle operation. It could be very helpful for WDM with more operating channels and smaller wavelength spacing. However, the transmitted power gradually drops as the incident angle is increased. For incident angles larger than 50° , the transmission efficiency is generally less than 50%. This could be possibly improved by refining the anti-reflection configuration in a future study.

5.4.3 Diffractive reflection

Recall earlier in Section 5.4, we briefly mentioned the practical concern of diffractive reflection when using complex rhombus Talbot crystals as self-collimating devices. More discussion about diffractive reflection will be given in this sub-section.

When a plane wave strikes an interface of a periodic dielectric structure (such as a PC), higher order reflected waves can exist depending upon the frequency, interface periodicity, and band structure. Such higher order reflection is due to the Bragg-diffraction phenomenon, so it is referred to as diffractive reflection [39]. Diffractive

reflection is undesirable since it implies low coupling efficiency and energy losses at the air-PC interface. The latter case might cause interference and cross talk between devices especially in compact optical integrated circuits [21, 118].

Diffractive reflection can be avoided by fulfilling the following condition:

$$\omega a_s / 2\pi c \leq 1 / (1 + \sin \theta_i) \quad (5.1)$$

where a_s is the surface parallel period at the PC interface [39, 62]. Therefore, for all incident angles within 90 degrees ($|\theta_i| < 90^\circ$), $\omega a_s / 2\pi c$ has to be less than 0.5 to ensure no diffractive reflection occurs. In the complex rhombus PC structure (FIGURE 5.1), if the row of bigger rods along the Γ - M_1 direction (x-direction) is chosen as the interface, $a_s = D_x = 3.5425 \mu\text{m}$. For $\lambda = 1429 \text{ nm} \sim 1695 \text{ nm}$, which corresponds to the wavelength range of nearly flat EFCs, $a_s / \lambda = 2.09 \sim 2.479$. Based on the criteria mentioned in Eq. (5.1), diffractive reflection must occur for all incident angles within 90 degrees. However, if the row of smaller rods is chosen as the interface, $a_s = D_x / 4 = 3.5425 / 4 = 0.8856 \mu\text{m}$ and $a_s / \lambda = 0.5225 \sim 0.6198$. Diffractive reflection only occurs if $|\theta_i| > 38^\circ$. We have also performed similar analyses on the complex rhombus Talbot crystals with other lattice aspect ratios, and Hamam's hybrid square lattice structure [2]. The results are listed in TABLE 5.1 for comparison.

The only condition within the domain of study where the structure supports virtual broadband “all-angle” self-collimation with no diffractive reflection for all incident angles ($a_s / \lambda < 0.5$) is when the lattice aspect ratio is 5.19. However, the wavelength range of this desired property is very narrow ($\Delta\lambda / \lambda_c = (1667 - 1624) / 1645.5 = 2.6\%$). On the other hand, as the lattice aspect ratio increases (or a_s increases), the

maximum incident angle allowing no diffractive reflection to occur within the wavelength range decreases. Unfortunately, there is a tradeoff between the operating wavelength range supporting virtual “all-angle” self-collimation ($\Delta\lambda$) and the angular range where no diffractive reflection occurs ($|\theta_i| \leq \theta_{max}$). We chose the lattice aspect ratio of 5.66 and an ellipticity of the bigger rods of 2.55 for the transmission study because these parameters have broad operating wavelength range ($\Delta\lambda/\lambda_c = (1695 - 1429)/1562 = 17.05\%$) with an acceptable angular range ($|\theta_i| \leq 38^\circ$) where no diffractive reflection occurs.

Complex rhombus lattice Talbot crystals	a_s (μm)	$\Delta\lambda$ (μm)	$\Delta\lambda_{NoDiffR}$ (μm)	θ_{max}
Lattice aspect ratio=5.19	0.8118	1429~1667	1624~1667	49°
Lattice aspect ratio=5.66	0.8856	1429~1695	NA	38°
Lattice aspect ratio=6.13	0.9594	1429~1724	NA	29°
Lattice aspect ratio=6.6	1.0333	1429~1786	NA	23°
Hamam’s hybrid square lattice structure [2]	0.786	1429~1786	1572~1786	55°

$\Delta\lambda$: Wavelength range showing virtual “all-angle” self-collimation

$\Delta\lambda_{NoDiffR}$: Wavelength range showing no diffractive reflection for all incident angles within the wavelength range showing virtual “all-angle” self-collimation

θ_{max} : Maximum incident angle allowing no diffractive reflection occurs for all wavelengths within the wavelength range showing virtual “all-angle” self-collimation

NA: Not applicable

TABLE 5.1: Results of diffractive reflection analysis assuming the row with smaller rods is the air-PC interface. Talbot crystals under study have been described in Section 5.4, assuming the ellipticity of the bigger rods is 2.55 and the lattice aspect ratios are listed in the table. A reference result from a hybrid square lattice is also listed for comparison.

We also examined the total reflective power of the complex rhombus Talbot crystals with different lattice aspect ratios (5.66, 6.13, and 6.6) at 30° incident angle. FIGURE 5.10 shows the reflection spectrum of the Talbot crystals from 1429 nm to 1695 nm. This wavelength range corresponds to the range of the “nearly flat” EFCs with a lattice aspect ratio of 5.66. The basic structure of the Talbot crystals for this study is assumed to be the same as described in FIGURE 5.7(a). A monitor with the same width as the PC (i.e. $14D_x$, where $D_x=49.6 \mu\text{m}$, $53.7 \mu\text{m}$, and $57.9 \mu\text{m}$ for lattice aspect ratio=5.66, 6.13, and 6.6, respectively) was placed in front of the structure just behind the source to capture all the power reflected. As seen in FIGURE 5.10, the total reflected power is generally increased as the lattice aspect ratio increases as expected. For a lattice aspect ratio of 5.66, there is no diffractive reflection occurs and the normalized reflection power can be lower than 10%. For lattice aspect ratios of 6.16 and 6.6, since 30° of incident angle is larger than the maximum angular range for no diffractive reflection, diffractive reflection occurs. The total reflected power is noticeable larger with a larger lattice aspect ratio, especially at locally low reflection wavelengths (corresponding to the peak wavelengths, at 1495 nm, 1546 nm, and 1607 nm, in the transmission section shown in FIGURE 5.8(a)). For example, at 1495 nm, the total reflected power for a lattice aspect ratio of 6.6 is more than three times large than for a lattice aspect ratio of 5.66. Assuming we can treat the PC as a homogeneous material with an effective refractive index and apply Fresnel’s equations, a larger lattice aspect ratio corresponding to a smaller refractive index should result in a smaller reflectance at a chosen incident angle. However, this is not the trend shown in FIGURE 5.10. Therefore, this implies that diffractive reflection plays a part in the resulting reflective power.

As reflected power is a practical concern to be taken into account when designing a PC device, we did not further increase the lattice aspect ratio even though it may enable a broader wavelength operating range for broadband virtual “all-angle” self-collimation.

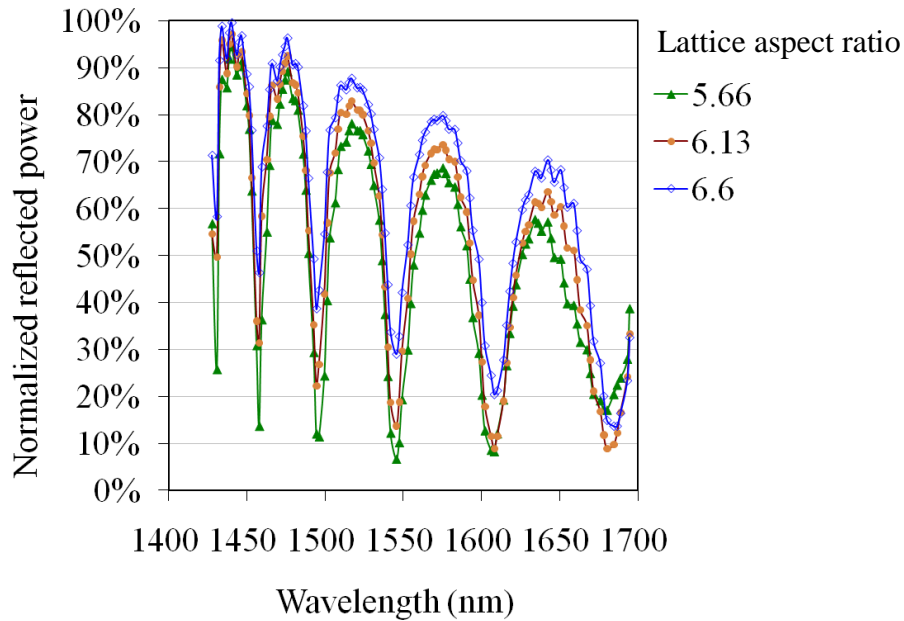


FIGURE 5.10: Normalized reflection spectrum of the total power for PCs with different lattice aspect ratios at 30° incident angle. The power monitor is placed just behind the light source with width of $14D_x$, where $D_x=49.6 \mu\text{m}$, $53.7 \mu\text{m}$, and $57.9 \mu\text{m}$ for lattice aspect ratios of 5.66, 6.13, and 6.6, respectively. The wavelength range shown corresponds to the virtual “all-angle” self-collimation operating range for a lattice aspect ratio of 5.66.

CHAPTER 6: PHOTONIC CRYSTALS FOR THREE-DIMENSIONAL SELF-COLLIMATION

In the previous chapter, we have shown that 2D complex rhombus Talbot crystals are capable of supporting broadband virtual ($|\theta_p|_{max}=2^\circ$) “all-angle” self-collimation for in-plane ($k_z=0$) propagation. In this chapter, additional PC structures are investigated in order to achieve ideal broadband 3D omnidirectional self-collimation. Omnidirectional self-collimation has been introduced in Section 2.4 ($|\theta_i|<\theta=90^\circ$ in FIGURE 2.5(b)). This property enables true 3D self-collimating beams with no limitation on incident angle. Broadband omnidirectional self-collimation provides more flexible usage of current 3D self-collimating devices and may benefit many potential applications, including multiplexers, solar light collection, and PC core fibers (Section 1.1). To realize broadband omnidirectional self-collimation, four PC structures are studied in 3D space, including tetragonal lattice structures, triangular lattice structures, complex hexagonal lattice structures, and kagome lattice structures. Design details and self-collimation performance of each case will be presented and compared in the following sections.

The EFSs and EFCs presented in this chapter were calculated through the PWEM using the MPB software package [87] and the post plotting was done in MATLAB. The spatial resolution is 32 pixels per lattice unit in each direction and the dielectric constant is averaged over 5 mesh points at each grid point. The calculation tolerance (the fractional change of the two sequence eigenvalues) is set to 10^{-7} for convergence.

6.1 3D tetragonal lattice structures

As mentioned in Section 2.5.2 and Section 2.6, structures with lower geometrical symmetry tend to show a wider angular collimating range and/or a broader operating wavelength range. For example, 2D rectangular lattice structures developed from square lattice structures have realized “all-angle” self-collimation [6] and broadband (limited-angled) self-collimation [3]. Here we applied this concept to sc lattice structures (i.e. to develop 3D tetragonal lattice structures) to extend 3D self-collimation performance.

The tetragonal lattice structures studied consist of spherical air holes embedded in dielectric material ($\epsilon=12$, unless otherwise specified). With the orientation indicated (FIGURE 6.1(a)), the lattice constants along the x-, y-, z- directions are defined as a , a , and z , respectively. The radius of the spherical holes equals $0.5z$. Such structures are freestanding and can be fabricated using high precision micromachining [119] or inverse opal methods [109, 110]. The case of $a=z$ corresponds to a sc lattice structure. This sc lattice structure shows cubic-like EFSs in the 3rd band which mimics the shape of its 1st BZ. A similar sc structure with different structure parameters has been reported showing 3D self-collimation [66].

In this study, a is stretched from 1 to 1.2 with 0.05 increments while $z=1$, assuming the desired collimating direction is the z-direction. As a increases, the dielectric regions in this hole-type tetragonal lattice structure gradually form the desired waveguiding configuration (Section 2.6) perpendicular to the stretching direction, suggesting broadband properties. FIGURE 6.1(b) shows the 3rd band EFS of the tetragonal lattice structure with $a=1.05$ at $\omega a/2\pi c=0.3$. The EFS has a tetragonal-like shape, mimicking the shape of its 1st BZ. Similar EFSs are observed across a broad

frequency range. The cross-sections of the 3rd band EFSs are shown in FIGURE 6.1(c)~(f) at different values of k_y . Within 8° of the incident angle ($|\Theta_1| \leq 8^\circ$), the frequency range for flat EFSs with $|\theta_p|_{max} \leq 1^\circ$ is 6.9% of a chosen central frequency ($\omega a/2\pi c = 0.28 \sim 0.3$; $\Delta\omega/\omega_c = (0.3 - 0.28)/0.29 = 6.9\%$); by slightly compromising on the degree of self-collimation with $|\theta_p|_{max} \leq 2^\circ$, this range can be increased to 25.5% ($\omega a/2\pi c = 0.24 \sim 0.31$; $\Delta\omega/\omega_c = (0.31 - 0.24)/0.275 = 25.5\%$). We applied a similar analysis to a previously reported sc lattice structure [66] based on the same criteria ($|\Theta_1| \leq 8^\circ$ and $|\theta_p|_{max} \leq 2^\circ$). The relative frequency range in this case is only 11.8% which is less than half of the range of our 3D tetragonal lattice structure. Applications and usefulness of the presented broadband virtual 3D self-collimation will be discussed in Section 6.5.

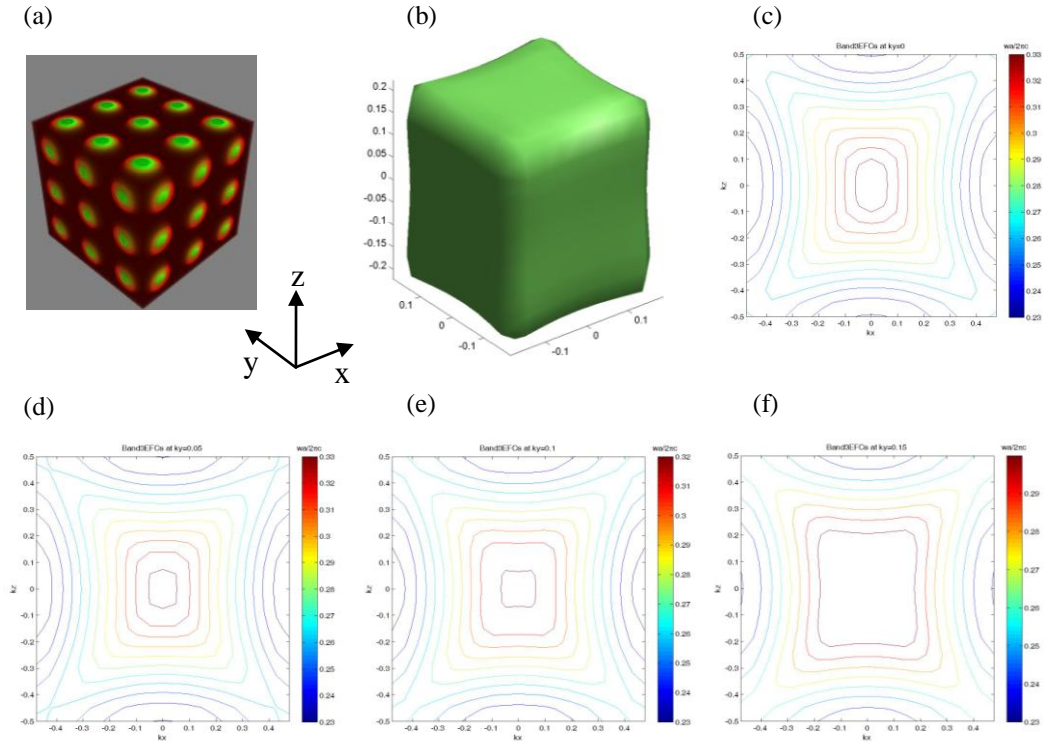


FIGURE 6.1: (a) Hole-type tetragonal lattice structure under study. (b) 3rd band EFS at $\omega a/2\pi c = 0.3$ of the tetragonal lattice structure with $a = 1.05$. (c)~(f) Cross-sections of the 3rd band EFSs at $k_y = 0, 0.05, 0.1, \text{ and } 0.15$, respectively.

Although breaking the geometrical symmetry of a structure can achieve a wider angular collimating range [6], we do not observe such tendencies in the tetragonal lattice structures under study. As a increases, the frequencies showing the flattest EFSs generally decrease, corresponding to a smaller air contour surface. A smaller air contour surface usually helps to produce a larger acceptance angle. However, the flat EFSs of the tetragonal lattice structure also become smaller as a increases. There is a trade-off between these two effects regarding the size of the resultant acceptance angle. The largest resultant acceptance angle of the tetragonal lattice structures (for EFSs with $|\theta_p|_{max} \leq 1^\circ$) found within the domain of study is 17.5° when $a=1.05$ at $\omega a/2\pi c=0.3$, but this property is only present at single frequency in the domain of study. The acceptance angle can be increased by using high refractive index materials (for example, microwave material, HiK500F with $\varepsilon=30$ [82], which results in $|\theta_p| \leq 28.3^\circ$ based on the same criterion). This is due to the fact that, with higher refractive index contrast, light modes are more easily trapped in the dielectric regions, thus resulting in an enhanced self-collimation effect. Therefore, although high refractive index material is not necessary to open a PBG for self-collimation, it can help to improve self-collimation performance due to stronger mode concentration along the waveguiding features. Unfortunately, the acceptance angle of 3D self-collimation in the tetragonal lattice structures (air holes in Si background) is not as comparable to previously reported 3D self-collimating PCs (TABLE 2.1) unless using high refractive index materials (i.e. HiK500F or others with equivalent refractive index) as the background.

6.2 Out-of-plane self-collimation in 2D triangular lattice structures

As mentioned in Section 2.5.3 and Section 2.6, some waveguiding configurations (for example, a 1D waveguide array) can help to realize broadband (in-plane) self-collimation. Recall that in such waveguide arrays, light modes trapped in neighboring dielectric regions have very little overlap at high frequencies [39]. Thus the light modes mostly propagate along the waveguide and present a collimating effect. This result inspired us to consider out-of-plane propagation ($k_z \neq 0$) in 2D PCs for 3D broadband self-collimation. In this case, 2D PCs are treated as 2D waveguide arrays in 3D space (as an example given in FIGURE 6.2(a)), where the propagating direction of light (z-direction) is perpendicular to the plane with periodicity (x-y plane). Such orientation is similar to the orientation of a PC fiber.

The PC under study is a hole-type (air cylinders in a dielectric background) triangular lattice structure (FIGURE 6.2). This structure was chosen because 2D hole-type triangular lattice structures have been shown to be the most promising candidate for absolute (i.e. polarization-independent) PBG (also known as “complete PBG” [39]) in the plane of periodicity (x-y plane) [120]. An in-plane PBG implies EFSs open to the x-y plane. Intuitively, it can help to obtain the desired open flat EFSs needed for 3D omnidirectional self-collimation. Absolute PBGs arise when the radii of the hole-type cylinders are relatively close to half of the lattice constant ($r=0.4a\sim 0.5a$) [39, 120, 121]. Therefore, the radius of the air cylinders was chosen within this range.

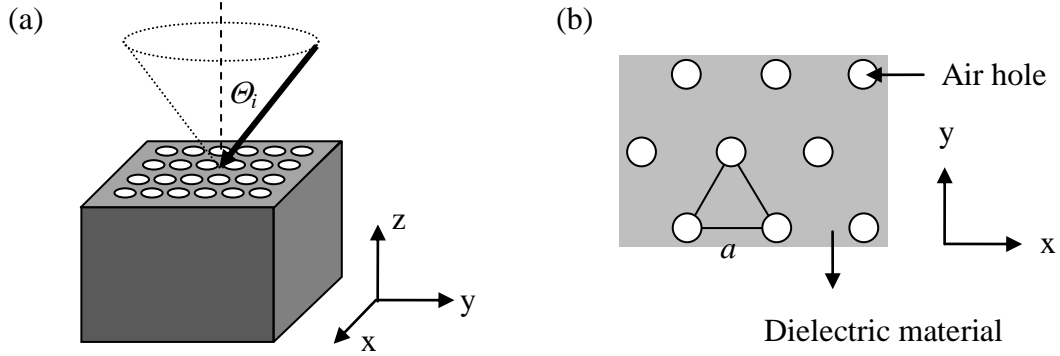


FIGURE 6.2: (a) Orientation for out-of-plane propagation in 2D triangular lattice structures, where the dotted lines, dashed line, and θ_i indicate the incident angle cone, the surface normal, and the incident angle, respectively. (b) Top view of the structure, where a is the lattice constant.

In the first part of this study, Si ($\epsilon=12$) is assumed as the background material and the radius of the air cylinders were chosen to be $r=0.4a$, $0.45a$, and $0.48a$. Within the domain of study, it is found that open flat EFSs with $|\theta_p|_{max} \leq 0.5^\circ$ are achievable, suggesting 3D omnidirectional self-collimation with comparable degree of self-collimation (referred to TABLE 2.1 for degree of self-collimation in previously reported 3D cases). Such omnidirectional (assuming $|\theta_p|_{max} \leq 0.5^\circ$ in the rest of this chapter) self-collimation has not been previously reported in any PC.

For example, FIGURE 6.3(a)~(e) display cross-sections of the EFSs at the five lowest bands of the triangular lattice structure with $r=0.48a$. In the figure, the open flat EFCs at higher frequencies correspond to open flat EFSs (as an example given in FIGURE 6.4(a)), and indicate the presence of omnidirectional self-collimation. Such high-frequency omnidirectional self-collimation is observed when the normalized frequencies are higher than certain minimum values ($\omega a/2\pi c|_{min}$). Normalized and relative frequency ranges of such omnidirectional self-collimation for $|k_z| \leq 5$ are listed in TABLE 6.1. Be aware that the triangular lattice structure under study is homogeneous in

the z -direction (FIGURE 6.2(a)), therefore the light modes in this structure do not have restriction on k_z (i.e. $|k_z|$ can be as large as infinity). For simplicity, we only consider and present results for $|k_z| \leq 5$, but omnidirectional self-collimation may also be present at larger k_z .

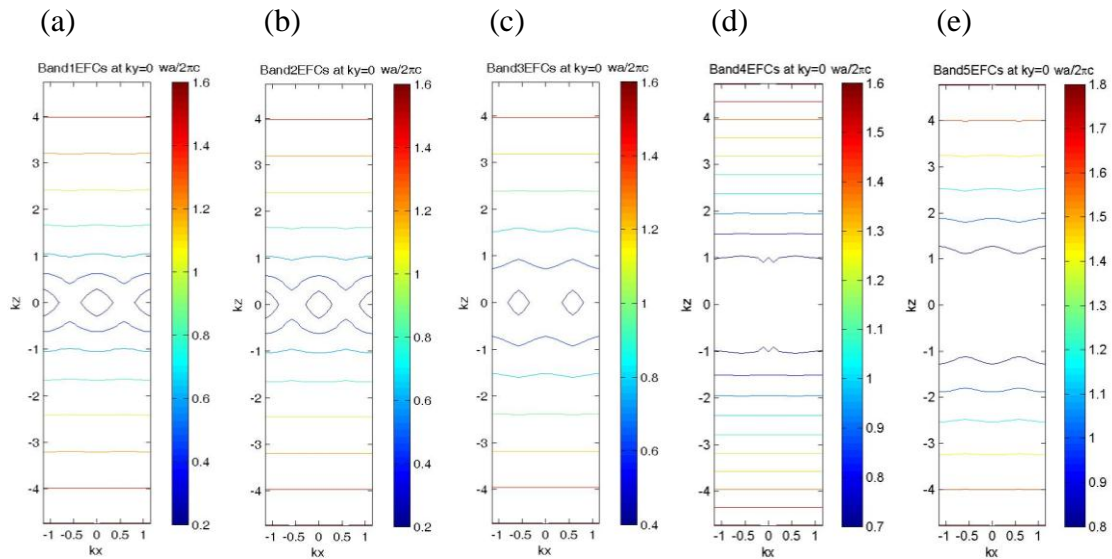


FIGURE 6.3: Cross-sections of the EFSs at $k_y=0$ for (a) 1st (b) 2nd (c) 3rd (d) 4th (e) 5th band of the triangular lattice structure (air cylinders in Si background, $r=0.48a$)

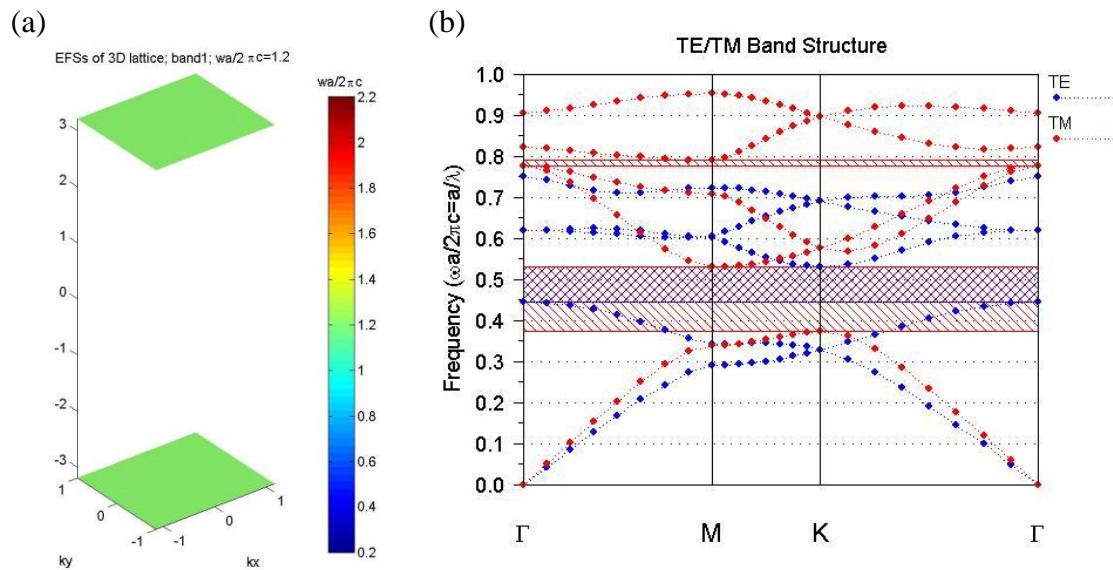


FIGURE 6.4: (a) 1st band EFSs of the triangular lattice structure ($r=0.48a$) at $\omega a/2\pi c=1.2$ (b) Band diagram for in-plane propagation

	1 st band	2 nd band	3 rd band	4 th band	5 th band
$r=0.4a$	1.5~1.51 (0.7 %)	NA	NA	NA	NA
$r=0.45a$	1.25~1.58 (23.3 %)	1.22~1.58 (25.7 %)	1.38~1.58 (13.5 %)	1.36~1.58 (15 %)	NA
$r=0.48a$	1.08~1.66 (42.3 %)	1.01~1.66 (48.7 %)	1.16~1.67 (36 %)	1.14~1.67 (37.7 %)	1.82~1.85 (1.6 %)

TABLE 6.1: Normalized and relative frequency range of omnidirectional self-collimation ($|\theta_p|_{max}=0.5^\circ$) for $|k_z|\leq 5$ in the triangular lattice structures. NA: not applicable

According to TABLE 6.1, structures with larger radius of the air cylinders present broader frequency range for omnidirectional self-collimation. This result can be explained as follows: because the dielectric regions in the hole-type triangular lattice structure become more isolated as the radius of the air cylinders increases, a stronger waveguiding feature is thus formed and increases the frequency range of the self-collimation.

In FIGURE 6.3, there are also open EFSs observed at lower frequencies ($\omega a/2\pi c=0.45\sim 0.53$, corresponding to the in-plane absolute PBG shown in FIGURE 6.4(b)), but these EFSs are not flat to show self-collimation.

In the second part of this study, addition dielectric materials are considered as the background material of the triangular lattice structure with $r=0.48a$. We investigated the EFSs and self-collimation performance assuming the following dielectric constants: $\varepsilon=2.1316$ ($n=1.46$), $\varepsilon=4$ ($n=2$), $\varepsilon=6.26$ ($n=2.5$), $\varepsilon=9$ ($n=3$), and $\varepsilon=31.36$ ($n=5.6$). These values correspond to many commonly used and/or recently popular dielectric materials for PCs and/or antireflection layers, for example, silicon dioxide (SiO_2 , $\varepsilon=2.1\sim 2.16$ for 404.656 nm~1082.97 nm [113]), silicon nitride (Si_3N_4 , $\varepsilon=3.992\sim 4.268$ for 413.3

nm~1240 nm [113]), titanium dioxide (TiO_2 , $\epsilon=7.5\sim 7.84$ ($n_{//}$) and $6.15\sim 6.35$ (n_{\perp}) for 780 nm~1100 nm [113]), TiO_2 ($\epsilon=7.84\sim 11.56$ ($n_{//}$) and $6.35\sim 9$ (n_{\perp}) for 400 nm~780 nm [113]), and beta-iron silicide ($\beta\text{-FeSi}_2$, $\epsilon\sim 31.36$ for 1330 nm~1550 nm [122]).

TABLE 6.2 shows the normalized and relative frequency ranges of the omnidirectional self-collimation for $|k_z|\leq 5$ in each case. As seen in the table, the minimum normalized frequency supporting omnidirectional self-collimation decreases as the refractive index of the background material increases. This is because the larger the refractive index contrast between the two composing materials, the easier it is for light modes to concentrate in the dielectric regions to achieve self-collimation along z-direction. It is preferred to have an optical property presented in relatively low frequencies to reduce (or eliminate) undesired diffraction, including the diffractive reflection discussed in Section 5.4.3. It is found that if $\beta\text{-FeSi}_2$ is used as the background material, there are frequencies supporting omnidirectional self-collimation satisfying the subwavelength condition (i.e. $\omega a/2\pi c=a/\lambda<1$). Therefore, no diffraction occurs as the light beams propagate in such PCs under such conditions. However, since these operating frequencies are larger than 0.5, diffractive reflection (Section 5.4.3) cannot be avoided at the air-PC boundary when a light beam is incident to the PC. As a result, high refractive index materials are not necessary for omnidirectional self-collimation in the triangular lattice structure, but still a preferred option if available.

	1 st band	2 nd band	3 rd band	4 th band	5 th band
SiO₂ ($\epsilon \sim 2.1316$)	3.02~3.83 (23.6 %)	2.95~3.83 (26 %)	3.09~3.83 (21.4 %)	3.1~3.83 (21.1 %)	NA
Si₃N₄ ($\epsilon \sim 4$)	1.98~2.85 (36 %)	1.87~2.85 (41.5 %)	2.09~2.85 (30.8 %)	2.07~2.85 (31.7 %)	NA
TiO₂ ($\epsilon \sim 6.26$)	1.53~2.29 (39.8 %)	1.43~2.29 (46.2 %)	1.66~2.3 (32.3 %)	1.62~2.3 (34.7 %)	NA
TiO₂ ($\epsilon \sim 9$)	1.26~1.92 (41.5 %)	1.17~1.92 (48.5 %)	1.37~1.92 (33.4 %)	1.33~1.92 (36.3 %)	2.12
Si ($\epsilon \sim 12$)	1.08~1.66 (42.3 %)	1.01~1.66 (48.7 %)	1.16~1.67 (36 %)	1.14~1.67 (37.7 %)	1.82~1.85 (1.6 %)
β-FeSi₂ ($\epsilon \sim 31.36$)	0.66~1.03 (43.8 %)	0.62~1.03 (49.7 %)	0.71~1.04 (37.7 %)	0.7~1.04 (39.1 %)	1.08~1.15 (6.3%)

TABLE 6.2: Normalized and relative frequency range of omnidirectional self-collimation for $|k_z| \leq 5$ in the triangular lattice structures ($r=0.48a$) using different background materials. (Data for Si was shown in TABLE 6.1. and is relisted here for comparison.)

6.3 3D complex hexagonal lattice structures

In the previous section, we have shown that triangular lattice structures can realize broadband omnidirectional self-collimation caused by mode concentration in the dielectric regions. Such properties are only present at relatively high normalized frequencies. As briefly mentioned, optical properties at relatively high frequencies may suffer unwanted diffraction. Therefore, we intended to design additional structures to realize broadband omnidirectional self-collimation at relatively lower frequencies.

In this section, a complex hexagonal lattice structure is proposed for the purpose mentioned. The complex hexagonal lattice structure can be described as a 2D hole-type triangular lattice array embedded in alternating dielectric layers (FIGURE 6.5(a)), where the 2D lattice array provides the waveguiding configuration for broadband properties while the periodicity along the z-direction fulfills the conventional requirement for self-

collimation (i.e. the structure must have periodicity along the desired self-collimation direction as mentioned in Section 2.6). The design strategy of this structure is based on a 2D hybrid square lattice structure proposed by Hamam [2] (as introduced in Section 2.5.3), where the periodicity introduced by the square sub-lattice breaks the symmetry of the 1D waveguide array and lowers the frequencies supporting broadband (in-plane) “all-angle” self-collimation. The proposed 3D complex hexagonal lattice structures can be fabricated utilizing current fabrication techniques by stacking alternating dielectric layers using the same techniques used for multi-layer thin films, then make the 2D array using lithography and etching processes. Therefore, it may be less challenging to fabricate this type of structure as compared with other 3D PC structures.

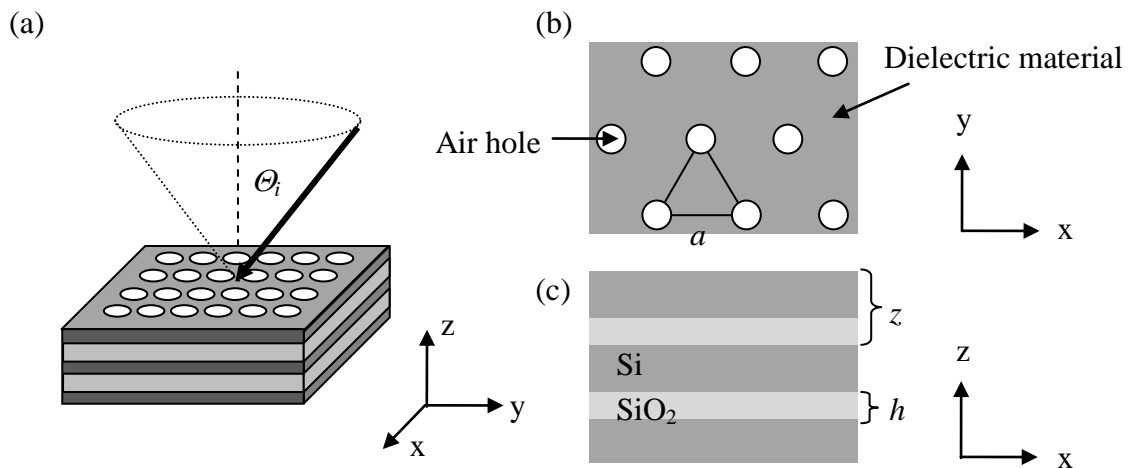


FIGURE 6.5: (a) 3D complex hexagonal lattice structure combining a 2D triangular lattice array with an alternative dielectric stack, where the dotted line, dashed line, and θ_i indicate the incident angle cone, the surface normal, and the incident angle, respectively (b) top view and (c) side view of the structure

FIGURE 6.5 defines the orientation and related structure parameters of this complex hexagonal lattice structure, which is very similar to what was described in the previous section (FIGURE 6.2). The two dielectric materials used in the dielectric stack

are assumed to be Si ($\epsilon=12$) and SiO₂ ($\epsilon=2.1316$), and the thickness of SiO₂ is h . In this study, z is varied from a to $0.1a$ with $0.1a$ decrement, assuming $h=0.1z$ and $r=0.48a$. By compressing the lattice constant z while a remains the same, the resulting 1st BZ areas parallel to the x-y plane become smaller and thus help to realize the desired open flat EFSs for omnidirectional self-collimation along z-direction. This idea is based on a similar concept for in-plane “all-angle” self-collimation summarized in Section 2.6.

It is found that omnidirectional self-collimation is present in this 3D complex hexagonal lattice structure when $z=0.1a$. FIGURE 6.6(a)~(e) display the cross-sections at $k_y=0$ for EFSs at the lowest five bands. Normalized and relative frequency ranges of the omnidirectional self-collimation for $|k_z|\leq 5$ are also listed in TABLE 6.3.

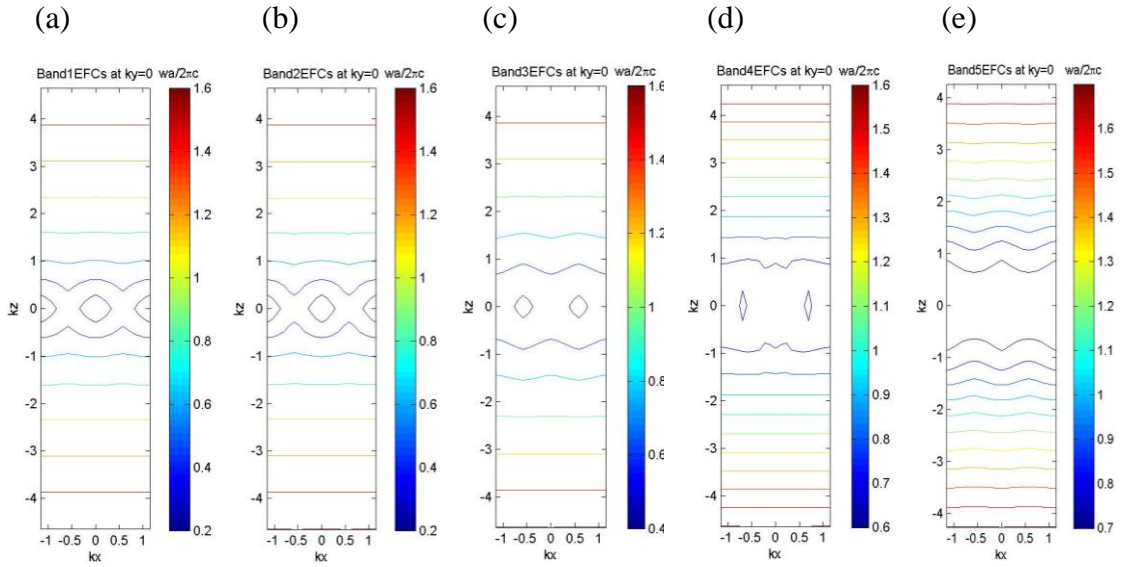


FIGURE 6.6: Cross-sections at $k_y=0$ for (a) 1st (b) 2nd (c) 3rd (d) 4th (e) 5th band EFSs of the 3D complex hexagonal lattice structure (air cylinders embedded in Si ($\epsilon=12$)/SiO₂ ($\epsilon=2.1316$) stack; $z=0.1a$; $h=0.1z$, $r=0.48a$)

	1st band	2nd band	3rd band	4th band	5th band
$r=0.48a$	1.11~1.67 (40.3%)	1.03~1.67 (47.4%)	1.2~1.67 (32.8%)	1.17~1.67 (35.2%)	NA

TABLE 6.3: Normalized and relative frequency range of omnidirectional self-collimation in the 3D complex hexagonal lattice structures (air cylinders embedded in Si ($\epsilon=12$)/ SiO₂ ($\epsilon=2.1316$) stack; $z=0.1a$; $h=0.1z$, $r=0.48a$). NA: not applicable

According to FIGURE 6.6 and TABLE 6.3, the omnidirectional self-collimation presented in this structure also only occurs at relatively high frequencies. And such omnidirectional self-collimation is not shown in the cases where $z \geq 0.2a$. This result suggests that the omnidirectional self-collimation presented in this hexagonal lattice structure is also mainly caused by mode concentration at high frequencies. For larger z (i.e. $z \geq 0.2a$ in this example), because k_z is bounded by the periodicity within a smaller range, no high frequency mode can be included in the structure and thus no such high frequency omnidirectional self-collimation is present. Unfortunately, using alternative dielectric stack as the background material did not flatten the EFSs at lower frequencies as we hoped for.

Compared to the triangular lattice structure discussed in Section 6.2, omnidirectional self-collimation in this 3D complex hexagonal lattice structure has slightly narrower operating range for all bands. Therefore, the triangular lattice structure presented in Section 6.2 is a better option for omnidirectional self-collimation due to its broader operating range and simpler structure design.

6.4 Out-of-plane self-collimation in 2D kagome lattice PCs

Another structure we considered for 3D self-collimation is a rod-type kagome lattice structure (FIGURE 6.7(a) [123]). The kagome lattice structure under study was originally proposed by Takeda to show flat photonic bands for in-plane propagation (FIGURE 6.7(b) [123]), but such a structure has not been considered for 3D self-collimation. The idea of using flat band PCs for 3D self-collimation can be explained by interpreting the quasi-flat bands (around $\omega a/2\pi c=0.22$ and $\omega a/2\pi c=0.46$) shown in FIGURE 6.7(b). For a given k_z ($k_z=0$ in this example), light modes of a flat band excited by all possible $k_{//}$ (k_x and k_y components) have very close angular frequencies, resulting in nearly flat EFSs parallel to the x-y plane in 3D k -space required for 3D self-collimation.

The kagome lattice structure under study is made by high refractive index rods (Indium antimonide (InSb), $\epsilon=17.7$) embedded in an air background. The radius of the rods is $r=0.2a$, where a in this particular case is the distance between the nearest-neighbor rods. FIGURE 6.7(c) indicates the orientation of this structure for 3D self-collimation. We note that there are practical limitations to fabricate this design with large height in the z direction due to the aspect ratio of the InSb structures; this issue is discussed in more detail later.

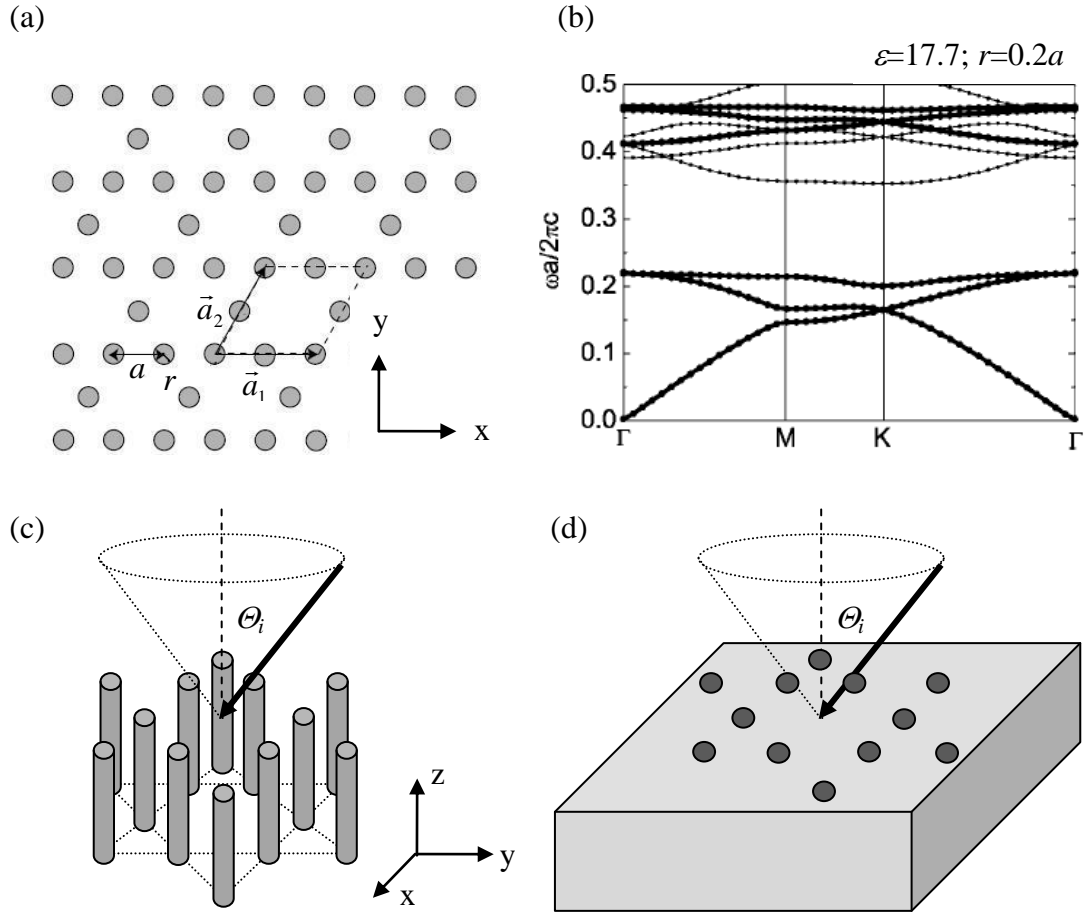


FIGURE 6.7: (a) The 2D rod-type kagome lattice PC structure [123] under study. The shaded circle indicates the dielectric rods, where r is the radius of the rod, a is the distance between the nearest-neighboring rods, a_1 and a_2 are the primitive lattice vectors of this structure. (b) The band diagram of this kagome structure [123] (c) The orientation for 3D self-collimation. (d) The “embedded design”

FIGURE 6.8(a)~(e) shows the cross-sections at $k_y=0$ for EFSs of this kagome lattice structure at the lowest five bands. This structure shows omnidirectional self-collimation at higher frequencies, similar to what was presented in Section 6.2 and Section 6.3. Such high frequency omnidirectional self-collimation is a general out-of-plane property of 2D PCs. Normalized and relative frequency ranges of the omnidirectional self-collimation for $|k_z| \leq 5$ in each band are listed in TABLE 6.4.

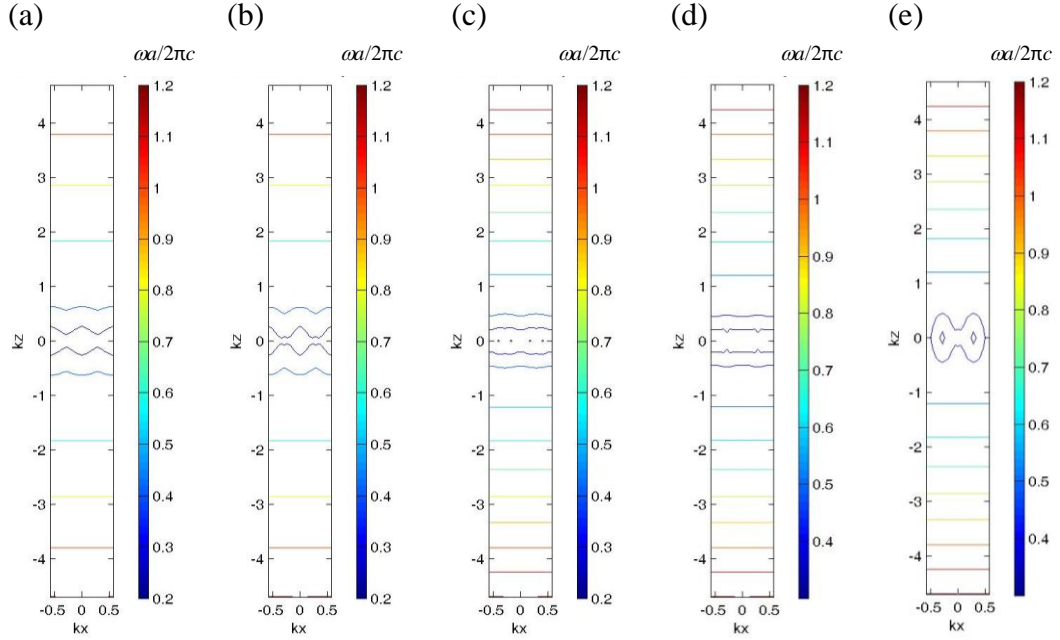


FIGURE 6.8: Cross-sections at $k_y=0$ for (a) 1st band (b) 2nd band (c) 3rd band (d) 4th band (e) 5th band EFSs of the kagome lattice structure (InSb ($\epsilon=17.7$) rods ($r=0.2a$) embedded in an air background)

	1 st band	2 nd band	3 rd band	4 th band	5 th band
$r=0.2a$	0.52~1.26 (83.1 %)	0.49~1.26 (88 %)	0.51~1.26 (84.7 %)	0.51~1.26 (84.7 %)	0.51~1.26 (84.7 %)

TABLE 6.4: Normalized and relative frequency range of omnidirectional self-collimation for $|k_z| \leq 5$ in the kagome lattice structures (InSb ($\epsilon=17.7$) rods ($r=0.2a$) embedded in an air background).

Compared with the hole-type β -FeSi₂ triangular lattice structure discussed in Section 6.2 (TABLE 6.2), the minimum frequencies supporting omnidirectional self-collimation are much lower in this kagome lattice structure. This is because rod-type lattice structures generally provide a more isolated waveguiding configuration than hole-type structures, and thus present stronger mode concentration at lower frequencies.

It is interesting to notice that, in addition to the omnidirectional self-collimation at high frequencies, this kagome lattice structure also presents open visually flat EFSs at relatively lower frequencies (4th band around $\omega a/2\pi c=0.3\sim 0.4$, FIGURE 6.9). This behavior at low frequencies has not been seen in the other PC structures discussed so far in this dissertation. The flattest EFS found within this range is at $\omega a/2\pi c=0.38$ (FIGURE 6.10(a)), which presents omnidirectional beam confinement with $|\theta_{p/max}|\leq 7^\circ$. This property cannot be realized by isotropic materials. Similar omnidirectional beam confinement is also present at $\omega a/2\pi c=0.25$, with a better beam confinement ($|\theta_{p/max}|\leq 5^\circ$, FIGURE 6.10(b)). Although the flat EFSs in this case are not open across the whole 1st BZ, the flat EFS area is larger than the diameter of the corresponding air contour surface so that omnidirectional beam confinement occurs.

We also applied similar analysis as discussed in Section 0, assuming the incident angle is within 8° ($|\theta_i|\leq 8^\circ$) and the tolerable degree of self-collimation is $|\theta_{p/max}|\leq 2^\circ$, the relative frequency range of the virtual 3D self-collimation at low frequencies ($\omega a/2\pi c\leq 0.4$) of the kagome lattice structure can be more than 60% ($\omega a/2\pi c=0.22\sim 0.41$; $\Delta\omega/\omega_c=(0.41-0.22)/0.315=60.3\%$). This range is more than two times the range shown in the 3D tetragonal lattice structure (25.5%, Section 0) based on the same criteria.

It is desirable to realize omnidirectional self-collimation ($|\theta_{p/max}|\leq 0.5^\circ$) at low frequencies not only to avoid unwanted diffraction but also because it is the key to accomplishing ideal whole-band (no restriction on operating frequency) omnidirectional self-collimation. Unfortunately, omnidirectional self-collimation ($|\theta_{p/max}|\leq 0.5^\circ$) has not been realized at relatively low frequencies, but the self-collimation performance at lower frequencies presented here ($|\theta_i|\leq 8^\circ$, $|\theta_{p/max}|\leq 2^\circ$, $\Delta\omega/\omega_c=60.3\%$) has already shown a

broader wavelength operating range (based on the same criteria mentioned) compared with previously reported 3D self-collimating PCs (TABLE 2.1).

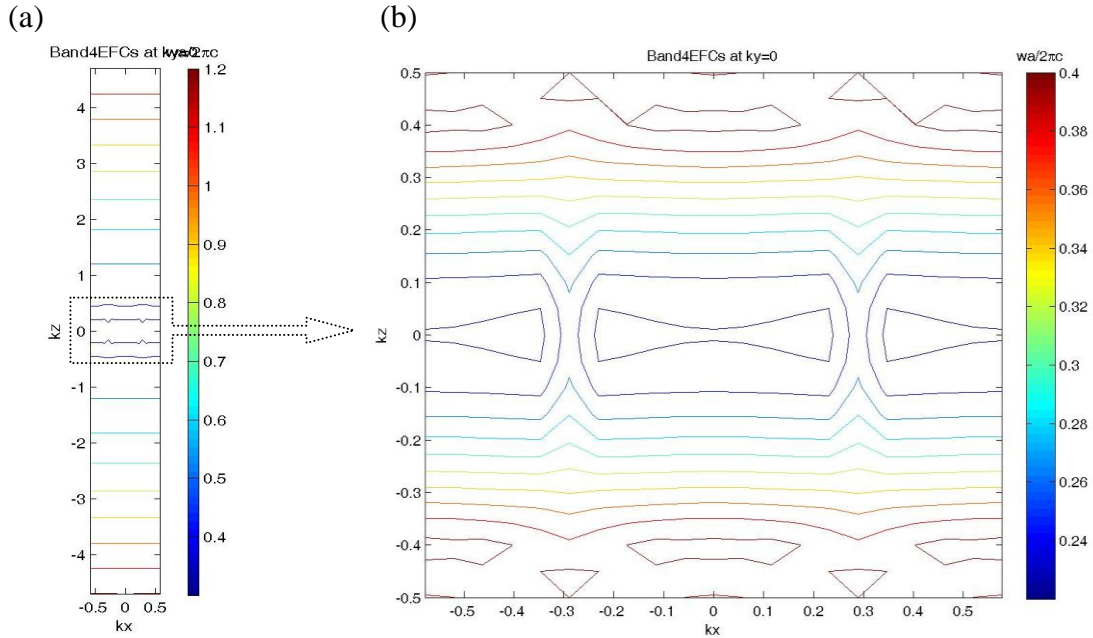


FIGURE 6.9: (a) Cross-section of the 4th band EFSs at $k_y=0$ (b) close view for $\omega a/2\pi c=0.22\sim 0.4$.

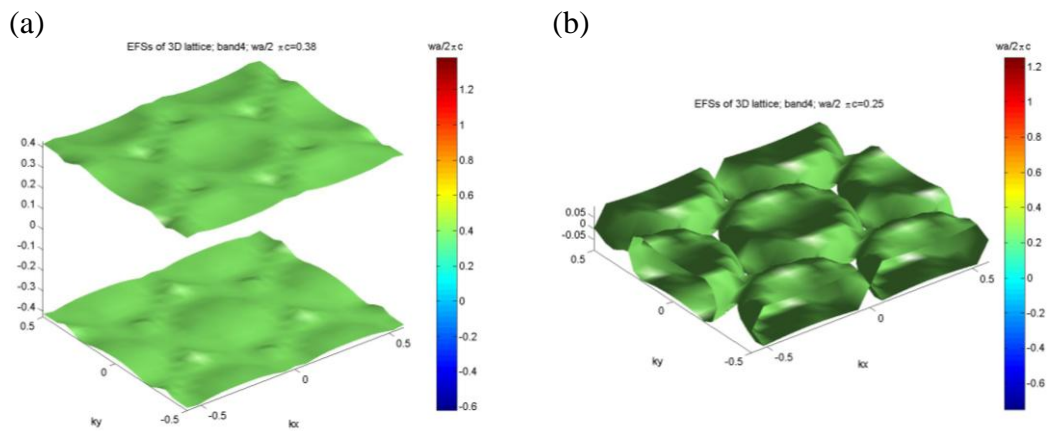


FIGURE 6.10: 4th band EFSs of the kagome lattice structure at (a) $\omega a/2\pi c=0.38$ (b) $\omega a/2\pi c=0.25$. Due to a smaller air contour sphere at $\omega a/2\pi c=0.25$, a smaller area of flat EFSs is required to present omnidirectional beam confinement.

Although the kagome lattice structure has shown omnidirectional self-collimation at the lowest frequency range among the structures presented so far, this structure is not practical due to the aspect ratio of the InSb rods. In reality, an alternative solution is using a high refractive index material embedded in a low refractive index material (the “embedded design,” FIGURE 6.7(d)). We considered a kagome lattice structure using β -FeSi₂ ($\epsilon=31.36$) embedded in SiO₂ ($\epsilon=2.1316$) and assume other structure parameters remain the same. β -FeSi₂ is chosen, because its refractive index is higher than InSb. It can retain relatively high refractive index contrast with the SiO₂ background ($31.36/2.1316=14.7$) and might also reduce the minimum frequency showing omnidirectional self-collimation. This modified kagome lattice structure is all-solid and could potentially be fabricated by adopting fabrication techniques for semiconductors (such as Si and Germanium (Ge)) optical fibers [33, 124-127], including stack and draw techniques [128] and chemical deposition techniques [124, 126].

FIGURE 6.11(a)~(e) shows the cross-sections of the EFSs at $k_y=0$ of the modified kagome lattice structure at the lowest five bands, and TABLE 6.5 lists the normalized and relative frequency ranges of the omnidirectional self-collimation for $|k_z|\leq 5$ are. As shown in FIGURE 6.11 and TABLE 6.5, omnidirectional self-collimation can be realized in this design and is present at a lower minimum normalized frequency compared to the original design (InSb in air), which is better than our original expectation. There are also open visually flat EFSs at lower frequencies in the 4th band (FIGURE 6.11(d) and close view in FIGURE 6.12). Omnidirectional beam confinement is present at $\omega a/2\pi c=0.2$ with $|\theta_p|_{max}\leq 7^\circ$, which is comparable to the result in the InSb kagome lattice structure. In addition, broadband 3D self-collimation (assuming $|\theta_p|_{max}\leq 2^\circ$) is present in the range of

$\omega a/2\pi c=0.17\sim 0.25$ ($\Delta\omega/\omega_c=(0.25-0.17)/0.21=38\%$) with a slightly larger acceptance angle ($|\Theta_i|\leq 11^\circ$). Although the embedded design loses about half of the relative frequency range for virtual limited-angled self-collimation at lower frequencies, the presented frequency range is close to 1.5 times broader than the corresponding range shown in the 3D tetragonal lattice structure (25.5%, Section 6.1) based on the same criteria.

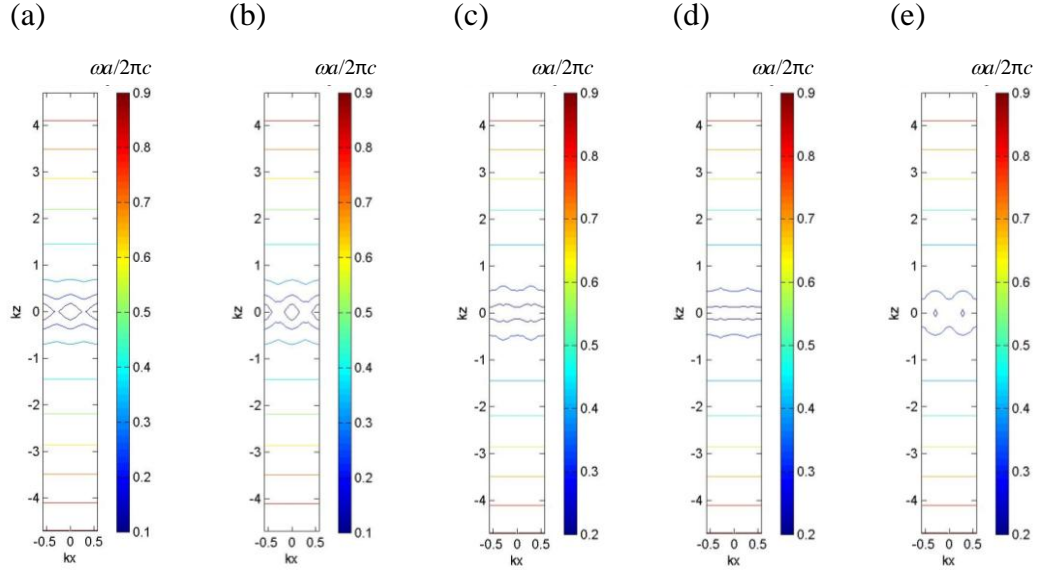


FIGURE 6.11: Cross-sections of the EFSs at $k_y=0$ for (a) 1st band (b) 2nd band (c) 3rd band (d) 4th band (e) 5th band of the embedded kagome lattice structures (β -FeSi₂ ($\varepsilon=31.36$) rods ($r=0.2a$) embedded in SiO₂ ($\varepsilon=2.1316$) background).

	1 st band	2 nd band	3 rd band	4 th band	5 th band
$r=0.2a$	0.4~0.95 (81.5 %)	0.37~0.95 (87.9 %)	0.38~0.95 (85.7 %)	0.39~0.95 (83.6 %)	0.38~0.95 (85.7 %)

TABLE 6.5: Normalized and relative frequency range of omnidirectional self-collimation for $|k_z|\leq 5$ in the embedded kagome lattice structures (β -FeSi₂ ($\varepsilon=31.36$) rods ($r=0.2a$) embedded in SiO₂ ($\varepsilon=2.1316$) background).

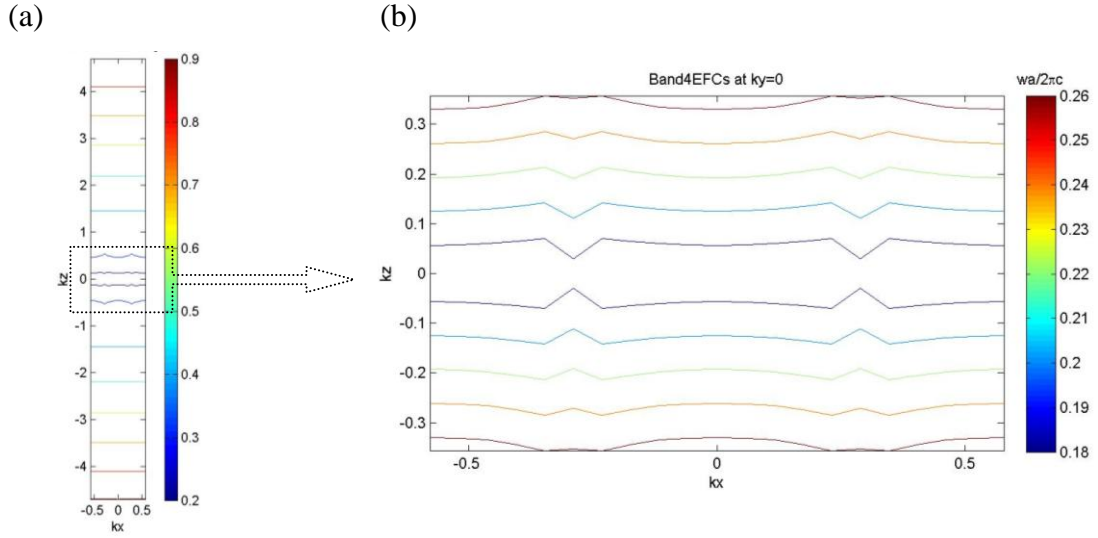


FIGURE 6.12: (a) Cross-section of the 4th band EFSs at $k_y=0$ of the embedded kagome lattice structure (β -FeSi₂ ($\epsilon=31.36$) rods ($r=0.2a$) embedded in SiO₂ ($\epsilon=2.1316$) background) (b) close view for $\omega a/2\pi c=0.18\sim 0.26$.

6.5 Summary and discussion

In this chapter, multiple PC structures have been studied for 3D self-collimation performance. All previously reported 3D self-collimation has only been shown at a particular operating frequency, and with limitations on incident angle (TABLE 2.1). As broadband 3D omnidirectional self-collimation has not been reported in any PC structure, our proposed PC structures have shown desired properties towards this ideal.

It is found that 3D tetragonal lattice structures (air spheres in Si background, Section 6.1) can display broadband ($\omega a/2\pi c=0.24\sim 0.31$; $\Delta\omega/\omega_c=25.5\%$) virtual self-collimation ($|\theta_p|_{max}\leq 2^\circ$) within the lowest 8° of incident angles ($|\theta_i|\leq 8^\circ$). In addition, 2D kagome lattice structures (β -FeSi₂ rods in SiO₂ background, Section 6.4) can also present similar out-of-plane broadband virtual self-collimation at $\omega a/2\pi c=0.17\sim 0.25$, with a larger operating frequency range ($\Delta\omega/\omega_c=38\%$) and acceptance angle ($|\theta_i|\leq 11^\circ$). The operating range in the latter case, for example, covers optical communication bands from

1260 nm to 1675 nm for any central wavelength chosen between 1408 nm and 1555 nm. Such properties provide flexibility for applications needing a loose degree of self-collimation that do not require a large angular collimating range, such as beam combiners.

On the other hand, the desired broadband 3D omnidirectional self-collimation ($|\theta_p|_{max} \leq 0.5^\circ$) can be realized using out-of-plane propagation in 2D triangular lattice structures (Section 6.2) and kagome lattice structures (Section 6.4), as well as proposed 3D complex hexagonal lattice structures (Section 6.3). The 3D complex hexagonal lattice structures exhibit the desired properties at $\omega a/2\pi c = 1.03 \sim 1.67$; with a relative operating frequency range ($\Delta\omega/\omega_c = 47.4\%$) even larger than ones in the previously mentioned broadband limited-angled 3D self-collimation. However, the 3D complex hexagonal lattice structure is not the structure found showing the broadest operating frequency range for omnidirectional self-collimation. Out-of-plane omnidirectional self-collimation in 2D triangular lattice and kagome lattice structures is present as the frequency reaches minimum values of $\omega a/2\pi c|_{min} = 0.62$ and 0.49 respectively. Therefore, the reported properties show the potential for self-collimation to be applied to applications, such as multiplexers, solar light collection and PC core fibers.

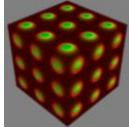
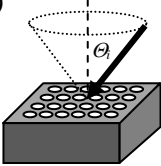
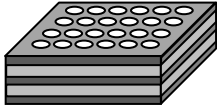
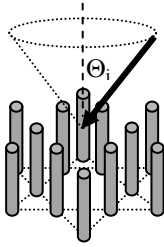
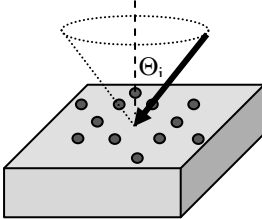
PC structures	Example self-collimation performance	Notes
3D tetragonal lattice structures (Section 6.1)	$ \Theta_i \leq 8^\circ$ for $ \theta_p _{max} \leq 2^\circ$ $\Delta\omega/\omega_c = 25.5\%$ ($\omega a/2\pi c = 0.24 \sim 0.31$)	
Out-of-plane propagation in 2D triangular lattice structures (Section 6.2) 	Omnidirectional self-collimation with $ \theta_p _{max} \leq 0.5^\circ$; $\omega a/2\pi c _{min} = 1.01$	Air cylinders in Si background ($r = 0.48a$)
	Omnidirectional self-collimation with $ \theta_p _{max} \leq 0.5^\circ$; $\omega a/2\pi c _{min} = 0.62$	Air cylinders in β -FeSi ₂ background ($r = 0.48a$)
3D complex hexagonal lattice structures (Section 6.3)	Omnidirectional self-collimation with $ \theta_p _{max} \leq 0.5^\circ$; $\Delta\omega/\omega_c = 47.4\%$ ($\omega a/2\pi c = 1.03 \sim 1.67$)	
Out-of-plane propagation in 2D kagome lattice structures (Section 6.4)	<ul style="list-style-type: none"> ◆ $\Theta_i \leq 8^\circ$ for $\theta_p _{max} \leq 2^\circ$ $\Delta\omega/\omega_c = 60.3\%$ ($\omega a/2\pi c = 0.22 \sim 0.41$) ◆ Omnidirectional beam confinement with $\theta_p _{max} \leq 7^\circ$ ($\omega a/2\pi c = 0.38$) ◆ Omnidirectional beam confinement with $\theta_p _{max} \leq 5^\circ$ ($\omega a/2\pi c = 0.25$) ◆ Omnidirectional self-collimation with $\theta_p _{max} \leq 0.5^\circ$ ($\omega a/2\pi c _{min} = 0.49$) 	Takeda's design (InSb rods in air background) [123] 
	<ul style="list-style-type: none"> ◆ $\Theta_i \leq 11^\circ$ for $\theta_p _{max} \leq 2^\circ$ $\Delta\omega/\omega_c = 38\%$ ($\omega a/2\pi c = 0.17 \sim 0.25$) ◆ Omnidirectional beam confinement with $\theta_p _{max} \leq 7^\circ$ ($\omega a/2\pi c = 0.2$) ◆ Omnidirectional self-collimation with $\theta_p _{max} \leq 0.5^\circ$ ($\omega a/2\pi c _{min} = 0.37$) 	Embedded design (β -FeSi ₂ rods in SiO ₂ background) 

TABLE 6.6: Summary of PCs for 3D self-collimation and their performance.

CHAPTER 7: CONCLUSIONS

In this dissertation, several PC structures were proposed to improve and extend self-collimation performance. These structures include different features to combine multiple self-collimation properties in a single design. It is found that broadband virtual (i.e. $|\theta_p|_{max} \leq 2^\circ$) (in-plane) “all-angle” self-collimation and several new 3D self-collimation properties can be realized by different proposed PC structures. These results are summarized and discussed in this chapter.

Virtual “all-angle” self-collimation is present in the 2D complex rhombus lattice Talbot crystals at 5th band for TM polarization with $\Delta\omega/\omega_c=17.05\%$ (CHAPTER 5). This range is comparable to two previously reported PC structures, including a 2D hybrid square lattice structure proposed by Hamam ($\Delta\omega/\omega_c=22.2\%$) [2] and a 2D square lattice structure ($\Delta\omega/\omega_c=10.9\%$) proposed by Liang [34]. Therefore, the proposed Talbot crystal can serve as an alternative option for broadband “all-angle” self-collimation with slightly compromised degree of self-collimation. Applications that do not require long-distance propagation can benefit from such a broad operating wavelength range for self-collimation, such as collimating beam combiners and multiplexers. If a central wavelength is chosen at 1550 nm, the presented virtual “all-angle” self-collimation covers the optical communication S-band through the U/XL-band from 1429 nm to 1695 nm. Although a larger operating frequency range is achievable by stretching the structure along a rhombus diagonal direction, the trade-off is higher reflected power at the air-PC interface (i.e. lower coupling efficiency). The robustness of such virtual “all-angle” self-collimation was also evaluated. If the size of the rods is changed (enlarged or shrunk) by 5%, the relative operating range is reduced to $\Delta\omega/\omega_c=9.2\%$ but this range is still

comparable to the one in Liang's 2D square lattice structure. Transmission spectra for two complex rhombus lattice PC configurations (with and without anti-reflection rods) were also presented and discussed. However, the transmission efficiency for large angles of incidence is currently a limitation that could be improved in future studies.

To date, broadband "all-angle" self-collimation in a PC structure has been reported for only a single polarization state per structure (TM polarization with rod-type PC structures as in our work and Ref. [2, 34]; TE polarization with hole-type PC structures as in Ref. [34]). A possible solution for polarization-independent broadband "all-angle" self-collimating PC is to combine features supporting the individual properties. This would be an interesting topic for exploration in future work.

In addition to broadband virtual "all-angle" self-collimation, several desired 3D self-collimation properties are realized for the first time, including broadband virtual 3D limited-angled self-collimation, 3D omnidirectional beam confinement, and broadband 3D omnidirectional self-collimation (CHAPTER 6). As the presented properties have not been previously reported in any PC structure, the proposed PC structures can provide 3D collimated beams for current self-collimation applications with more flexible usages, and extend the usefulness of self-collimation to additional applications, including solar light collection and PC core fibers.

Broadband 3D omnidirectional self-collimation ($|\theta_p|_{max} \leq 0.5^\circ$) can be realized by 3D complex hexagonal lattice structures and out-of-plane propagation in 2D triangular and kagome lattice structures. The presented omnidirectional self-collimation is only displayed at relatively high frequencies. In the case of 3D hexagonal lattice structures, there is an operating frequency range ($\omega a/2\pi c = 1.03 \sim 1.67$, $\Delta\omega/\omega_c = 47.4\%$) for such

properties due to its periodicity in the propagation direction. But for the triangular and kagome lattice structures, omnidirectional self-collimation is shown as the frequency reaches some minimum values. For example, $\omega a/2\pi c|_{\min}=1.01, 0.62, 0.49,$ and 0.37 respectively in a Si hole-type triangular lattice structure ($r=0.48a$), the β -FeSi₂ hole-type triangular lattice structure, the InSb rod-type kagome lattice structure, and the embedded (β -FeSi₂ in SiO₂) kagome lattice structures. Generally, using rod type designs (isolated high refractive index material embedded in low refractive index material) and higher refractive index materials can reduce the minimum frequency, which helps to avoid unwanted diffraction (for example, diffractive reflection that may increase total reflected power and reduces coupling efficiency).

In addition, broadband virtual 3D limited-angled self-collimation and omnidirectional beam confinement are presented at relatively lower frequencies in the kagome lattice structures. In the embedded (β -FeSi₂ in SiO₂) kagome structure, the virtual ($|\theta_p|_{\max}\leq 2^\circ$) self-collimation is presented at $\omega a/2\pi c=0.17\sim 0.25$ ($\Delta\omega/\omega_c=38\%$) within $|\theta_i|\leq 11^\circ$. This range is more than 1.5 times larger than the one realized in 3D tetragonal lattice structures ($\omega a/2\pi c=0.24\sim 0.31$; $\Delta\omega/\omega_c=25.5\%$) based on the same criteria. On the other hand, omnidirectional beam confinement is realized at $\omega a/2\pi c=0.2$ with $|\theta_p|_{\max}\leq 7^\circ$. Although omnidirectional self-collimation was not found at relatively lower frequencies, these two low-frequency properties can be the key to approaching whole-band 3D omnidirectional self-collimation in the future. In this work, such low-frequency phenomena are only seen in the kagome lattice structures. Further study is necessary to determine if these low-frequency properties are related to the flat band properties of the kagome lattice structures.

For comparison, TABLE 7.1 summarizes all achieved self-collimation performance in this work with previously reported results (if applicable). To apply the proposed properties to actual applications, additional study is required for further optimization and to address practical concerns, including effects caused by the limited size of the PCs and fabrication issues.

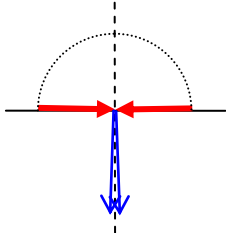
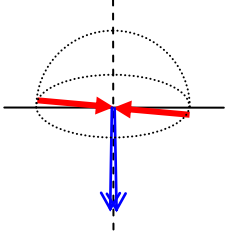
Self-collimation type	PC structures	Performance details
Broadband (in-plane) virtual “all-angle” self-collimation ($ \theta_{p/max} \leq 2^\circ$) 	2D complex rhombus lattice Talbot crystals (★)	$\Delta\omega/\omega_c=17.05\%$
	2D hybrid square lattice structures [2]	$\Delta\omega/\omega_c=22.2\%$
	2D square lattice structures [34]	$\Delta\omega/\omega_c=10.9\%$
Broadband 3D omnidirectional self-collimation ($ \theta_{p/max} \leq 0.5^\circ$) (★) 	Out-of-plane propagation in 2D triangular lattice structures (air cylinders in Si background, $r=0.48a$)	$\Delta\omega/\omega_c \geq 48.7\%$ ($\omega a/2\pi c _{min}=1.01$)
	Out-of-plane propagation in 2D triangular lattice structures (air cylinders in β -FeSi ₂ background, $r=0.48a$)	$\Delta\omega/\omega_c \geq 49.7\%$ ($\omega a/2\pi c _{min}=0.62$)
	Out-of-plane propagation in 2D kagome lattice structures (InSb rods in air background)	$\Delta\omega/\omega_c \geq 88\%$ ($\omega a/2\pi c _{min}=0.49$)
	Out-of-plane propagation in 2D kagome lattice structures (embedded design, β -FeSi ₂ rods in SiO ₂ background)	$\Delta\omega/\omega_c \geq 87.9\%$ ($\omega a/2\pi c _{min}=0.37$)
	3D complex hexagonal lattice structures	$\Delta\omega/\omega_c=47.4\%$ ($\omega a/2\pi c=1.03\sim 1.67$)

TABLE 7.1: Summary of achieved self-collimation performance in this work with previously reported results if applicable (★: new achievement)

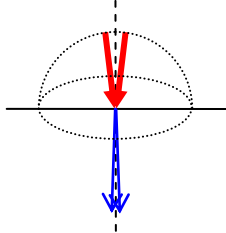
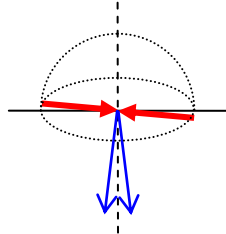
Self-collimation type	PC structures	Performance details
Broadband 3D virtual limited-angled self-collimation ($ \theta_{p/max} \leq 2^\circ$) (★) 	3D sc lattice structures [66]	$ \theta_i \leq 8^\circ$; $\Delta\omega/\omega_c = 11.8\%$ ($\omega a/2\pi c = 0.32 \sim 0.36$) †
	3D tetragonal lattice structures	$ \theta_i \leq 8^\circ$; $\Delta\omega/\omega_c = 25.5\%$ ($\omega a/2\pi c = 0.24 \sim 0.31$)
	Out-of-plane propagation in 2D kagome lattice structures (InSb rods in air background)	$ \theta_i \leq 8^\circ$; $\Delta\omega/\omega_c = 60.3\%$ ($\omega a/2\pi c = 0.22 \sim 0.41$)
	Out-of-plane propagation in 2D kagome lattice structures (embedded design, β -FeSi ₂ rods in SiO ₂ background)	$ \theta_i \leq 11^\circ$; $\Delta\omega/\omega_c = 38\%$ ($\omega a/2\pi c = 0.17 \sim 0.25$)
3D omnidirectional beam confinement (★) 	Out-of-plane propagation in 2D kagome lattice structures (InSb rods in air background)	$ \theta_{p/max} \leq 7^\circ$ at $\omega a/2\pi c = 0.38$ $ \theta_{p/max} \leq 5^\circ$ at $\omega a/2\pi c = 0.25$
	Out-of-plane propagation in 2D kagome lattice structures (embedded design, β -FeSi ₂ rods in SiO ₂ background)	$ \theta_{p/max} \leq 7^\circ$ at $\omega a/2\pi c = 0.2$

TABLE 7.1 (continued): Summary of achieved self-collimation performance in this work with previously reported results if applicable (★: new achievement)

†Determined (calculated by us) using the previously reported structure, where self-collimation was reported only at a single frequency

REFERENCES

- [1] D. N. Chigrin, S. Enoch, C. M. S. Torres, and G. Tayeb, "Self-guiding in two-dimensional photonic crystals," *Optics Express*, 11(10), p. 1203-1211 (2003).
- [2] R. E. Hamam, M. Ibanescu, S. G. Johnson, J. D. Joannopoulos, and M. Soljacic, "Broadband super-collimation in a hybrid photonic crystal structure," *Opt. Express*, 17(10), p. 8109-8118 (2009).
- [3] D. Gao, Z. Zhou, and D. S. Citrin, "Self-collimated waveguide bends and partial bandgap reflection of photonic crystals with parallelogram lattice," *J. Opt. Soc. Am. A*, 25(3), p. 791-795 (2008).
- [4] D. W. Prather, C. Chen, S. Shi, B. Miao, D. M. Pustai, S. Venkataraman, A. S. Sharkawy, G. J. Schneider, and J. A. Murakowski, "Ultralow-loss photonic crystal waveguides based on the self-collimation effect," *Photonic Crystal Materials and Devices II*, SPIE, 5360, p. 175 (2004).
- [5] J. Hou, D. Gao, H. Wu, and Z. Zhou, "Polarization insensitive self-collimation waveguide in square lattice annular photonic crystals," *Optics Communications*, 282(15), p. 3172-3176 (2009).
- [6] Y. Xu, X.-J. Chen, S. Lan, Q. Guo, W. Hu, and L.-J. Wu, "The all-angle self-collimating phenomenon in photonic crystals with rectangular symmetry," *Journal of Optics A: Pure and Applied Optics*, 10(8), p. 085201 (2008).
- [7] A. F. Matthews, S. K. Morrison, and Y. S. Kivshar, "Self-collimation and beam splitting in low-index photonic crystals," *Optics Communications*, 279(2), p. 313-319 (2007).
- [8] V. Zabelin, L. A. Dunbar, N. Le Thomas, R. Houdr, M. V. Kotlyar, L. O'Faolain, and T. F. Krauss, "Self-collimating photonic crystal polarization beam splitter," *Opt. Lett.*, 32(5), p. 530-532 (2007).
- [9] X. Yu, and S. Fan, "Bends and splitters for self-collimated beams in photonic crystals," *Applied Physics Letters*, 83(16), p. 3251-3253 (2003).
- [10] A. F. Matthews, "Experimental demonstration of self-collimation beaming and splitting in photonic crystals at microwave frequencies," *Optics Communications*, 282(9), p. 1789-1792 (2009).
- [11] C.-S. Kee, D.-K. Ko, and J. Lee, "Self-collimated beams in two-dimensional photonic crystals: Properties and applications," *Journal of the Korean Physical Society*, 51(4), p. 1479~1483 (2007).
- [12] D. Pustai, S. Shi, C. Chen, A. Sharkawy, and D. Prather, "Analysis of splitters for self-collimated beams in planar photonic crystals," *Opt. Express*, 12(9), p. 1823-

- 1831 (2004).
- [13] Y. Zhang, Y. Zhang, and B. Li, "Optical switches and logic gates based on self-collimated beams in two-dimensional photonic crystals," *Opt. Express*, 15(15), p. 9287-9292 (2007).
 - [14] X.-Y. Chen, H. Li, Y.-S. Qiu, Y.-F. Wang, and B. Ni, "Tunable Photonic Crystal Mach-Zehnder Interferometer Based on Self-collimation Effect," *Chinese Physics Letters*, 25(12), p. 4307-4310 (2008).
 - [15] D. Zhao, J. Zhang, P. Yao, X. Jiang, and X. Chen, "Photonic crystal Mach-Zehnder interferometer based on self-collimation," *Applied Physics Letters*, 90(23), p. 231114-3 (2007).
 - [16] T. Yamashita, "Unraveling photonic bands: characterization of self-collimation effects in two-dimensional photonic crystals," Ph.D. Dissertation, Georgia Institute of Technology (2005).
 - [17] W. Zhang, J. Liu, W.-P. Huang, and W. Zhao, "Self-collimating photonic-crystal wave plates," *Opt. Lett.*, 34(17), p. 2676 (2009).
 - [18] R. Iliew, C. Etrich, T. Pertsch, F. Lederer, and K. Staliunas, "Subdiffractive all-photonic crystal Fabry-Perot resonators," *Opt. Lett.*, 33(22), p. 2695 (2008).
 - [19] X.-P. Shen, K. Han, F. Yuan, H.-P. Li, Z.-Y. Wang, and Q. Zhong, "New Configuration of Ring Resonator in Photonic Crystal Based on Self-Collimation," *Chinese Physics Letters*, 25(12), p. 4288 (2008).
 - [20] D. Zhao, C. Zhou, Q. Gong, and X. Jiang, "Lasing cavities and ultra-fast switch based on self-collimation of photonic crystal," *Journal of Physics D: Applied Physics*, 41(11), p. 115108 (2008).
 - [21] T. P. White, C. M. de Sterke, R. C. McPhedran, and L. C. Botten, "Highly efficient wide-angle transmission into uniform rod-type photonic crystals," *Applied Physics Letters*, 87(11), p. 111107-3 (2005).
 - [22] M. Koshiba, "Wavelength Division Multiplexing and Demultiplexing With Photonic Crystal Waveguide Couplers," *J. Lightwave Technol.*, 19(12), p. 1970 (2001).
 - [23] A. Sharkawy, S. Shi, and D. W. Prather, "Multichannel Wavelength Division Multiplexing with Photonic Crystals," *Appl. Opt.*, 40(14), p. 2247 (2001).
 - [24] Y. Kanamori, M. Sasaki, and K. Hane, "Broadband antireflection gratings fabricated upon silicon substrates," *Opt. Lett.*, 24(20), p. 1422 (1999).
 - [25] H. Sai, H. Fujii, K. Arafune, Y. Ohshita, Y. Kanamori, H. Yugami, and M. Yamaguchi, "Wide-Angle Antireflection Effect of Subwavelength Structures for

- Solar Cells,” Japanese Journal of Applied Physics, 46(6A), p. 3333-3336 (2007).
- [26] C. C. Striemer, and P. M. Fauchet, “Dynamic etching of silicon for broadband antireflection applications,” Applied Physics Letters, 81(16), p. 2980 (2002).
- [27] H. Sai, Y. Kanamori, K. Arafune, Y. Ohshita, and M. Yamaguchi, “Light trapping effect of submicron surface textures in crystalline Si solar cells,” Progress in Photovoltaics: Research and Applications, 15(5), p. 415-423 (2007).
- [28] Y. M. Song, J. S. Yu, and Y. T. Lee, “Antireflective submicrometer gratings on thin-film silicon solar cells for light-absorption enhancement,” Opt. Lett., 35(3), p. 276 (2010).
- [29] Y. Park, E. Drouard, O. El Daif, X. Letartre, P. Viktorovitch, A. Fave, A. Kaminski, M. Lemiti, and C. Seassal, “Absorption enhancement using photonic crystals for silicon thin film solar cells,” Opt. Express, 17(16), p. 14312 (2009).
- [30] J. H. Karp, E. J. Tremblay, and J. E. Ford, “Planar micro-optic solar concentrator,” Opt. Express, 18(2), p. 1122 (2010).
- [31] M. Yan, P. Shum, and X. Yu, “Heterostructured photonic crystal fiber,” Photonics Technology Letters, 17(7), p. 1438-1440 (2005).
- [32] X. Yu, M. Yan, G. Ren, W. Tong, X. Cheng, J. Zhou, P. Shum, and N. Q. Ngo, “Nanostructure Core Fiber With Enhanced Performances: Design, Fabrication and Devices,” J. Lightwave Technol., 27(11), p. 1548 (2009).
- [33] F. Yaman, H. Pang, X. Xie, P. LiKamWa, and G. Li, "Silicon Photonic Crystal Fiber," Conference on Lasers and Electro-Optics/International Quantum Electronics Conference, Optical Society of America, p. CTuDD7 (2009).
- [34] W. Y. Liang, T. B. Wang, C. P. Yin, J. W. Dong, F. C. Leng, and H. Z. Wang, “Super-broadband non-diffraction guiding modes in photonic crystals with elliptical rods,” Journal of Physics D: Applied Physics, 43(7), p. 075103 (2010).
- [35] J. W. Goodman, *Introduction to Fourier Optics* (McGraw-Hill, Inc., 2005).
- [36] T. J. Suleski, “The Talbot Effect: Fresnel diffraction of amplitude and phase gratings,” Ph.D. Dissertation, Georgia Institute of Technology (1996).
- [37] M. V. Berry, and S. Klein, “Integer, fractional, and fractal Talbot effect,” Journal of Modern Optics, 43(10), p. 2139-2164 (1996).
- [38] J. R. Leger, and G. J. Swanson, “Efficient array illuminator using binary-optics phase plates at fractional-Talbot planes,” Opt. Lett., 15, p. 288-290 (1990).
- [39] J. D. Joannopoulos, S. G. Johnson, J. N. Winn, and R. D. Meade, *Photonic Crystals* (Princeton University Press, 2008).

- [40] K. Sakoda, *Optical Properties of Photonic Crystals* (Springer, 2005).
- [41] E. Yablonovitch, "Inhibited Spontaneous Emission in Solid-State Physics and Electronics," *Physical Review Letters*, 58(20), p. 2059 (1987).
- [42] S. John, "Strong localization of photons in certain disordered dielectric superlattices," *Physical Review Letters*, 58(23), p. 2486 (1987).
- [43] C. M. Soukoulis, *Photonic Band Gap Materials* (Kluwer Academic Publishers, 1996).
- [44] T. Y. M. Chan, O. Toader, and S. John, "Photonic band gap templating using optical interference lithography," *Physical Review E*, 71(4), p. 046605 (2005).
- [45] A. Bruyant, G. Lerondel, P. J. Reece, and M. Gal, "All-silicon omnidirectional mirrors based on one-dimensional photonic crystals," *Applied Physics Letters*, 82(19), p. 3227 (2003).
- [46] Y. Akahane, M. Mochizuki, T. Asano, Y. Tanaka, and S. Noda, "Design of a channel drop filter by using a donor-type cavity with high-quality factor in a two-dimensional photonic crystal slab," *Applied Physics Letters*, 82(9), p. 1341 (2003).
- [47] M. Qiu, and B. Jaskorzynska, "Design of a channel drop filter in a two-dimensional triangular photonic crystal," *Applied Physics Letters*, 83(6), p. 1074 (2003).
- [48] A. Chutinan, and S. Noda, "Waveguides and waveguide bends in two-dimensional photonic crystal slabs," *Physical Review B*, 62(7), p. 4488 (2000).
- [49] S. G. Johnson, P. R. Villeneuve, S. Fan, and J. D. Joannopoulos, "Linear waveguides in photonic-crystal slabs," *Physical Review B*, 62(12), p. 8212 (2000).
- [50] M. Loncar, T. Doll, J. Vuckovic, and A. Scherer, "Design and Fabrication of Silicon Photonic Crystal Optical Waveguides," *J. Lightwave Technol.*, 18(10), p. 1402 (2000).
- [51] A. Ghaffari, M. Djavid, and M. S. Abrishamian, "Bi-periodic photonic crystal Y-splitter," *Physica E: Low-dimensional Systems and Nanostructures*, 41(8), p. 1495 (2009).
- [52] Y. Akahane, T. Asano, B.-S. Song, and S. Noda, "High-Q photonic nanocavity in a two-dimensional photonic crystal," *Nature*, 425(6961), p. 944 (2003).
- [53] H. Hirayama, T. Hamano, and Y. Aoyagi, "Novel surface emitting laser diode using photonic band-gap crystal cavity," *Applied Physics Letters*, 69(6), p. 791 (1996).
- [54] A. Matthews, X. H. Wang, Y. Kivshar, and M. Gu, "Band-gap properties of two-

- dimensional low-index photonic crystals,” *Applied Physics B: Lasers and Optics*, 81(2), p. 189-192 (2005).
- [55] K. M. Ho, C. T. Chan, and C. M. Soukoulis, “Existence of a photonic gap in periodic dielectric structures,” *Physical Review Letters*, 65(25), p. 3152 (1990).
- [56] A. Berrier, M. Mulot, M. Swillo, M. Qiu, L. Thylén, A. Talneau, and S. Anand, “Negative Refraction at Infrared Wavelengths in a Two-Dimensional Photonic Crystal,” *Physical Review Letters*, 93(7), p. 073902 (2004).
- [57] M. Notomi, “Theory of light propagation in strongly modulated photonic crystals: Refractionlike behavior in the vicinity of the photonic band gap,” *Physical Review B*, 62(16), p. 10696 (2000).
- [58] Z. Tang, R. Peng, D. Fan, S. Wen, H. Zhang, and L. Qian, “Absolute left-handed behaviors in a triangular elliptical-rod photonic crystal,” *Opt. Express*, 13(24), p. 9796-9803 (2005).
- [59] S. Feng, L. Ao, Y.-Q. Wang, Z.-Y. Li, and D.-Z. Zhang, “Negative Refraction and Near-Field Imaging of an Elliptical-Rod Photonic Crystal Slab in the Second Band,” *Chinese Physics Letters*, 24(9), p. 2675-2677 (2007).
- [60] Y. J. Huang, W. T. Lu, and S. Sridhar, “Alternative approach to all-angle negative refraction in two-dimensional photonic crystals,” *Physical Review A (Atomic, Molecular, and Optical Physics)*, 76(1), p. 013824-5 (2007).
- [61] Y. Jin, and S. He, “Negative refraction of complex lattices of dielectric cylinders,” *Physics Letters A*, 360(3), p. 461 (2007).
- [62] C. Luo, S. G. Johnson, J. D. Joannopoulos, and J. B. Pendry, “All-angle negative refraction without negative effective index,” *Physical Review B*, 65(20), p. 201104 (2002).
- [63] D. Tang, L. Chen, and W. Ding, “Efficient beaming from photonic crystal waveguides via self-collimation effect,” *Applied Physics Letters*, 89(13), p. 131120 (2006).
- [64] J. Shin, and S. Fan, “Conditions for self-collimation in three-dimensional photonic crystals,” *Opt. Lett.*, 30(18), p. 2397 (2005).
- [65] J. Witzens, M. Loncar, and A. Scherer, “Self-collimation in planar photonic crystals,” *Ieee Journal Of Selected Topics In Quantum Electronics*, 8(6), p. 1246-1257 (2002).
- [66] D. W. Prather, S. Y. Shi, J. Murakowski, G. J. Schneider, A. Sharkawy, C. H. Chen, B. L. Miao, and R. Martin, “Self-collimation in photonic crystal structures: a new paradigm for applications and device development,” *Journal Of Physics D-Applied Physics*, 40(9), p. 2635-2651 (2007).

- [67] H. Kosaka, T. Kawashima, A. Tomita, M. Notomi, T. Tamamura, T. Sato, and S. Kawakami, "Self-collimating phenomena in photonic crystals," *Applied Physics Letters*, 74(9), p. 1212-1214 (1999).
- [68] Y. Ogawa, Y. Omura, and Y. Iida, "Study on Self-Collimated Light-Focusing Device Using the 2-D Photonic Crystal With a Parallelogram Lattice," *J. Lightwave Technol.*, 23(12), p. 4374 (2005).
- [69] J.-M. Park, S.-G. Lee, H. Y. Park, and J.-E. Kim, "Efficient beaming of self-collimated light from photonic crystals," *Opt. Express*, 16(25), p. 20354 (2008).
- [70] L.-J. Wu, M. Mazilu, and T. F. Krauss, "Beam steering in planar-photonic crystals: from superprism to supercollimator," *Journal of Lightwave Technology*, 21(2), p. 561~566 (2003).
- [71] A. I. Cabuz, E. Centeno, and D. Cassagne, "Superprism effect in bidimensional rectangular photonic crystals," *Applied Physics Letters*, 84(12), p. 2031-2033 (2004).
- [72] A. Sharkawy, D. Pustai, S. Shi, D. Prather, S. McBride, and P. Zanzucchi, "Modulating dispersion properties of low index photonic crystal structures using microfluidics," *Opt. Express*, 13(8), p. 2814-2827 (2005).
- [73] L. Wang, W. Jiang, X. Chen, J. Chen, S. Zhang, and R. Chen, "Superprism phenomena in 2 D low index contrast polymer photonic crystal," *SPIE*, 6475, p. 647510 (2007).
- [74] R. Iliew, C. Etrich, U. Peschel, F. Lederer, M. Augustin, H. J. Fuchs, D. Schelle, E. B. Kley, S. Nolte, and A. Tunnermann, "Diffractionless propagation of light in a low-index photonic-crystal film," *Applied Physics Letters*, 85(24), p. 5854 (2004).
- [75] Y.-C. Chuang, and T. J. Suleski, "Optical characteristics of photonic crystals based on the fractional Talbot effect," *Photonic and Phononic Crystal Materials and Devices IX, Proc. SPIE*, 7223, p. 72230P (2009).
- [76] A. T. Cannistra, and T. J. Suleski, "Characterization of hybrid molding and lithography for SU-8 micro-optical components," *Advanced Fabrication Technologies for Micro/Nano Optics and Photonics II, SPIE*, 7205, p. 720517 (2009).
- [77] H. Kosaka, T. Kawashima, A. Tomita, M. Notomi, T. Tamamura, T. Sato, and S. Kawakami, "Superprism phenomena in photonic crystals," *Physical Review B*, 58(16), p. 10096-10099 (1998).
- [78] S. Foteinopoulou, and C. M. Soukoulis, "Electromagnetic wave propagation in two-dimensional photonic crystals: A study of anomalous refractive effects," *Physical Review B*, 72, p. (2005).

- [79] S. Kawakami, O. Hanaizumi, T. Sato, Y. Ohtera, T. Kawashima, N. Yasuda, Y. Takei, and K. Miura, "Fabrication of 3D photonic crystals by autocloning and its applications," *Electronics and Communications in Japan (Part II: Electronics)*, 82(9), p. 43-52 (1999).
- [80] Y. Xu, X.-J. Chen, S. Lan, Q.-F. Dai, Q. Guo, and L.-J. Wu, "Polarization-independent self-collimation based on pill-void photonic crystals with square symmetry," *Opt. Express*, 17(6), p. 4903 (2009).
- [81] C. W. Neff, "Optical Properties of Superlattice Photonic Crystals," Ph.D. Dissertation, Georgia Institute of Technology (2005).
- [82] Z. Lu, S. Shi, J. A. Murakowski, G. J. Schneider, C. A. Schuetz, and D. W. Prather, "Experimental Demonstration of Self-Collimation inside a Three-Dimensional Photonic Crystal," *Physical Review Letters*, 96(17), p. 173902 (2006).
- [83] D. W. Prather, S. Shi, S. Venkataraman, Z. Lu, J. Murakowski, and G. J. Schneider, "Self-collimation in three-dimensional photonic crystals," *Photonic Crystal Materials and Devices III, Proc. SPIE*, 5733, p. 84-93 (2005).
- [84] R. Iliew, C. Etrich, and F. Lederer, "Self-collimation of light in three-dimensional photonic crystals," *Opt. Express*, 13(18), p. 7076 (2005).
- [85] E. Soliveres, V. Espinosa, I. Perez-Arjona, V. J. Sanchez-Morcillo, and K. Staliunas, "Self collimation of ultrasound in a three-dimensional sonic crystal," *Applied Physics Letters*, 94(16), p. 164101 (2009).
- [86] Y. C. Chuang, and T. J. Suleski, "Complex rhombus lattice photonic crystals for broadband all-angle self-collimation," *Journal of Optics*, 12(3), p. 035102 (2010).
- [87] S. Johnson, and J. Joannopoulos, "Block-iterative frequency-domain methods for Maxwell's equations in a planewave basis," *Opt. Express*, 8(3), p. 173 (2001).
- [88] S. Guo, and S. Albin, "Simple plane wave implementation for photonic crystal calculations," *Opt. Express*, 11(2), p. 167-175 (2003).
- [89] R. C. Rumpf, "Design and optimization of nano-optical elements by coupling fabrication to optical behavior," Ph.D. Dissertation, The University of Central Florida (2006).
- [90] S. Shi, C. Chen, and D. W. Prather, "Plane-wave expansion method for calculating band structure of photonic crystal slabs with perfectly matched layers," *J. Opt. Soc. Am. A*, 21(9), p. 1769 (2004).
- [91] C. Kittel, *Introduction to Solid State Physics* (John Wiley & Sons, 1996).
- [92] D. C. Champeney, *Fourier transforms and their physical applications* (Academic

- Press, 1973).
- [93] G. B. Arfken, and H. J. Weber, *Mathematical methods for physicists* (Academic Press, 2001).
 - [94] S. Guo, "Plane Wave Expansion Method for Photonic Band Gap Calculation Using MATLAB," Manual version 1, Old Dominion University (2003).
 - [95] BandSOLVE, <http://www.rsoftdesign.com/products.php?sub=Component+Design&itm=BandSOLVE>
 - [96] A. Taflove, and S. C. Hagness, *Computational Electrodynamics: the Finite-Difference Time-Domain Method* (Artech House, Inc., 2000).
 - [97] K. S. Yee, "Numerical Solution of Initial Boundary Value Problems Involving Maxwell's Equations in Isotropic Media," IEEE transactions on antennas and propagation, AP-14, p. 302 (1966).
 - [98] FullWAVE, <http://www.rsoftdesign.com/products.php?sub=Component+Design&itm=FullWAVE>
 - [99] J.-P. Berenger, "A perfectly matched layer for the absorption of electromagnetic waves," Journal of Computational Physics, 114, p. 185-220 (1994).
 - [100] M. G. Moharam, and T. K. Gaylord, "Rigorous Coupled-Wave Theory of Planar Gratings," Journal of the Optical Society of America, 70(12), p. 1631-1632 (1980).
 - [101] M. G. Moharam, "Rigorous Coupled-Wave Analysis of Planar-Grating Diffraction," Journal of the Optical Society of America, 71(7), p. 811-818 (1981).
 - [102] M. G. Moharam, "Formulation for Stable and Efficient Implementation of the Rigorous Coupled-Wave Analysis of Binary Gratings," Journal of the Optical Society of America A, 12(5), p. 1068-1076 (1995).
 - [103] GSolver, <http://www.gsolver.com/>
 - [104] L. Rayleigh, "On the dynamical theory of gratings," Proceedings of the Royal Society of London, A79, p. 399-416 (1907).
 - [105] E. Noponen, "Electromagnetic Theory of Diffractive Optics," Ph.D. Dissertation, Helsinki University of Technology (1994).
 - [106] M. Neviere, and E. Popov, *Light Propagation in Periodic Media-Diffractive Theory and Design* (Marcel Dekker, Inc., 2003).

- [107] K. Patorski, "The self-imaging phenomenon and its applications," *Progress in Optics*, 27, p. 1-108 (1989).
- [108] M. E. Testorf, T. J. Suleski, and Y.-C. Chuang, "Design of Talbot array illuminators for three-dimensional intensity distributions," *Opt. Express*, 14(17), p. 7623 (2006).
- [109] F. García-Santamaría, C. López, F. Meseguer, F. López-Tejiera, J. Sánchez-Dehesa, and H. T. Miyazaki, "Opal-like photonic crystal with diamond lattice," *Applied Physics Letters*, 79(15), p. 2309 (2001).
- [110] F. García-Santamaría, H. T. Miyazaki, A. Urquía, M. Ibisate, M. Belmonte, N. Shinya, F. Meseguer, and C. López, "Nanorobotic Manipulation of Microspheres for On-Chip Diamond Architectures," *Advanced Materials*, 14(16), p. 1144-1147 (2002).
- [111] M. Ritala, and M. Leskela, *Handbook of Thin Film Materials* (Academic Press, 2002).
- [112] MicroChem, http://www.microchem.com/products/pdf/SU-82000DataSheet2000_5thru2015Ver4.pdf
- [113] E. D. Palik, and G. Ghosh, *Handbook of Optical Constants of Solids* (Academic Press, 1998).
- [114] J. T. Verdeyen, *Laser Electronics* (Prentice hall, 1981).
- [115] J. Witzens, M. Hochberg, T. Baehr-Jones, and A. Scherer, "Mode matching interface for efficient coupling of light into planar photonic crystals," *Physical Review E*, 69(4), p. 046609 (2004).
- [116] Q. Wang, Y. Cui, C. Yan, L. Zhang, and J. Zhang, "Highly efficient directional emission using a coupled multi-channel structure to a photonic crystal waveguide with surface modification," *Journal of Physics D: Applied Physics*, 41(10), p. 105110 (2008).
- [117] F. J. Lawrence, L. C. Botten, K. B. Dossou, and C. M. de Sterke, "Antireflection coatings for two-dimensional photonic crystals using a rigorous impedance definition," *Applied Physics Letters*, 93(12), p. 121114-3 (2008).
- [118] Z. Li, E. Ozbay, H. Chen, J. Chen, F. Yang, and H. Zheng, "Resonant cavity based compact efficient antireflection structures for photonic crystals," *Journal of Physics D: Applied Physics*, 40(19), p. 5873 (2007).
- [119] M. Elwenspoek, and H. V. Jansen, *Silicon Micromachining* (Cambridge University Press, 2004).
- [120] N. Susa, "Large absolute and polarization-independent photonic band gaps for

- various lattice structures and rod shapes,” *Journal of Applied Physics*, 91(6), p. 3501 (2002).
- [121] F. Wen, S. David, X. Checoury, M. El Kurdi, and P. Boucaud, “Two-dimensional photonic crystals with large complete photonic band gaps in both TE and TM polarizations,” *Opt. Express*, 16(16), p. 12278 (2008).
- [122] Y. Maeda, “Semiconducting β -FeSi₂ towards optoelectronics and photonics,” *Thin Solid Films*, 515(22), p. 8118 (2007).
- [123] H. Takeda, T. Takashima, and K. Yoshino, “Flat photonic bands in two-dimensional photonic crystals with kagome lattices,” *Journal of Physics: Condensed Matter*, 16(34), p. 6317 (2004).
- [124] P. J. A. Sazio, A. Amezcua-Correa, C. E. Finlayson, J. R. Hayes, T. J. Scheidemantel, N. F. Baril, B. R. Jackson, D.-J. Won, F. Zhang, E. R. Margine, V. Gopalan, V. H. Crespi, and J. V. Badding, “Microstructured Optical Fibers as High-Pressure Microfluidic Reactors,” *Science*, 311(5767), p. 1583 (2006).
- [125] C. E. Finlayson, A. Amezcua-Correa, P. J. A. Sazio, N. F. Baril, and J. V. Badding, “Electrical and Raman characterization of silicon and germanium-filled microstructured optical fibers,” *Applied Physics Letters*, 90(13), p. 132110 (2007).
- [126] J. Ballato, T. Hawkins, P. Foy, R. Stolen, B. Kokuoz, M. Ellison, C. McMillen, J. Reppert, A. M. Rao, M. Daw, S. R. Sharma, R. Shori, O. Stafsudd, R. R. Rice, and D. R. Powers, “Silicon optical Fiber,” *Opt. Express*, 16(23), p. 18675 (2008).
- [127] B. L. Scott, K. Wang, and G. Pickrell, “Fabrication of n-Type Silicon Optical Fibers,” *Photonics Technology Letters*, 21(24), p. 1798-1800 (2009).
- [128] P. Russell, “Photonic Crystal Fibers,” *Science*, 299(5605), p. 358 (2003).
- [129] E. Noponen, and J. Turunen, “Electromagnetic Theory of Talbot Imaging,” *Optics Communications*, 98, p. 132-140 (1993).

APPENDIX A: PWEM SOURCE CODE

```
% 1.This is a program to calculate band structures of general 2D parallelogram lattice
% structures, including square, rectangular, triangular, rhombus lattice structures.
% 2.Required user-defined functions:
% "unitcellMatrix.m","fftcoef.m","kpoints.m","SolveEigen.m"
% and "calculatek.m","generatek.m","generatesection.m","plotseg.m"
% 3.Required to import the previously defined dielectric function ("int1")
% and primitive lattice vectors ("t1 t2 t3")
% Copyright (c) 2008 Yi-Chen Chuang

% ***** Form orthogonal unit cell from the original dielectric function
Nt1= 2^9+1; % required an odd number
Nt2= round(norm(t2)/norm(t1)*(Nt1-1));
if rem(Nt2,2)==0
    Nt2= Nt2+1;
end
originx=1;originz=1;
[int2]= unitcellMatrix(int1,t1,t2,t3,originx,originz,delx,dely,Nt1,Nt2);
% ***** Calculate reciprocal lattice vectors *****
denominator= dot(t1,cross(t2,t3));
T1= 2*pi*cross(t2,t3)/denominator;
T2= 2*pi*cross(t3,t1)/denominator;
% ***** FFT & construct convolution matrix *****
minOrder= 4; %P or Q =minOrder
[ConvoMatrix,G,P,Q]= fftcoef(int2,Nt1,Nt2,minOrder,T1,T2);
% ***** Define special k-points in the 1st BZ *****
[kpath,Q1,Q2,Q3,Q4,Q5,Q6,tmpx,Nk]= kpoints(T1,T2);
% ***** Define k points for EFC calculation *****
kxmax= T1(1);
kymax= T2(2);
Nkx= 40;
Nky= 40;
delkx= T1(1)/(Nkx-1);
delky= T2(2)/(Nky-1);
[kx,ky]= meshgrid(0:delkx:kxmax,0:delky:kymax);
kall= zeros(numel(kx),2);
kall(:,1)= reshape(kx,numel(kx),1);
kall(:,2)= reshape(ky,numel(kx),1);
% ***** Solve eigen function *****
numBand=5;
[freq,Polarization]= SolveEigen(numBand,kall,G,ConvoMatrix);
% ***** Plot EFCs *****
startband= 5;
endband= 5;
for band= startband:endband
    w= zeros(size(kx));
    for ii= 1:numel(kx)
        w(ii)= freq(band,ii);
    end
end
% Extend the data from the 1st quadrant to cover the whole 1st BZ (4 quadrants)
[rowqua1,colqua1]= size(w); % 1st quadrant & kx- and ky- axes;
```

```

freq_qua2= fliplr(w(:,2:colqua1)); %2nd quadrant
freq_up= [freq_qua2 w];
freq_down= flipud(freq_up(2:rowqua1,:)); %3rd and 4th quadrants
freq_1stBZ= [freq_down;freq_up];
figure;
[k1stBZx,k1stBZy]= meshgrid(-T1(1):delkx:T1(1),-T2(2):delky:T2(2));
contour(k1stBZx,k1stBZy,freq_1stBZ); %correct
axis equal
h= colorbar;
h= get(h,'Title');
set(h,'String','w/2\pic');
xlabel('kx')
ylabel('ky')
text(0,0,'\Gamma');
hold on;
if abs(Q1-Q2)<10^-3|abs(Q3-Q4)<10^-3|abs(Q2-Q3)<10^-3; % rectangular
    % draw 1BZ
    plotseg(50,Q3,Q5);% plotseg(50,kM1,kM2); %kM1=Q3;kM2=Q5;
    plotseg(50,Q5,-Q3);% plotseg(50,kM2,kM3); %kM3=-kM1=-Q3
    plotseg(50,-Q3,-Q5);% plotseg(50,kM3,kM4); %kM4=-kM2=-Q5
    plotseg(50,-Q5,Q3);% plotseg(50,kM4,kM1);
    text(Q3(1),Q3(2),'M1');
    kX1=(Q3-Q5)./2; %kX1=(kM1+kM4)./2=(Q3-Q5)./2
    kX2=(Q3+Q5)./2; %kX2=(kM1+kM2)./2=(Q3+Q5)./2
    text(kX1(1),kX1(2),'X1');
    text(kX2(1),kX2(2),'X2');
else
    plotseg(50,Q3,Q4);
    plotseg(50,Q4,Q5);
    plotseg(50,Q5,Q6);
    plotseg(50,Q6,-Q4);
    plotseg(50,-Q4,-Q5);
    plotseg(50,-Q5,Q3);
    text(Q3(1),Q3(2),'K1');
    text(Q4(1),Q4(2),'K2');
    text(Q5(1),Q5(2),'K3');
    kM1=(Q3+Q4)./2;
    kM2=(Q4+Q5)./2;
    kM3=(Q5+Q6)./2;
    text(kM1(1),kM1(2),'M1');
    text(kM2(1),kM2(2),'M2');
    text(kM3(1),kM3(2),'M3');
end
if Polarization==1
    title(['TM EFCs; P=',num2str(P),'; Q=',num2str(Q)];['# of plane waves:',num2str((2*P+1)*(2*Q+1)),';
    er(scatterers)=' ,num2str(er_s),'; er(bg)=' ,num2str(er_bg),'; band ',num2str(band)]])
    saveas(gcf,['EFCtMband',num2str(band)],'jpg');
    save(['EFCDataTMband',num2str(band)]);
elseif Polarization==2
    title(['TE EFCs; P=',num2str(P),'; Q=',num2str(Q)];['# of plane waves:',num2str((2*P+1)*(2*Q+1)),';
    er(scatterers)=' ,num2str(er_s),'; er(bg)=' ,num2str(er_bg),'; band ',num2str(band)]])
    saveas(gcf,['EFCtEband',num2str(band)],'jpg');
    save(['EFCDataTEband',num2str(band)]);
end
end
end

```

Required user-defined MATLAB functions:

"unitcellMatrix.m"-----

% This function form orthogonal unit cell from the original dielectric function; 2/9/10 Yi-Chen Chuang

```
function [int2]=unitcellMatrix(int1,t1,t2,t3,originx,originz,deltx,deltz,Nt1,Nt2)
% Define the number of the mesh grids of the converted unit cell
% Nt1 must be an odd # since it corresponds to the Fourier Coefficients in different orders
if rem(Nt1,2)==0 || rem(Nt2,2)==0 %if Nt1 or Nt2 is an even number
    display('Warning: Nt1 or Nt2 is an even number...the result will go wrong');
end
delt1=norm(t1)/(Nt1-1);
delt2=norm(t2)/(Nt2-1);
% Form converted rectangular unit cell for FFT from the oblique indexes
int2=zeros(Nt2,Nt1);
for m=1:size(int2,2);
    for n=1:size(int2,1);
        xyzcord=[m-1,n-1,0]*[delt1/norm(t1) 0 0;0 delt2/norm(t2) 0;0 0 0]*[t1(1) t1(2) t1(3);t2(1) t2(2)
            t2(3);t3(1) t3(2) t3(3)];
        xyzindex=[round(xyzcord(1)/deltx)+originz,round(xyzcord(2)/deltx)+originx];
        int2(n,m)=int1(xyzindex(2),xyzindex(1));
    end
end
clear m n xyzindex
```

"fftcoef.m"-----

% This function do FFT & build convolution matrix; 2/9/10 Yi-Chen Chuang

```
function [ConvoMatrix,G,P,Q]=fftcoef(int2,Nt1,Nt2,minOrder,T1,T2)
FourierCoeff=fftshift(1/(Nt2*Nt1)*fft2(int2)); % Shift zero-frequency component to center of spectrum
% Note: size(int2)=[Nt2,Nt1]; % Note: (2P+1)/(2Q+1)=Nt1/Nt2=norm(t1)/norm(t2)=norm(T2)/norm(T1)
if Nt1>=Nt2
    Q=minOrder;
    P=round((Nt1/Nt2*(2*Q+1)-1)/2); %so that P>Q (assigned)
elseif Nt1<Nt2
    P=minOrder;
    Q=round((Nt2/Nt1*(2*P+1)-1)/2); %so that gurentee Q>=P(assigned)
end
ConvoMatrix=zeros((2*P+1)*(2*Q+1));
G=zeros((2*P+1)*(2*Q+1),2);
for n=1:(2*Q+1);
    for m=1:(2*P+1)
        i=m+(n-1)*(2*P+1); % i-th row of the Convolution Matrix=i-th row of the Expansion vectors
        G(i,:)=((m-1)-P)*[T2(1),T2(2)]+((n-1)-Q)*[T1(1),T1(2)]; %Expansion vectors
        for rr=1:(2*Q+1)
            for q=1:(2*P+1)
                j=q+(rr-1)*(2*P+1); % j-th column of the Convolution Matrix
                Nt1c=(Nt1+1)/2;
                Nt2c=(Nt2+1)/2;
                ConvoMatrix(i,j)=FourierCoeff(Nt2c+m-q,Nt1c+n-rr); %follow (eq.6.27)
            end
        end
    end
end; clear n m i rr q j
```

```

"kpoinits.m"-----
% This function obtains special k-points of the 1st BZ; 2/9/10 Yi-Chen Chuang

function [kpoinits,Q1,Q2,Q3,Q4,Q5,Q6,tmpx,Nk]=kpoinits(T1,T2)
% Define special k-points from the reciprocal lattice vectors
% General lattice points in the k-space, assuming the vector a is aligned to horizontal axis
P1=T1;
P2=T1+T2;
P3=T2;
P4=-T1+T2;
P5=-P1;
P6=-P2;
P7=-P3;
P8=-P4;
P10=P1+P2; %=2*T1+T2
P12=P2+P3; %=T1+2*T2
P14=P3+P4; %=-T1+2*T2
P16=P4+P5; %=-2*T1+T2
P18=-P10;
P20=-P12;
P22=-P14;
P24=-P16;
% In the very general 24 mesh points, only 16 points can be potential closest P points since some of the
% points are behind others even if their norm might be smaller
% Determine the closest 6 lattice points in the k-space
NearbyP=[P1;P2;P3;P4;P5;P6;P7;P8;P10;P12;P14;P16;P18;P20;P22;P24];
NearbyPnorm=(NearbyP(:,1).^2+NearbyP(:,2).^2+NearbyP(:,3).^2).^0.5;
[NearbyPnormSort index]=sort(NearbyPnorm);
ClosestNearbyP=[NearbyP(index(1),:);NearbyP(index(2),:);NearbyP(index(3),:);NearbyP(index(4),:);Near
byP(index(5),:);NearbyP(index(6),:)];
% Determine the sequence of these lattice points in the k-space
PcpX=ClosestNearbyP(:,1)+1i*ClosestNearbyP(:,2); % convert to complex coordinates
ang=angle(PcpX)/pi; %to determine the phase angle to "locate" these points
[ArrP index2]=sort(ang);
Q1=calculatek(ClosestNearbyP(index2(1),:),ClosestNearbyP(index2(2),:));
Q2=calculatek(ClosestNearbyP(index2(2),:),ClosestNearbyP(index2(3),:));
Q3=calculatek(ClosestNearbyP(index2(3),:),ClosestNearbyP(index2(4),:));
Q4=calculatek(ClosestNearbyP(index2(4),:),ClosestNearbyP(index2(5),:));
Q5=calculatek(ClosestNearbyP(index2(5),:),ClosestNearbyP(index2(6),:));
Q6=calculatek(ClosestNearbyP(index2(6),:),ClosestNearbyP(index2(1),:));
% Note: Q1~Q6 are defined in counter-clockwise order;
% Note: Q1, whoever the phase angle is smallest, is likely to be in the 3rd quadrant
% Define special k-points of the 1BZ chosen from the general points
if abs(Q2-Q3)<10^-3|abs(Q3-Q4)<10^-3|abs(Q1-Q2)<10^-3 % rectangular
if abs(Q2-Q3)<10^-3 % Q2=Q3
kM2=Q4; %N-W corner
else %Q3=Q4 or Q1=Q2
kM2=Q5; %N-W corner
end
kX1=(Q3+(-kM2))./2; %E side; kX1=(kM1+kM4)./2;
kX2=(Q3+kM2)./2; %N side; kX2=(kM1+kM2)./2;
[k1,Nk1,absDelK1]=generatek(10,[0,0,0],kX1); % Gamma-X1(E side)
[k2,Nk2,absDelK2]=generatek(10,kX1,Q3); % X1-M1(N-E corner); kM1=Q3
[k3,Nk3,absDelK3]=generatek(10,Q3,[0,0,0]); % M1-Gamma

```

```

[k4,Nk4,absDelK4]=generatek(10,[0,0,0],kX2); % Gamma-X2(N side)
[k5,Nk5,absDelK5]=generatek(10,kX2,Q3); % X2-M1
kpoints=[zeros(1,2);k1;k2;k3;k4;k5]; % Gamma-X1-M1-Gamma-X2-M1
% for plotting purpose
Nk=[Nk1,Nk2,Nk3,Nk4,Nk5];
absDelK=[absDelK1,absDelK2,absDelK3,absDelK4,absDelK5];
tmpx=generatesection(Nk,absDelK);
else % other general cases
% kK1=Q3; kK2=Q4; kK3=Q5; kK4=Q6;
kM1=(Q3+Q4)/2; % kM1=(kK1+kK2)/2
kM2=(Q4+Q5)/2; % kM2=(kK2+kK3)/2;
kM3=(Q5+Q6)/2; % kM3=(kK3+kK4)/2;
[k1,Nk1,absDelK1]=generatek(10,[0,0,0],Q3); % Gamma-K1;
[k2,Nk2,absDelK2]=generatek(10,Q3,kM1); % K1-M1;
[k3,Nk3,absDelK3]=generatek(10,kM1,[0,0,0]); % M1-Gamma;
[k4,Nk4,absDelK4]=generatek(10,[0,0,0],Q4); % Gamma-K2
[k5,Nk5,absDelK5]=generatek(10,Q4,kM2); % K2-M2;
[k6,Nk6,absDelK6]=generatek(10,kM2,[0,0,0]); % M2-Gamma
[k7,Nk7,absDelK7]=generatek(10,[0,0,0],Q5); % Gamma-K3
[k8,Nk8,absDelK8]=generatek(10,Q5,kM3); % K3-M3
[k9,Nk9,absDelK9]=generatek(10,kM3,[0,0,0]); % M3-Gamma
kpoints=[zeros(1,2);k1;k2;k3;k4;k5;k6;k7;k8;k9]; % Ga-K1-M1-Ga-K2-M2-Ga-K3-M3-Ga
% for plotting purpose
Nk=[Nk1,Nk2,Nk3,Nk4,Nk5,Nk6,Nk7,Nk8,Nk9];
absDelK=[absDelK1,absDelK2,absDelK3,absDelK4,absDelK5,absDelK6,absDelK7,absDelK8,absDelK9];
tmpx=generatesection(Nk,absDelK);
end

```

"SolveEigen.m"-----

```

function [freq,Polarization]=SolveEigen(numBand,kpoints,G,ConvoMatrix)
display('Type in 1 for TM mode; 2 for TE mode. (based on Joannopoulos definition)')
Polarization=input('Polarization:');
freq=zeros(numBand,length(kpoints));
if Polarization==1;
% Guo's TM; Tipper's TE...(only Ha,Hb,Ec; Ea=Eb=Hc=0)
Beta=zeros(1,length(G));
for ii=1:length(kpoints);ii
for jj=1:length(G)
beta=kpoints(ii,:)+G(jj,:); % TM
Beta(jj)=(beta(1)^2+beta(2)^2)^0.5; % TM
end
M=abs(Beta'*Beta).*inv(ConvoMatrix); % TM
d=sort(abs(eig(M)));
freq(:,ii)=sqrt(abs(d(1:numBand)))/(2*pi); % select the number of eigen-values to shown by d(1:#)
end
elseif Polarization==2;
% Guo's TE; Tipper's TM...(only Ea,Eb,Hc; Ha=Hb=Ec=0)
Beta=zeros(length(G),2);
for ii=1:length(kpoints);ii %for non-symmetric lattice, have to calculate the whole upper k-space
for jj=1:length(G)
beta=kpoints(ii,:)+G(jj,:);
Beta(jj,1)=beta(1);
Beta(jj,2)=beta(2);
end
end

```



```

M=(Beta*Beta').*inv(ConvMatrix);
d=sort(abs(eig(M)));
freq(:,ii)=sqrt(abs(d(1:numBand)))/(2*pi); % select the number of eigen-values to shown by d(1:#)
end
end
clear ii jj Beta beta M

```

"calculatek.m"-----
 % This program calculates the coordinates of special k point from the coordinates of two chosen adjacent "atoms" in the k-space

```

function Kcoordinates=calculatek(Pstart,Pend)
if round(Pstart(2)*1000)==0; % to make sure Pstart(2) is really small
    Kcoordinates=( [1 0 0;Pend(1)/Pend(2) 1 0;0 0 1] \ [Pstart(1);Pend(1)^2/Pend(2)+Pend(2);0] ./2)';
elseif round(Pend(2)*1000)==0 % to make sure Pend(2) is really small
    Kcoordinates=( [Pstart(1)/Pstart(2) 1 0;1 0 0;0 0 1] \ [Pstart(1)^2/Pstart(2)+Pstart(2);Pend(1);0] ./2)';
else
    Kcoordinates=( [Pstart(1)/Pstart(2) 1 0;Pend(1)/Pend(2) 1 0;0 0 1] \ [Pstart(1)^2/Pstart(2)+Pstart(2);Pend(1)^2/Pend(2)+Pend(2);0] ./2)';
end
end

```

"generatek.m"-----

```

function [k,Nk,absDelK]=generatek(Nk,Begink,Endk)
k=zeros(Nk,2);
DelK1=(Endk(1)-Begink(1))/Nk;
DelK2=(Endk(2)-Begink(2))/Nk;
if round(DelK1*1000)==0 % to make sure DelK1 is really small
    k(:,1)=Begink(1);
    k(:,2)=(Begink(2)+DelK2):DelK2:Endk(2);
elseif round(DelK2*1000)==0 % to make sure DelK2 is really small
    k(:,1)=(Begink(1)+DelK1):DelK1:Endk(1);
    k(:,2)=Begink(2);
else
    k(:,1)=(Begink(1)+DelK1):DelK1:Endk(1);
    k(:,2)=(Begink(2)+DelK2):DelK2:Endk(2);
end
absDelK=abs((DelK1^2+DelK2^2)^0.5);

```

"generatesection.m"-----

```

function [tmpx]=generatesection(Nk,absDelK)
section=0;
for ii=1:length(Nk)
    section=[section,section(length(section))+absDelK(ii):absDelK(ii):section(length(section))+absDelK(ii)*Nk(ii)];
end
tmpx=section;

```

"plotseg.m"-----
 % This function plots a line segment from Pstart to Pend
 % ex. Pstart=[0,0]; Pend=[5,5]; 09/29/08 Yi-Chen Chuang

```

function plotseg(Nseg,Pstart,Pend)

```

```
if round((Pend(1)-Pstart(1))*1000)~=0 % to make sure Pend(1)~=Pstart(1)
    x=Pstart(1):(Pend(1)-Pstart(1))/Nseg:Pend(1);
    y=(Pend(2)-Pstart(2))/(Pend(1)-Pstart(1))*(x-Pstart(1))+Pstart(2);
else
    x=Pstart(1);
    y=Pstart(2):(Pend(2)-Pstart(2))/Nseg:Pend(2);
end
plot(x,y,'b','LineWidth',1);axis equal; xlim([-5,5]);ylim([-12,12]);
hold on;
```

APPENDIX B: CODE TO GENERATE IRRADIANCE DISTRIBUTIONS

```
% This program generates the irradiance distribution from a 1D binary phase grating
% Need to type-in/import the diffraction coefficients from GSolver to matrix (Am)
% Copyright (c) 2007 by Yi-Chen Chuang.
```

```
lambda=0.364; %[um] incident wavelength in the air
```

```
%% Grating parameters
```

```
tx=2*lambda; ty=tx; % length of unit cell (grating period);
wx=[0.5*tx]; wy=[ty]; % [um] width of the (clear aperture)grating feature
xi=[0]; yi=[0]; % [um] center of the aperture
opx=wx./tx; opy=wy./ty; % opening ratio=w/t
deltaphi=[pi/2]; % phase difference
ds=100; % [um] assume substrate 100 um
ns=1.5; % assume substrate fused silica (glass)
Zt=lambda/(1-(1-(lambda/tx)^2)^0.5); % The Talbot distance, assuming tx=ty
```

```
%% Generate the 3D meshgrids for the propagating space
```

```
y=0; % selected y [um]
xinmax=tx; % xin max [um]
Nxin=500; % Sampling points of x-axis
zinmax=Zt; % z max [um]
Nzin=500; % Sampling points of z-axis
```

```
%% Meshgrids for displaying x-y plane
```

```
[zin,xin]=meshgrid(0:zinmax/Nzin:zinmax,-xinmax:(2*xinmax/Nxin):xinmax);
```

```
%% Calculate the field amplitude by 2D Fourier series expansion
```

```
feature=0; amp=0;
Am=[0.0001 6.26E-22 0.949987 3.56E-22 0.0001]; % complex coefficient from GSolver
[row,column]=size(Am);
for k=1:length(xi);k; % In this case, length(xi) should=length(yi)=length(wx)=length(wy)
    for p=1:row % i-th row in the matrix Am
        for q=1:column; % j-th column
            my=p-(row-1)/2-1;
            mx=q-(column-1)/2-1;
            feature=feature+Am(p,q)*exp(i*2*pi*(mx*xin./tx+my*y./ty)).*exp(-i*2*pi*(mx^2+my^2)*zin./Zt);
        end
    end
amp=1+(exp(i*(deltaphi(k)))-1)*feature; % complex transmission function u(x,y;z)
end
int=abs(amp).^2; % field intensity (irradiance)
phase=angle(amp);
```

```
%% Display the irradiance distribution at selected x-z surfaces
```

```
figure;
imagesc(zin(1,:),xin(:,1),int)
title(['Irradiance colormap at selected x-z plane (y=',num2str(y)]))
set(gca,'Ylabel',text(0,0,['Grating Period (X); DutyCyc.='mat2str(opx)]))
set(gca,'Xlabel',text(0,0,'Normalized Propagation Distance (Z)'))
```

APPENDIX C: DERIVATION OF THE TALBOT DISTANCE

The Talbot distance can be derived based on the diffraction theory described in Section 0. Recall Eq. (3.16) is the equation describing propagated field after an optical grating with normal incidence. In order to show self-imaging, the following condition must be satisfied [129]:

$$U_T(x; z + Z_T) = U_T(x; z) e^{i(2\pi m + \varphi)} \quad (\text{C-1})$$

In this is the case, we have

$$\sqrt{(n_t k)^2 - \left(\frac{2\pi m}{\Lambda}\right)^2} \cdot Z_T = \sqrt{\left(\frac{n_t 2\pi}{\lambda}\right)^2 - \left(\frac{2\pi m}{\Lambda}\right)^2} \cdot Z_T = 2\pi m + \varphi \quad (\text{C-2})$$

$$\sqrt{n_t^2 - \left(\frac{m\lambda}{\Lambda}\right)^2} \cdot \frac{Z_T}{\lambda} = m + \frac{\varphi}{2\pi} \quad (\text{C-3})$$

Letting $m=0$ and -1 in Eq.(C-3):

$$\frac{n_t}{\lambda} \cdot Z_T = \frac{\varphi}{2\pi} \quad (\text{C-4})$$

$$\sqrt{n_t^2 - \left(\frac{-\lambda}{\Lambda}\right)^2} \cdot \frac{Z_T}{\lambda} = -1 + \frac{\varphi}{2\pi} \quad (\text{C-5})$$

Combine Eq. (C-4) and Eq. (C-5):

$$\sqrt{n_t^2 - \left(\frac{-\lambda}{\Lambda}\right)^2} \cdot \frac{Z_T}{\lambda} = -1 + \frac{n_t}{\lambda} \cdot Z_T \quad (\text{C-6})$$

$$\left(n_t - \sqrt{n_t^2 - \left(\frac{\lambda}{\Lambda}\right)^2} \right) \cdot \frac{Z_T}{\lambda} = 1 \quad (\text{C-7})$$

So we obtain

$$Z_T = \frac{\lambda}{n_t - \sqrt{n_t^2 - \left(\frac{\lambda}{\Lambda}\right)^2}} \quad (\text{C-8})$$

If the transmission medium is air, $n_t=1$:

$$Z_T = \frac{\lambda}{1 - \sqrt{1 - \left(\frac{\lambda}{\Lambda}\right)^2}} \quad (\text{C-9})$$

APPENDIX D: CODE TO GENERATE DIELECTRIC FUNCTIONS

```
% This is a program to generate dielectric function of the 2D complex rhombus  
% lattice Talbot crystals and/or other lattice structures analytically  
% Required user-defined function: "SbyLayer.m", "primVect.m"  
% Copyright (c) 2008 Yi-Chen Chuang
```

```
***** Define unit cell and primitive lattice vectors *****  
% For complex rhombus Talbot crystals:  
LRRz= 1.2; % lattice rescale ratio along z-direction  
SR= 1.147; % scaling ratio to tune operating range  
unitZ= (2.5738*SR)*LRRz; % period in z-direction (horizontal)  
unitX= 0.546*SR; % period in x-direction (vertical)  
thetaZX= 90; %[deg] angle between z- and x-direction  
% For general simple lattice cases:  
% unitZ, unitX: norms of the primitive lattice vectors  
% thetaZX: angle between the two primitive lattice vectors  
  
***** Define dielectric materials *****  
er_s= 12; % scatterers permittivity  
er_bg= 1; % background permittivity  
  
***** Define simulation domain *****  
% x-direction (vertical...usually the shorter side)  
xinmax= 1.5*unitX*abs(sin(thetaZX/180*pi)); % [um]xin max  
Nxin= 2^8; % Sampling points in x-direction  
delx= unitX*abs(sin(thetaZX/180*pi)/Nxin);  
% z-direction (horizontal)  
zinmax= 1.5*unitZ; % [um]zin max...little bug: zinmax must >= 1.5 unitZ  
delz= delx;  
Nzin= round(zinmax/delz); % Sampling points in z-direction  
  
Z= 0:delz:zinmax;  
Nz= length(Z);  
X= 0:delx:xinmax;  
Nx= length(X);  
[zin,xin]= meshgrid(0:delz:zinmax,0:delx:xinmax);  
  
***** Generate dielectric function *****  
ER= zeros(Nx,Nz);  
% user-defined function: SbyLayer.m  
% [ER]=SbyLayer(zin,xin,ER,thetaZX,zend,xend,periodZ,periodX,OriginZ,OriginX,sa,sb)  
% in the case of circular scatterer: sa=sb  
ARRz= 0.9; % atom rescale ratio along z-direction (double check=AtomStretch)  
ARR= 1; % atom rescale ratio in all directions (double check=AtomRatio)  
saBig= (0.17*SR)*ARRz*ARR;  
sbBig= (0.06*SR)*ARR;  
saSmall= (0.12*SR)*ARRz*ARR;  
sbSmall= (0.05*SR)*ARR;  
  
% Rhombus sub-lattices  
% at 0  
ER= SbyLayer(zin,xin,ER,thetaZX,2,3,unitZ,unitX/2,0,unitX/4,saSmall,sbSmall);
```

```

% at 1/4*unitZ
ER= SbyLayer(zin,xin,ER,thetaZX,2,3,unitZ,unitX/2,unitZ/4,unitX/4,saSmall,sbSmall);
% % at 2/4*unitZ
ER= SbyLayer(zin,xin,ER,thetaZX,8,3,unitZ/4,unitX/2,0,unitX/4,saSmall,sbSmall);
% at 3/4*unitZ
ER= SbyLayer(zin,xin,ER,thetaZX,2,3,unitZ,unitX/2,unitZ*3/4,unitX/4,saSmall,sbSmall);
% at unitZ
ER= SbyLayer(zin,xin,ER,thetaZX,2,3,unitZ,unitX/2,unitZ,unitX/4,saSmall,sbSmall);

% Rectangular sub-lattice
% at 1/8*unitZ
ER= SbyLayer(zin,xin,ER,thetaZX,1,3,unitZ,unitX,unitZ/8,unitX/2,saBig,sbBig);
% at 3/8*unitZ
ER= SbyLayer(zin,xin,ER,thetaZX,1,2,unitZ,unitX,unitZ*3/8,0,saBig,sbBig);
% at 5/8*unitZ
ER= SbyLayer(zin,xin,ER,thetaZX,1,2,unitZ,unitX,unitZ*5/8,0,saBig,sbBig);
% at 7/8*unitZ
ER= SbyLayer(zin,xin,ER,thetaZX,1,2,unitZ,unitX,unitZ*7/8,unitX/2,saBig,sbBig);

% Convert Boolean to materials
ER= (er_s)*(ER) + (er_bg)*(~ER);
int1= ER;

%***** Show dielectric function *****
figure;
pcolor(Z,X,ER);
axis equal tight;
shading flat;
h= colorbar;
h= get(h,'Title');
set(h,'String','\epsilon_r');
title('Permittivity profile');

%***** Define the primitive lattice vectors *****
% user-defined function: primVect.m
[t1,t2,t3]= primVect(unitZ,unitX);

```

Required user-defined MATLAB functions:

```
"SbyLayer.m"-----
% This is the routine function to generate periodic complex lattice
% layer-by-layer analytically
% 11/18/08 updated Yi-Chen Chuang
function [ER]=SbyLayer(Zc,Xc,ER,thetaZX,zend,xend,periodZ,periodX,OriginZ,OriginX,sa,sb)
    for ii=0:xend;
        for jj=0:zend
            R = ((Zc-(ii*periodX*cos(thetaZX/180*pi)+jj*periodZ+OriginZ))/sa).^2 + ((Xc-
                (ii*periodX*sin(thetaZX/180*pi)+OriginX))/sb).^2;
            ER = ER | (R<=1^2);
        end
    end
end
```

```
"primVect.m"-----
function [t1,t2,t3]=primVect(unitZ,unitX)
% Define the primitive lattice vectors
tA=[unitZ,0,0];
tB=[unitZ/2,unitX/2,0];
tC=[0,unitX,0];
tD=[-unitZ/2,unitX/2,0];
thetaab=atan(unitX/unitZ)/pi*180; %[deg]

% primitive lattice vectors chosen from above lattice vectors
if (round(thetaab)>=60) && (round(thetaab)<=90)
    t1=tA;
    t2=tB;
    t3=[0,0,1]; %2D
elseif (round(thetaab)<60) && (round(thetaab)>30)
    t1=tB;
    t2=tD;
    t3=[0,0,1]; %2D
elseif (round(thetaab)<=30) && (round(thetaab)>0)
    t1=tB;
    t2=tC;
    t3=[0,0,1]; %2D
else
    display('Be aware: "thetaa" is out of range!')
end
```